CRANFIELD UNIVERSITY

Laurie Finian Brooking

Combined hot corrosion and static stress or fatigue of single crystal superalloys

School of Water, Energy and Environment

PhD
Academic Year: 2015 - 2018

Supervisor: Professor Nigel Simms
Associate Supervisors: Dr Joy Sumner and Dr Simon Gray
September 2018

CRANFIELD UNIVERSITY

School of Water, Energy and Environment

PhD

Academic Year 2015 - 2018

Laurie Finian Brooking

Combined hot corrosion and static stress or fatigue of single crystal superalloys

Supervisor: Professor Nigel Simms
Associate Supervisors: Dr Joy Sumner and Dr Simon Gray
September 2018

This thesis is submitted in partial fulfilment of the requirements for the degree of Doctor of Philosophy

Abstract

It has been observed that gas turbine (GT) blades operating in harsh environments can undergo material degradation in the form of crack initiation and propagation before that predicted by fatigue lifing. It is thought that this degradation can occur partly as a result of the growing demands for improved GT efficiencies. This is because the requirement for improved GT efficiencies is commonly achieved through increases in operational temperatures and pressures which the turbine stages operate at. These increases in the operational temperatures can consequently lead to the extended effect of hot corrosion in locations of the blade which would not normally impacted, such as the under platform region. Therefore, GT blades are subjected to continuous developments in terms of blade design and material properties and selection in order to achieve improvement in the GT efficiencies, reduce emissions and lower life cycle costs. However, at start of this research project it was postulated that the mechanism causing premature material degradation is a result of the extended effects of low temperature hot corrosion (LTHC), interacting with both cyclic and static loading conditions. In order to experimentally study these interactions statically and cyclically loaded specimens were tested in environments representative of the under platform region of both industrial and aviation gas turbine (GT) blades. A range of geometries were studied: C-rings, three point bend and cylindrical fatigue specimens. Using these specimens experimental studies were conducted investigating the impact of deposit flux, dwell time, multiaxial stress state and load application rate. Further investigations into the microscopic mechanism occurring at the crack tip have been conducted using high magnification transmission electron microscopy (TEM) and scanning electron microscopy (SEM). Detailed stress state data has been produced using finite element analysis (FEA), this data has then been used to assess the impact of the stress state on crack initiation and propagation. It was found that turbine blade materials were susceptible to a form of high temperature stress corrosion cracking (SCC). Additionally, enhanced fatigue crack initiation and propagation was observed with test conditions consistent with low temperature hot corrosion (LTHC) conditions. There was shown to be a detrimental impact with increased rates of LTHC on the high temperature cracking mechanism. Detailed microscopy and analysis of specimens informed a proposed fundamental mechanism behind the enhanced cracking observed in LTHC environments. The five research papers presented within this thesis provide contributions to knowledge and developments in the understanding of crack initiation and propagation within superalloys exposed to simultaneous LTHC environments and loading.

Keywords:

Single crystal superalloys, Hot corrosion, Fatigue, Corrosion cracking, FEA

Acknowledgements

I would like to acknowledge the plethora of personal, academic and industrial support I have received over the course of this project, and without which the work would not have been possible. Starting with the personal support I would like to thank all of my wonderful mums: Ann, Janneke, Kathy and Anne who have foremost raised me, but who have also been with me every step of the way throughout my PhD providing sound guidance and support. I would also like to thank my brother Josh, my father Guy, and the two family dogs Bobby and Benji who have always helped to keep my spirits high. There are too many supportive friends to mention but in the name of keeping drunken promises, I would like to acknowledge the select few who went beyond the call of duty: Maadhav, Oliver, Caspar, Alex and Adnan thanks for the friendship and support. Last but by no means least I would like to thank Ciara my wonderful girlfriend, who between saving lives still finds the time and energy to support me in my endeavours.

In terms of academic support I would like to thank my supervisors and subject advisor: Dr Simon Gray, Dr Joy Sumner, Professor Nigel Simms and Professor John Nicholls. I have benefited from their academic guidance and extensive knowledge, as well as their inspiring love for the subject area. Without their help the project would not have been possible. Additionally I would like to thank Simon for the beers, friendship and jokes exchanged over the course of my project. I would also like to acknowledge and thank Tim Pryor for his un-rivalled technical knowledge in the lab, and Professor Gordon Tatlock and the University of Liverpool for their support in conducting some fascinating TEM imaging for the research project.

Finally I would like to thank all of the Flex-E-Plant partners listed in the acknowledgements of the papers, but with a special thanks to the following: Geoff Marchant, Neil Chapman and Jonathon Wells of Siemens Industrial Turbomachinery, thank you for the data, support and guidance provided for the project.

Contents

List of Figures

List of Tables

List of Equations

1. Introduction

1.1. General introduction to project and research papers

Gas turbines (GTs) both industrial and aero often operate in chemically dirty environments, with contamination from both sulphur content within the fuels used, and particulate and salt content within the air ingested by the turbine system. These contaminants contribute towards the conditions required for hot corrosion. Additionally the ever growing industry drive to improve the thermal efficiencies of GTs results in increases in turbine temperatures, providing a growing requirement to understand the extended impact of hot corrosion on regions of turbine components not normally impacted.

Typically, GT components are lifed for a number of environmental, temperature, time, load and cycle dependent degradation mechanisms such as creep, oxidation/corrosion and fatigue. However, often the combined effects of the above mechanisms are not comprehensively considered during the design and engineering process.

The component focused on during this research is the turbine blade, specifically the under platform region of a 1st stage turbine blade (Figure 1.1). This region of the blade is exposed to cyclic and static dwell loading, cooling air and sometimes combustion gasses that can bleed by the platform seals. The temperatures in this area are normally in the lower region of the blades operating range, and are between 450 – 700 ^{o}C. Single crystal (SC) Ni-based superalloys such as CMSX-4 are used as 1st stage turbine blades, primarily because of their favourable high temperature creep properties.

With the ever increasing temperature demands on turbine blades required in order to improve turbine efficiencies, the conditions of the under platform region of gas turbine blades are often consistent with those of hot corrosion. The combination of this high temperature corrosion mechanism with both static and cyclic loading has led to the premature degradation and cracking within the under platform region of blades in both industrial and aerospace applications.

Turbine blades are both a safety critical and serviceable component of the gas turbine and as such have to be routinely inspected and sometimes replaced at significant cost to the customer or manufacture. Therefore designing the turbine blade to have the longest possible safe operational life is of great benefit to the life cycle cost of the turbine system. However, if poorly managed and predicted, the unexpected degradation of the turbine blades could lead to complete turbine failure which is both a major safety concern and expense in terms of scrappage and down time costs.

As such a better understanding of the hot corrosion cracking mechanism is required in order to be able to more accurately predict and life the degradation mechanism. Understanding of these particular combined mechanisms is still in its infancy, and this body of research presents some significant findings on the subject area.

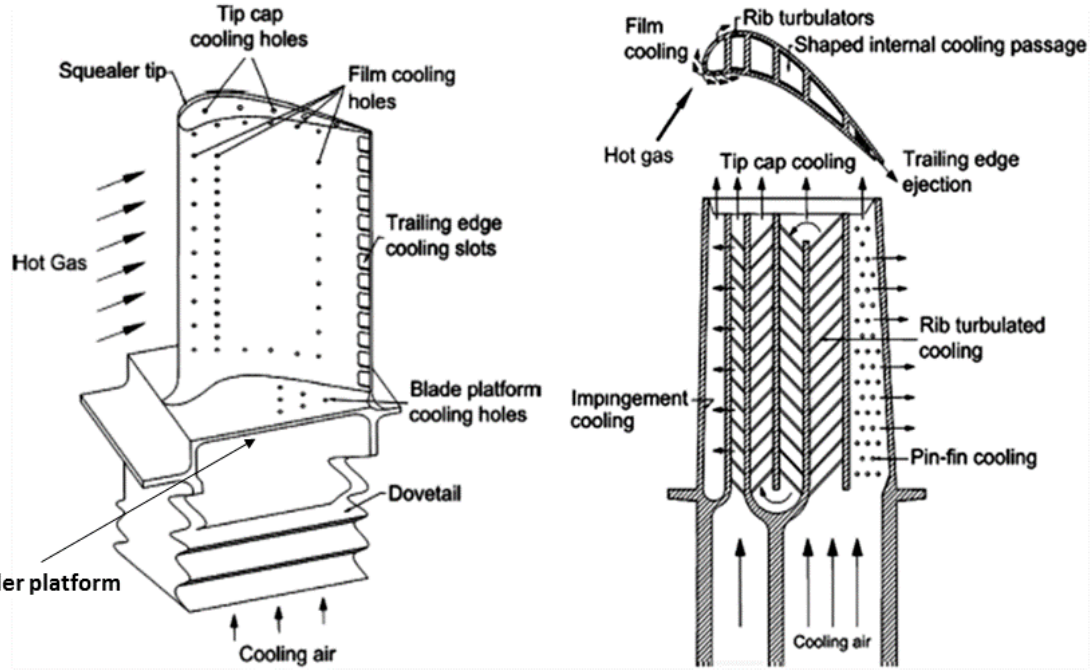

Figure 1.1: Schematic of a typical gas turbine blade, showing the under platform and dovetail regions on the left, and a cross section of the cooling passages on the right [1]

Due to the conditions present in the under platform region, this location can be susceptible to low temperature hot corrosion (LTHC), also often referred to as type II hot corrosion. Whilst additionally the load/stress conditions experienced (both static and cyclic) can lead to fatigue and cracking type degradation. It is further plausible that LTHC could occur at temperatures below those normally considered due to simultaneous loading and stresses. Furthermore it is possible that fatigue cracking could occur below the fatigue threshold due to the simultaneous influence of LTHC in this region of the blade. It is the intimate interactions between these two normally unrelated degradation mechanisms that forms the basis of this research. The influence of creep is not considered in the scope of this work as the temperature of 550 ^{o}C studied is considered below the creep limit for CMSX-4; creep is documented as occurring in CMSX-4 at temperatures greater than 700 ^{o}C [2]. An indication of creep in γ/γ' superalloys is the formation of rafted precipitates [3], which would be expected to be omitted in the absence of creep.

The thesis is constructed from research presented over five papers which are outlined in table 1.1. For reference within the thesis the papers are numbered from 1 to 5, the designation of which is also outlined in table 1.1. The specific contributions made by the candidate towards the papers is stated in table 1.2.

Table 1.1: List of research papers

Paper number	Title	Published status	Journal	DOI
1	Stress corrosion of Ni-based superalloys	Published	Materials at High Temperature Volume 35 Pages 120-129	10.1080/09603409.2017.1392414
2	Interaction of hot corrosion fatigue and load dwell periods on a nickel-base single crystal superalloy	Published	International Journal of Fatigue Volume 117 Pages 13-20	10.1016/j.ijfatigue.2018.07.029
3	Effect of stress state and simultaneous hot corrosion on the crack propagation and fatigue life of a single crystal superalloy CMSX-4	Published	International Journal of Fatigue Volume 116 Pages 106-117	10.1016/j.ijfatigue.2018.05.002
4	Analysis of combined static load and low temperature hot corrosion induced cracking in a Ni-based single crystal superalloy	Un Published	Intended for submission to a corrosion journal	N/A
5	Corrosion fatigue testing: the combined effect of stress and high temperature corrosion	Published	Materials at High Temperature Volume 35 Pages 151-158	10.1080/09603409.2017.1389100

Table 1.2: Contributions from the PhD candidate to the papers presented in the thesis

Paper number	Candidate's contribution to papers	Additional author's contributions to papers
1	The candidate conducted the experimental work and analysis/imaging. The candidate was the primary author of the paper.	J.Sumner, N.J.Simms and S.Gray – Supervised the research, and contributed to technical content of paper
2	The candidate conducted the experimental work and analysis/imaging. The candidate was the primary author of the paper.	S.Gray, J.Sumner, J.R.Nicholls, N.J.Simms – Supervised the research, and contributed to the technical content of the paper
3	The candidate conducted the experimental work and analysis/imaging with some SEM imaging conducted at Siemens Industrial Turbomachinery. The candidate was the primary author of the paper.	S.Gray, J.Sumner, J.R.Nicholls, N.J.Simms – Supervised the research, and contributed to the technical content of the paper G.Marchant – Industrially supervised the research and provided specimens and contribution to technical content
4	The candidate designed and conducted the experimental work as well as conducting some of the SEM analysis. The FIB and TEM analysis was conducted by Karl Dawson and Gordon Tatlock at the University of Liverpool. The candidate was the primary author of the paper.	S.Gray, J.R.Nicholls, N.J.Simms, J.Sumner – Supervised the research, and contributed to the technical content of the paper K.Dawson, G. J.Tatlock – Conducted microscopy analysis and contributed to technical content of the paper
5	The candidate supported with generation of LTHC fatigue data and discussion around technical content, however the development of concepts and theories presented was produced by the primary author. As such the candidate is credited as a secondary author on the paper.	Neil Chapman – Primary author of the paper Joy Sumner, Simon Gray and John Nicholls – Supervised the research, and contributed to the technical content of the paper

The papers cover two general topic areas: crack propagation under static loading and crack propagation under cyclic loading. Both of these loading conditions were generated in specimens that were simultaneously exposed to LTHC environments. Two of the papers further compare and

discuss the interactions between static load crack growth and dynamic loading fatigue crack growth. The topics covered in each paper and the way they are interlinked are presented in figure 1.2.

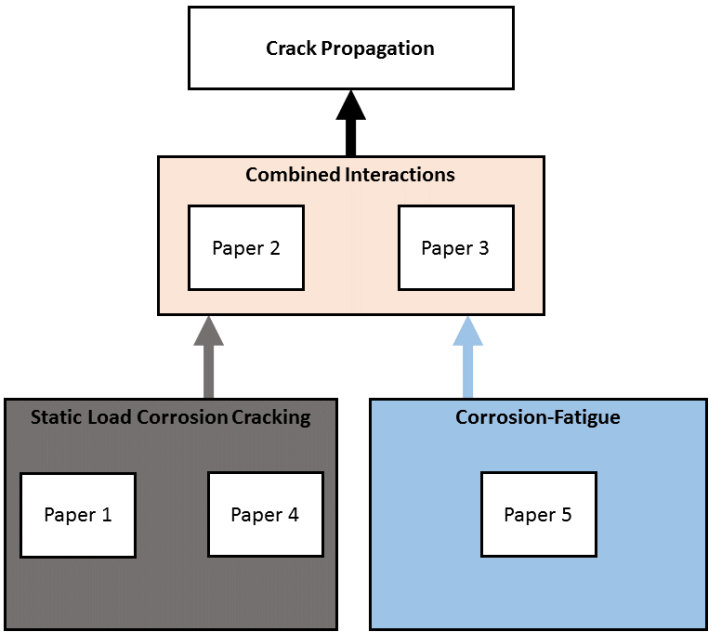

Figure 1.2: Subject areas covered by papers

In the papers which are public documents, fatigue results are presented in a normalised format due to the commercial sensitivity of the research. A complete tabulated list of the LTHC fatigue data generated throughout the project can be found in Appendix 1 in an un-normalised format.

Three specimen geometries were used throughout the project and the details of these can be found within the thesis as follows:

- C-ring geometry: paper 1
- Uniaxial fatigue specimen geometry: paper 5
- The details of the three point bend jig and specimen geometry developed: appendix 2

A brief overview and introduction to the topics and methodologies used throughout the research is outlined in the thesis Sections 1.2. to 1.5. A more detailed review of the literature and an introduction to the topics specific to each paper is given within the papers themselves.

A summary overview of each paper highlighting the specific questions it sets to answer, the papers aims and its contributions to knowledge is given in Section 1.7.

1.2. Introduction to fatigue

Fatigue is a phenomenon caused by cyclic loading, where over a number of cycles crack initiation and subsequent crack propagation can take place. This can lead to the degradation and possible

failure of a component over a period of usage. Fatigue is an insidious process which occurs at loads below what would normally be the maximum design limits for a specific component, and as such it is a crucial design consideration. Therefore, it is important to be able to predict and account for the fatigue life of components in order to ensure safe operation and life cycle strategies over a period of use.

There are a number of fatigue models and methodologies commonly used to predict a component's fatigue performance and life, these being stress-life, strain-life [3] and fracture mechanics [4]. All of these methodologies use experimentally determined material fatigue properties and parameters. In the design, specification and optimisation process these properties are assessed against a specific components loading or duty cycle, in order to estimate and predict the fatigue life and performance of the component. Often, mechanically loaded components will either be designed to operate below the fatigue limits of the material(s) used, or they will be designed to have a safe operational fatigue life before they need to be inspected and/or repaired or replaced.

The decision of whether or not to design a component to operate below a theoretical fatigue limit, or to operate within a fatigue life, is often a function of the requirements on that component, and how close to the material limits it therefore needs to operate. For example, where low weight is a key factor in the design brief, there is a requirement to minimise the mass of material used for the component. This requirement often results in a compromise in the load bearing cross sectional area, which results in the design stresses being greater within the component. Whilst there are normally a variety of other design considerations involved, this weight/stress compromise is often a design factor for large structural components such as aircraft fuselages, as well as rotational components such as GT blades. Therefore, in these cases regular inspection and/or repair or replacement is required, and fatigue lifing is a critical factor in the design process. Fracture mechanics is a widely used tool in fatigue lifing, as such it is used as an analytical tool throughout this research. Further literature review of fracture mechanics methods is given within papers 1, 2 and 3.

Whilst pure fatigue is considered to be a function of loading cycles, it is well documented that other time and environment dependent degradation mechanisms such as corrosion can accelerate the initiation and propagation of fatigue cracks. As a result of this, modelling approaches which account for the effects of environmental conditions on fatigue have been developed [5][6][7]. These models are dependent on the specific interactions between fatigue and the environmental conditions they were developed for and are often too complex to be easily applied to other environments. Consequently, these models are not currently widely adopted and instead, a fatigue safety factor may be used. Due to the insufficient techniques available to model fatigue in corrosive environments, this enhanced fatigue propagation can often be overlooked in components that operate in particularly aggressive or corrosive environments.

1.3. Introduction to type II hot corrosion (LTHC)

Hot corrosion is the accelerated chemical degradation of materials, and is commonly separated into two distinct mechanisms. These are low temperature corrosion (LTHC), also referred to as type II hot corrosion, and high temperature hot corrosion (HTHC), also referred to as type I hot corrosion. LTHC is generally considered to occur between 600 - 750 ^{o}C and HTHC between 850 - 900 ^{o}C [8].

LTHC has historically been studied and modelled independently of load/stress or loading cycles. Current empirical modelling approaches are dependent on exposure time, temperature and deposit composition/deposition flux [9][10]. The LTHC corrosion mechanism is thought to occur due to the formation of a liquid mixture on the surface, which then results in the dissolution of any protective oxide scale the material may have, and subsequently the corrosion of the substrate. A more detailed literature review and introduction to relevant corrosion mechanisms, as well as specifically LTHC is given in all the papers. The most comprehensive introduction and overview is covered in paper 4 concentrating on the electrochemical aspects of LTHC.

1.4. Introduction to electron microscopy

All five of the papers present scanning electron microscopy (SEM) data alongside energy dispersive X-ray (EDX) analysis [11]. Additionally paper 4 presents transmission electron microscopy (TEM) imaging [12]. As such electron microscopy techniques have provided an important analytical tool utilised throughout the course of the research. Therefore, a brief introduction into the methods and techniques used is given below.

In SEM imaging, a focused beam of electrons is scanned across the surface of a sample. By correlating the location of this beam to the back scattered (BSE) or secondary electrons (SE) detected, an image of the surface can be obtained. SE are emitted by atoms near the surface and therefore give more detailed topological imaging capabilities than BSE. However, BSE imaging is more sensitive to atomic mass and can contrast more effectively between heavier and lighter elements within a sample.

The electrons which bombard the surface of the specimen during the SEM imaging, generate energy dispersive X-rays which are emitted from the ionised particles on the specimen surface. These X-rays can be further analysed using EDX techniques, which provides data about the localised elemental composition of the sample being analysed. EDX analysis can be conducted either for single points or mapped over the scan area. Some elements have overlapping X-ray emission peaks and whilst sometimes this can be overcome with the careful consideration of the elements likely present and consideration of the L_α, K_α, K_β signals, in some circumstances it is not possible to determine which element is present when there is peak overlap.

In TEM imaging, a beam of electrons is accelerated at an ultra-thin sample, an image can then be formed by measuring the density and energy of the electrons which pass through the sample. TEM microscopy offers extremely good magnification and resolution capabilities, which are close to the atomic scale. Normally TEM samples are prepared using field ion beam (FIB) machining, where a thin lamella is machined out of a sample at a point of interest, which can then be transferred to a TEM for high magnification imaging.

1.5. Introduction to finite element analysis

Another analytical tool utilised was finite element analysis (FEA) [13]. FEA is a structural modelling method used to analyse and calculate stress, strain and other thermal magnetic and mechanical parameters, within a defined geometry subjected to boundary conditions. This is achieved by producing a geometrical mesh of elements and nodes which are assigned set material properties. When the boundary conditions are applied the FEA solver then solves a series of simultaneous equations to determine local conditions present in each element of the geometry. Over the course of this work FEA was used to calculate the stress states within specimen geometries and locally at crack tips. FEA results are presented in papers 1 and 3, with results also being discussed in paper 2.

1.6. Aims and Objectives

Aims

The project aims to understand premature material degradation observed in the under platform regions of gas turbine blades, which can be characterised by a cracking morphology encompassing both initiation and propagation. It studies the parameters affecting this crack initiation and propagation through experimental investigation and then uses microscopy and analytical techniques to better understand the mechanism behind this material degradation.

Objectives

1) Develop an increased understanding of how LTHC atmospheres interact with both static and cyclic load/stress through experimental testing of the uncoated single crystal superalloy CMSX-4.

2) Utilise modelling methods to determine the stresses and local conditions present within the specimen geometries used for testing. Use this data to study the effects of stress state on the crack initiation and propagation.

3) Experimentally explore factors which impact the fatigue stress cycles to failure (S-N) curves and crack propagation rates under combined stress and low temperature hot corrosion (LTHC) environments.

4) Develop an improved fundamental understanding of the mechanism(s) acting at the crack tip through the use of analytical techniques. Combined this improved understanding with experimental observations to propose new models for crack advance.

Each paper aims to address specific objectives of the research project as a whole, these paper contributions are tabulated in Table 1.3. Together the papers add to the current understanding of LTHC stress interactions within single crystal superalloys, and help inform future research in the field.

Table 1.3: Objectives addressed by each paper

Paper	Objectives covered
Paper 1	**1, 2**
Paper 2	**1, 3**
Paper 3	**1, 2, 3**
Paper 4	**1, 4**
Paper 5	**1, 3**

1.7. Overview of papers

1.7.1. Paper 1 overview: Stress corrosion of Ni-based superalloys

Question the paper set out to answer	• How does static stress and LTHC interact, and what is the suitability of the C-ring testing methodology for higher temperature applications?
Paper introduction	• The introduction provides a literature review of LTHC in Ni-based superalloys. • The literature reviewed also covers LTHC-load interactions.
Experimental testing and data generated	• Experimental studies were conducted varying the load and removing/reducing the deposit flux.
Analytical investigations	• SEM/EDX imaging and analysis of specimens was performed. • FEA modelling of C-rings with and without cracks was performed.
Key findings and contributions to knowledge	• Analysis using SEM imaging and EDX mapping confirmed that the corrosion mechanism was consistent with type II/LTHC at temperatures as low as 550 ^{o}C when assisted by load/stress. • It was demonstrated experimentally on C-rings that combined static loading and LTHC can result in crack initiation and propagation in the SC superalloy CMSX-4. • It was demonstrated that for crack initiation and subsequent propagation to occur, a salt deposit flux was required. • Comparison of FE modelled stresses in C-rings was close to those predicted by the ISO standard used when comparing equivalent von Mises stresses. • Using FEA it was determined that the corrosive environments and test durations studied could theoretically lower the stress intensity limit required for cracking by up to 75%. • It was observed that there was preferential γ/γ’ corrosion attack, with the γ’ being attacked at the crack tip and the γ towards the specimen surface.

1.7.2. Paper 2 overview: Interaction of hot corrosion fatigue and load dwell periods on a nickel-base single crystal superalloy

Questions the paper set out to answer	• What are the B of increasing the load dwell period on the fatigue life in LTHC environments? • What are the effects of increasing the load dwell period on the fracture face morphology in LTHC environments?
Paper introduction	• The introduction provides a review of the industrial requirement for studies into combined LTHC and fatigue. • A review of the relevant literature concerning combined LTHC-fatigue is given.
Experimental testing and data generated	• Experimental studies were conducted looking at the effects of combined LTHC and fatigue as well as extending the maximum load dwell period of the fatigue cycle.
Analytical investigations	• Optical and SEM images are presented along with EDX analysis of specimens and fracture faces.
Key findings and contributions to knowledge	• It was found that dwell increased the number of externally initiated {100} cracks and significantly reduced the fatigue life. • It was observed that extended dwell tests took longer to fail under the wave forms studied. • The paper presents fracture face analysis which suggests a start/stop nature to the crack propagation and observes a change in the fracture face crystallographic topology which correlates to the fatigue threshold being exceeded. • It is proposed that fatigue crack initiation is accelerated with the introduction of dwell due to static crack growth and increased crack tip exposure to corrosion.

1.7.3. Paper 3 overview: Effect of stress state and simultaneous hot corrosion on the crack propagation and fatigue life of a single crystal superalloy CMSX-4

Questions the paper set out to answer	• What are the effects of stress state on the crack initiation and propagation of static load cracking? • What are the effects of LTHC salt flux on the fatigue life? • What are the possible mechanisms behind the crack behaviours and morphologies observed?
Paper introduction	• An introduction into basic fracture mechanics is provided as an introduction to the approach used. • A review of literature on LTHC in superalloys is given as well as published research on LTHC-fatigue.
Experimental testing and data generated	• The paper experimentally studies cracking in statically loaded specimens within three geometries: C-rings, three point bend and plain cylindrical specimens. • The paper experimentally studies the effects of salt flux/deposition rate on combined crack initiation and propagation in statically loaded C-rings and plain cylindrical fatigue specimens.
Analytical investigations	• SEM imaging and EDX mapping were conducted on specimens. • FEA analysis was conducted to define the stress states and calculate stress intensities within the specimen geometries.
Key findings and contributions to knowledge	• It was observed that increasing the deposition flux and therefore corrosion rate, had the effect of generating preferential orthogonal {100} fracture planes. • The aggressiveness of crack initiation and propagation in statically loaded specimens correlated with the stress gradient present. • Preferential corrosion attack of γ’ was observed at crack tip locations, whilst the γ was preferentially attacked towards the specimen surface. • A mechanism of gas induced acidic fluxing at the crack tip and alloy induced acidic fluxing towards the surface was proposed as an explanation for the preferential corrosion attack. • It was further proposed that the preferential corrosion attack of the gamma-prime resulted in orthogonal {100} propagation due to the orthogonal attack of net closest γ’ phases at the crack tip. • It was proposed that crack propagation can occur due to localised environmentally assisted lattice de-cohesion.

1.7.4. Paper 4 overview: Analysis of combined static load and low temperature hot corrosion induced cracking in a Ni-based single crystal superalloy

Questions the paper set out to answer	• What is the mechanism occurring at the crack tip that enables crack propagation under static loading? • Are there any effects of stress on LTHC?
Paper introduction	The introduction provides a review of literature into the following areas. • The industrial motivations for studies into LTHC and load interactions generating cracking in superalloys. • The single crystal γ/γ' microstructure and its anisotropic properties. • Previous research studying LTHC and fatigue in Ni-based superalloys. • Comparative mechanisms of SCC and static load crack propagation. • Electrochemical nature of LTHC and the electromechanical interactions within crystalline materials.
Experimental testing and data generated	• The paper analyses a statically loaded three point bend specimen that has been exposed to LTHC under both tension and compression.
Analytical investigations	• The paper presents high magnification TEM and SEM imaging, as well as EDX analysis of a crack tip generated within the specimen.
Key findings and contributions to knowledge	• The analysis demonstrates [100] crack propagation cutting through the γ' precipitates, slip systems and defects are visible ahead of the crack tip however there is no evidence of diffusion ahead of the crack. • It is demonstrated that the preferential corrosion attack of the γ/γ' is sensitive to stress/deformation effects. Where tensile deformation generates preferential γ' attack and compressive deformation γ attack. • Corrosive species and electrolytes such as Na_2SO_4 were found at the crack tip suggesting an electrochemical type II/LTHC mechanism could be present in this critical location. • Elemental mapping showed segregation of W to the γ'. It was suggested that W could compete with Ta and Mo due to their similar ionic radii. A stress assisted LTHC electrochemical mechanism is proposed at the crack tip, resulting in oxidation and enhanced de cohesion, generating crack propagation. It is further suggested that there is a deformation related effect on the anodic potential of the γ/γ' phases independently, which results in preferential corrosion attack of the phases under tension and compression.

1.7.5. Paper 5 overview: Corrosion fatigue testing: the combined effect of stress and high temperature corrosion

Questions the paper set out to answer	• What is the impact of load application rate on the LTHC fatigue life, in a LTHC environment? • What is the effect of LTHC on the propagation plane in uniaxial cylindrical fatigue specimens?
Paper introduction	• The introduction provides a literature review and study into type II/LTHC and the protective formers generated by Ni-based superalloys. • A review of the impact of stress application or ramp up rate on the fatigue crack propagation is also given.
Experimental testing and data generated	• The paper experimentally studies the effects of the ramp period on fatigue cycles to failure in a LTHC/type II corrosion environment.
Analytical investigations	• Optical imaging of specimens is presented along with SEM imaging and EDX analysis.
Key findings and contributions to knowledge	• A detrimental influence of decreasing the ramp rate on the fatigue life is observed. It is proposed that this behaviour is associated to crack tip blunting generated by the increased dislocation emissions resulting from the higher ramp rates. • A corrosion effect on the preference of the crack propagation plane from {111} to {100} is observed with an increase in the corrosion attack.

1.8. Introduction references

[1] L. M., S. M. Shaahid, and A. A., "Jet Impingement Cooling in Gas Turbines for Improving Thermal Efficiency and Power Density," *Adv. Gas Turbine Technol.*, no. state 3, 2011.

[2] A. Epishin, T. Link, M. Nazmy, M. Staubli, and G. Nolze, "Microstructural degradation of cmsx-4: kinetics and effect on mechanical properties," *Proceeding Superalloy 2008, (Editors R. C. Reed al.,)*, pp. 725–731, 2008, 2008.

[3] N. E. Dowling, *Mechanical Behavior of Materials*, 4th ed. Boston, MA : Pearson, 2012.

[4] T. L. Anderson, *Fracture Mechanics: Fundamentals and Applications*, vol. 58, no. 1. 2012.

[5] D. A. Woodford, "Gas phase embrittlement and time dependent cracking of nickel based superalloys," *Energy Mater.*, vol. 1, no. 1, pp. 59–79, 2006.

[6] D. Gustafsson, J. Moverare, S. Johansson, and M. Hörnqvist, "Procedia Engineering Fatigue crack growth behaviour of Inconel 718 with high temperature hold times," 2010.

[7] A. Saxena and K. Findley, "AFRL-ML-WP-TR-2007-4117 DWELL-TIME FATIGUE CRACK GROWTH IN Ni-BASE SUPERALLOYS," no. April 2003, 2007.

[8] D. A. Shifler, "Hot corrosion: a modification of reactants causing degradation," *Mater. High Temp.*, vol. 35, no. 1–3, pp. 225–235, 2018.

[9] J. Sumner, A. Encinas-Oropesa, N. Simms, and J. R. Nicholls, "Type II hot corrosion: Behaviour of CMSX-4 and IN738LC as a function of corrosion environment," *Mater. Corros.*, no. 2, pp. 188–196, 2014.

[10] K. S. Chan, M. P. Enright, and J. P. Moody, "Development of a Probabilistic Methodology for Predicting Hot Corrosion Fatigue Crack Growth Life of Gas Turbine Engine Disks," *J. Eng. Gas Turbines Power*, vol. 136, no. 2, p. 022505, 2014.

[11] D. N. Leonard, G. W. Chandler, and S. Seraphin, "Scanning Electron Microscopy," in *Characterization of Materials*, 2012.

[12] D. B. Williams and C. B. Carter, *Transmission Electron Microscopy: A Textbook for Materials Science*. 2009.

[13] D. V. Hutton, "Fundamentals of Finite Element Analysis," *Textbook (Important)*. 2004.

2. Paper 1: Stress corrosion of Ni-based superalloys

L.Brooking, J.Sumner*, S.Gray, N.J.Simms

Cranfield University, College Rd, Cranfield, MK43 OAL

*Corresponding author: j.sumner@cranfield.ac.uk

Abstract. The development of gas turbines to increase fuel efficiency is resulting in progressively higher operating temperatures in the under platform regions of the blades. These regions have traditionally been considered low risk areas. However, higher metal temperatures combined with stresses and the deposition of contaminants from the cooling air system may result in complex degradation mechanisms.

Static stress corrosion testing has been conducted on C-ring specimens at a range of stresses in a hot corrosion environment. Cracks were observed in C-rings after exposure times greater than 100 h. Scanning electron microscopy (SEM) systems were used to image cracks and characterise deposits to improve understanding of the mechanism. Finite element analysis (FEA) has been used to model the stress intensity under test conditions.

CMSX-4 specimens subject to static stresses combined with hot corrosion demonstrated significant material degradation (crack initiation and propagation) suggesting a combined stress corrosion mechanism resulting in cracking.

Keywords: Stress Corrosion, Superalloy, C-ring, FEA

List of Symbols

D - Outside diameter

D_f - Final outside diameter when stressed

D_{AV} - Average Diameter of C-ring

σ - Stress

t - C-ring thickness

Z - Correction factor for curved beams

E - Young's modulus

d - Mean inner diameter of C-ring

K - Stress intensity

Υ - LEFM geometry factor

a - Crack length

K_{th}- Stress intensity threshold

2.1. Introduction

Gas turbines are widely used in power generation systems. Developments to improve their efficiencies have led to increased operating temperatures of regions of some components, such as the under platform areas of turbine blades. The high stress state of the root pocket due to the high rotational speeds, combined with cooling air derived deposits and temperatures approaching the conditions associated with type II corrosion, can lead to cracking [1].

CMSX-4 (Table 2.1) is a single crystal Ni-based superalloy commonly used for 1st stage gas turbine blades as a result of its good high temperature creep-strength properties combined with production affordability [2]. However due to its composition (lower Cr content than other commonly used 1st stage turbine blade materials), CMSX-4 is susceptible to type II hot corrosion. This can result in damage that has the morphology of either pitting or broad fronted attack. Sumner et al [3] have reported investigations of type II hot corrosion of CMSX-4, using statistical analysis of large data sets to generate models for specific conditions. They observed broad fronted attack and more rapid depletion of Cr in CMSX-4, when compared with IN738LC.

Table 2.1 : Composition of CMSX-4 (wt%)

Alloy	Cr	Co	Mo	Al	Ti	Ta	Re	Hf	Ni
CMSX-4	6.5	9.6	0.6	5.6	1.0	6.5	3.0	0.1	Bal.

Research conducted on hot corrosion mechanisms in 1970s-1980s is summarised by Luthra & LeBlanc [4]. They concluded that hot corrosion could occur through a combination of three mechanisms: sulphidation-oxidation, formation of volatile compounds beneath the protective oxide layer or scale fluxing. Fluxing models have since gained the widest acceptance for deposit induced hot corrosion [5, 6].

The process of type II hot corrosion of Ni-based superalloys requires the formation of a liquid eutectic film [5, 6]. Type II hot corrosion occurs in the temperature range of 650°C-800°C through the formation of minimum melting point mixtures of Na_2SO_4, $NiSO_4$ and $CoSO_4$ [4, 5, 8]. $NiSO_4$ and $CoSO_4$ compounds form as a result of the reaction of SO_3 with nickel and cobalt from the superalloy. A widely accepted mechanism for hot corrosion was proposed by Goebel & Pettit [9]. Their mechanism outlines two stages, firstly the incubation stage, where a liquid eutectic of Na_2SO_4, $NiSO_4$ and/or $CoSO_4$ forms on the component surface; as a result of deposition coupled with a reaction between sulphur oxides and nickel and/or cobalt from the superalloy. The second stage is the propagation stage where the fluxing of the surface oxide by a liquid deposit on the surface allows inward S access, and outward Co/Ni transport. This form of attack often results in pitting damage with an outer NiO/CoO layer being formed, although sometimes a form of broad fronted attack develops [5, 6].

For type II hot corrosion many researchers have noted the importance of a constant SO_x supply for sustained corrosion to occur[3, 7, 9, 10]; this variation of the damage mechanism is known as gas induced acidic fluxing [8, 11]. Without both gaseous SO_x and a regular sulphate deposition flux, the corrosion reaction would cease to occur when all the reactants have been consumed.

Type II hot corrosion combined with static stress in Ni-based superalloys has not been extensively studied. However, stress corrosion cracking (SCC) is a well-documented failure mechanism especially in aqueous systems [12, 13].

Studies have been conducted on the effects of stress on corrosion pitting growth in aluminium alloys [14]. It was found that corrosion pit growth could be affected by time, stress amplitude and frequency in a fatigue environment. The methodology of Ishihara et al [14] was applied to Ni-based superalloys by Chan et al [15]. They considered the point at which fatigue crack growth exceeds corrosion pit growth. However, neither of these studies consider the effect of hot corrosion on the materials stress intensity threshold ($\mathrm{K_{th}}$), the threshold below which cracking does not occur.

Finite element analysis (FEA) is a commonly used method to calculate stresses within complex geometries or multiaxial loading states. This is done by meshing the geometry as a net of elements and nodes. The elements can deform as constrained by the material model, whereas the load is transferred from element to element through the node connections. FEA has been widely used to assess the stress in statically and cyclically loaded condition.

2.2. Experimental method

2.2.1. C-ring test method

C-ring specimens were manufactured from CMSX-4 bars. Guidelines for the dimensions were taken from ISO 7539-5 [16]. The final dimensions for the specimens used in this testing are given in Figure 2.1. C-ring specimens where manufactured with a <001> crystallographic orientation aligned with the cylinder axis.

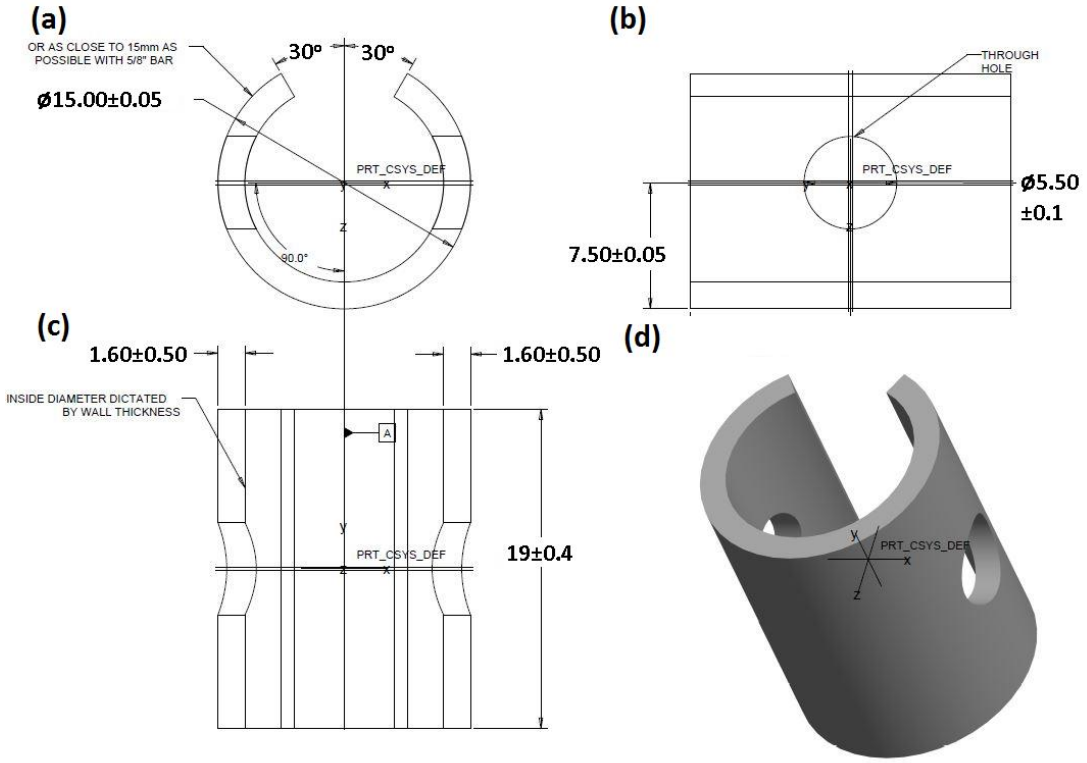

Figure 2.1: C-ring specimen geometry as established from ISO 7539-5 (a) frontal cross section (b) top view cross section (c) side view cross section (d) isometric view

For target stress levels at a constant strain the required displacement of the C-rings were calculated by first calculating the change in diameter (*ΔD*) required to achieve a given stress (Equation 2.1).

Equation 2.1: Change in diameter from ISO 7539-5 [16]

$$\Delta D = \sigma \pi d^2 / 4EtZ$$

FEA modelling was used to verify the stress calculations. Surrogate data from Siebörger et al [17] for CMSX-4 provided the young's modulus (*E*) for Equation 2.2 and the monotonic material properties used in FEA modelling. The final stressed diameters (*Df*) were calculated using Equation 2.2: Final stressed diameter

$$D_f = D_{AV} - \Delta D$$

The C-rings were clamped to the final diameter (D_f) using A2 grade stainless steel M5 nuts, bolts and washers, and measured using a digital micrometre with a resolution of 1 µm (and accuracy of 2 µm).

An average of five readings was used to determine both the initial external diameter (D_{AV}) from which the final stressed diameter is calculated these are given in Table 2.2.

Prior to testing, C-ring samples were cleaned in an ultrasonic bath with IPA (isopropyl alcohol). Corrosion exposures were carried out in a horizontal controlled atmosphere furnace. The corrosion environment, deposit composition and deposit flux were controlled using the well-established deposit recoat methodology (eg Sumner et al [3]). Specimens were coated with an 80/20 molar mixture of Na_2SO_4/K_2SO_4. The mass of deposited salt was measured per unit area and specimens were recoated every 100 h in order to control the deposition flux. A gaseous environment of air - 300 vppm SO_2 was used, and all testing was conducted at 550 °C. C-rings were stressed to 800, 700 and 500 MPa, and exposed for 100, 300 or 500 hour exposure times with a target deposition flux of 5 µg/cm^2/h. In addition, one C-ring at each target stress level was exposed for 300 hours without any deposit.

2.2.2. Microscopy and analytical methods

Samples were mounted in a 50:50 mixture of MetPrep's epoxy set resin and ballotini (40-70 µm diameter glass spheres). Samples were then sectioned, using oil lubricant to prevent dissolution of corrosion products and deposits, before being ground and then polished to a 1 µm diamond paste finish (again using oil lubricant).

Both optical and SEM examinations of the samples were carried out. Optical microscopy was used to determine if cracking was present in the C-rings after each exposure period. SEM was used to characterise the results of the degradation mechanism's interaction with the alloy microstructure. FEI XL-30 and a JEOL 7800F field electron gun (FEG) SEMs equipped with backscatter energy-dispersive X-ray (EDX) detectors were used for characterisation and SEM imaging. SEM images were post-processed using Image J software to enable accurate measurement of features.

2.3. FEA Analytical methods

FEA modelling was conducted using ANSYS Workbench 15 [18]. The material model used for this analysis was an isotropic model generated using monotonic surrogate material data for CMSX-4 from Siebörger et al [17]. The C-ring was constrained between two plates (Figure 2.2.2). A frictionless sliding contact was utilised between one of the two blocks and the C-ring in order to allow a small amount of relative movement. The boundary conditions were applied through a displacement equivalent to those calculated using equation 2.1 and are tabulated in Table **2.3**.

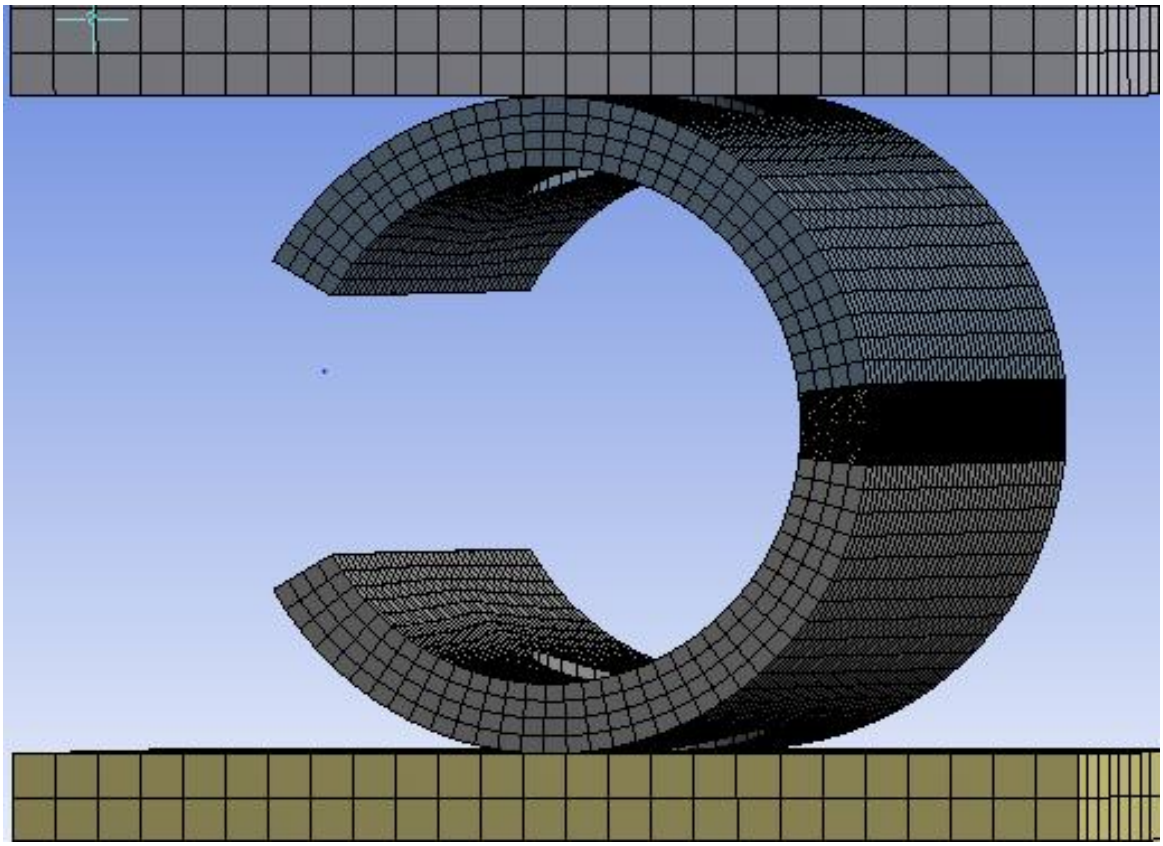

Figure 2.2: Example of a C-ring mesh constrained between two plates

The C-ring was modelled as three separate sections to allow more accurate refinement of the mesh in the central section of the C-ring. This was important as it was in this central region that it was anticipated that cracking could occur. A hex dominant mesh is used wherever possible; however meshing around the crack tips required the use of a tetrahedral mesh due to the size and complexity of the crack tip geometry. A semi elliptical crack was used within the FE model with an aspect ratio (a/w) of 0.5.

When clamped, a multiaxial stress condition was predicted in the C-ring. As such the von Mises criterion was used to obtain local stress values. However it was also useful to consider the principal or normal stresses in relation to a mode I crack opening, as shown in Figure 2.3, as these stresses could be higher for the C-ring geometry in the principal x-axis plane when compared with the von Mises stress.

Linear elastic fracture mechanics (Equation 2.3) was used to assess the local stress intensity range (ΔK) for micro semi-elliptical cracks within the C-ring. The stress intensity was assessed using the ANSYS R15 [18] stress intensity solver code. ANSYS uses J-integral evaluation [19] in order calculate the local crack tip stress intensity.

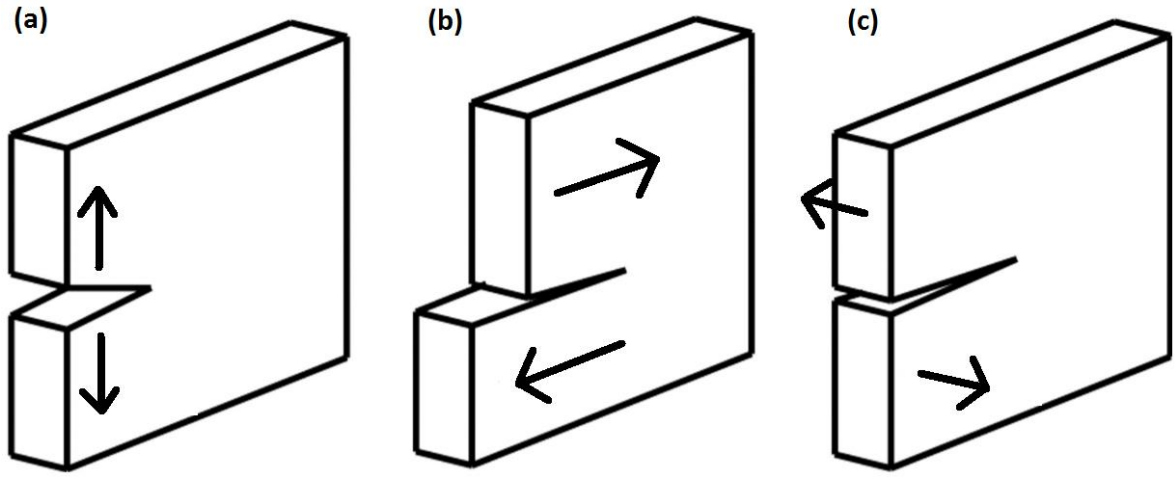

Figure 2.3: Crack opening modes (a) mode I (b) mode II and (c) mode III

Equation 2.3: Linear Elastic Fracture Mechanics Equation [20]

$$\Delta K = \Upsilon \sigma \sqrt{\pi a}$$

FEA generated local crack tip stress intensity predictions were then used to calculate the geometry factor (Υ) for finite surface cracks in the C-ring geometry. ΔK Can then be compared to K_{th} to assess the likelihood of cracking. The K_{th} of CMSX-4 has been reported to be 15 MPa.m$^{1/2}$ in air at 750 °C [21]. Stress intensities calculated through FEA modelling can be compared to this in order to determine the likelihood of cracking and the effect of hot corrosion on K_{th}.

2.4. Results and discussion

2.4.1. C-ring results & discussion

Unstressed sections of CMSX-4 C-rings were corroded at 550 °C with a target deposition of 5 µg/cm^2/h and a gaseous environment of air - 300 vppm SO_2. Samples were removed after exposure times of 100, 300 and 500 hours. Inspection showed formation of an oxide scale containing Co, Ni, S and O (Figure 2.4, Figure 2.5). Sulphidation had occurred beneath the oxide scale, consistent with type II hot corrosion [7][22].

For stressed C-rings, cracking of corroded samples was observed at 800, 700 and 500 MPa after exposures 100 h; with visible cracking still occurring at 500 MPa for exposure times longer than 100 h (Table 2.2). By contrast C-ring tests without deposit showed no signs of cracking after 500 h of exposure to the test conditions.

C-rings normally experienced cracking within the most highly stressed central region. However when cracks initiated off centre, cracking would occur either side of the centre line due to the shifted stress distribution around the C-Ring (Figure 2.6).

The corrosion mechanism varied from attacking the gamma-prime (γ') to attacking the gamma-matrix (γ). This is visible in SEM backscattered imaging as a shift in the contrast between the two

microstructural features (Figure 2.7). This reduction in back scattered electrons is attributable to the lower atomic number of the S and O present in the corrosion products.

SEM imaging suggests that the initial combined presence of stress and hot corrosion results in the reaction of the γ' precipitates. Cracks then initiate from features similar to corrosion pit features (Figure 2.7) and propagate through the γ' where corrosion is present (Figure 2.8). Using the results of EDX analysis (Figure 2.5) it is hypothesised that this is because of the lower Cr and Co content of the γ' precipitates. The corrosion attack shifts to the γ, and it is hypothesised that this happens when the protective NiO/CoO rich oxide scale is formed, as this depletes Co from the alloy which is mainly concentrated in the matrix.

Table 2.2: C-ring visible cracking results

Stress (MPa)	Exposure (Hours)	Final Flux (μg/cm^2/hr)	Cracking Observed	Average Diameter	Stressed Diameter
800	500	5.1	Yes	15.02	14.40
800	300	5.1	Yes	15.01	14.39
800	300	0.0	No	15.03	14.40
800	100	5.0	Yes	15.02	14.40
700	500	5.2	Yes	15.01	14.47
700	300	4.7	Yes	15.05	14.50
700	300	0.0	No	15.01	14.47
700	100	5.2	Yes	14.99	14.46
500	300	0.0	No	15.03	14.64
500	100	5.0	No	14.98	14.59
500	300	5.0	Yes	15.02	14.63
500	500	5.2	yes	15.02	14.63

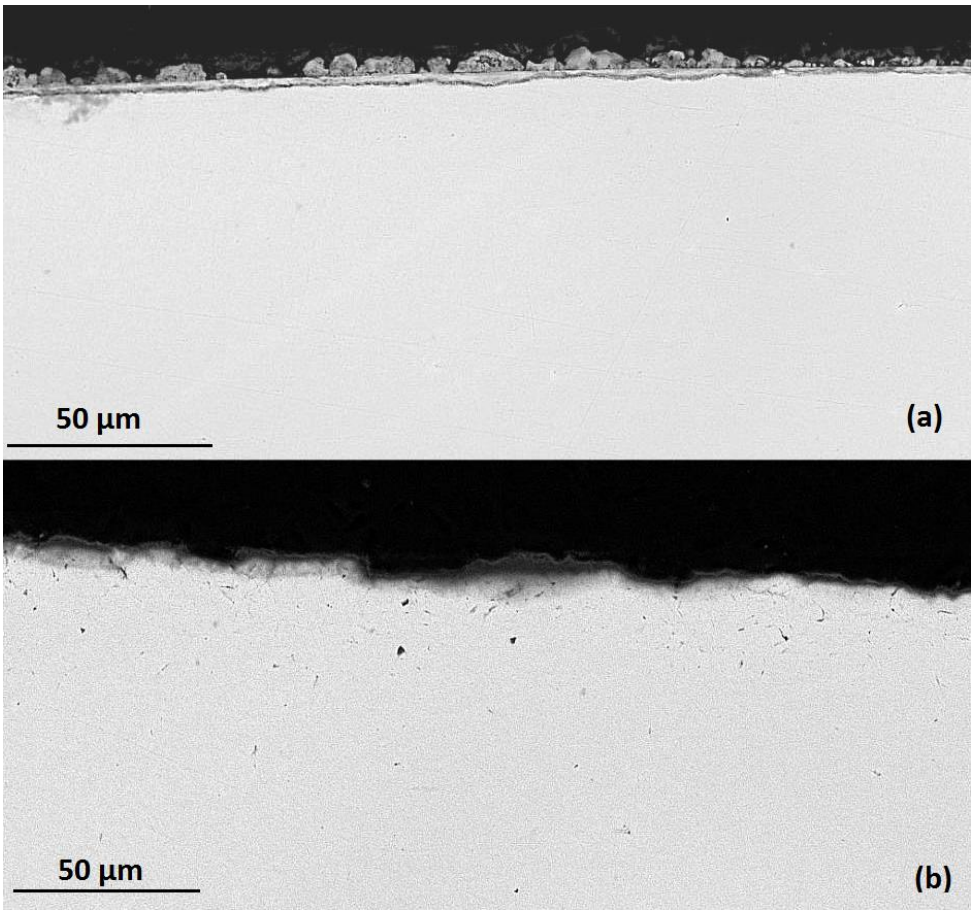

Figure 2.4 : Un-stress C-ring surface, showing corrosion product at 550 °C and exposed to 5 µg/cm^2/h with a test gas of air - 300 vppm SO_2 (a) 500 h resulting in 7.7 µm oxide scale (b) 100 h exposure resulting in 2.43 µm oxide scale

2.4.2. FEA principal and von Mises stress state modelling in C-rings

FEA modelling predicted that maximum stress occurred in the central region of the C-ring as shown in Figure 2.9. FEA also predicted the presence of a multi-axial stress state within the C-ring, where the largest resolved principal stress plane referred to as maximum principal occurs along the x-axis, and the second largest resolved stress plane referred to as middle principal occurs in along the z-axis. This stress state would suggest cracks would firstly initiate and then propagate in the Z-axis where the maximum principal is acting at a normal in mode I crack opening. However as cracks propagate and ΔK exceeds K_{th} then secondary cracks could propagate in all three principle directions. A summary of the stress conditions for various *ΔD* values is given in Table **2.3Table 2.3: Calculated stress conditions from ISO 7539-5 and FEA modelling stress results**

Required Pre Stress (MPa)	ΔD Calculated Using ISO 7539-5 (µm)	FEA Maximum von Mises Stress (MPa)	FEA Maximum Principle Crack Opening Stress (MPa)
800	621.0	815	930
700	544.0	712	814
600	466.0	611	693

500	388.0	508	580

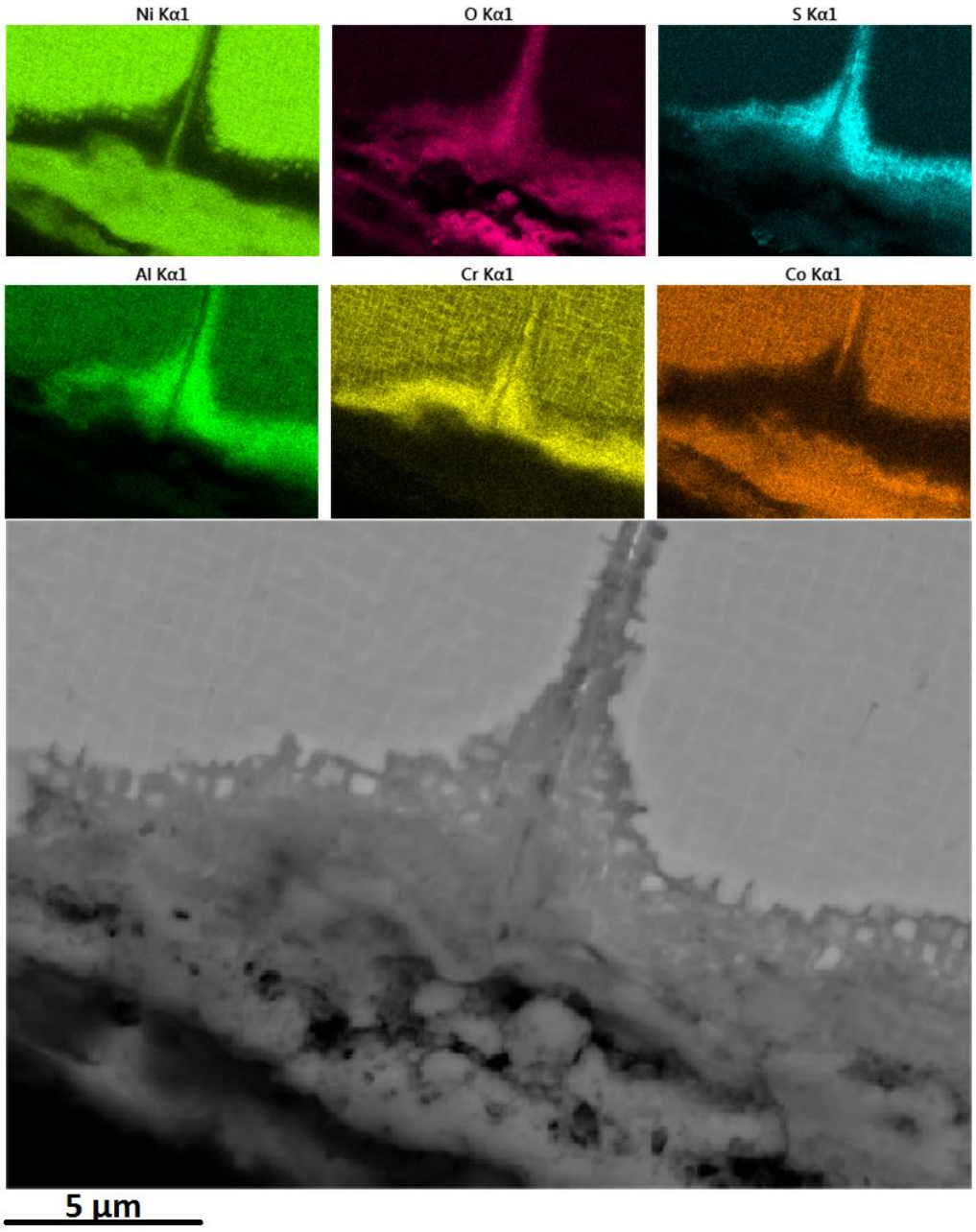

Figure 2.5 : Surface corrosion fatigue crack and back scattered EDX characterisation at 800 MPa after 300 h with a 5 µg/cm^2/h deposition flux and a test gas of air - 300 vppm SO_2

Crack body modelling FEA was further used to predict the stress intensity and concentration around a crack tip (Figure 2.10) within the C-ring geometry. These micro-cracks were modelled in the central region of the C-ring using a refined tetrahedral mesh; the results are presented in Table 2.4.

Table 2.4: Stress intensity FEA results

Peak Surface von Mises Stress (MPa)	Crack Length (µm)	Peak Mode I Stress Intensity ΔK (MPa.m$^{1/2}$)	Calculated Geometry Factor Y

890	50	9.28	0.832
890	100	13.11	0.831
500	1	0.74	0.837
500	50	5.27	0.841
500	100	7.44	0.839

FEA stress intensity modelling suggests that cracks or pits need to be greater than 100 µm for cracking to occur given a K_{th} of 15 MPa.m$^{1/2}$, as the reported fatigue threshold for CMSX-4 [21]. Therefore the presence of hot corrosion may have a significant effect on reducing the materials K_{th} as well as concentrating stress through corrosion pitting.

Analysis of a corrosion pit's size in cracked C-ring specimen implies that a 10 µm diameter pit has initiated cracking during these exposures (Figure 2.7).

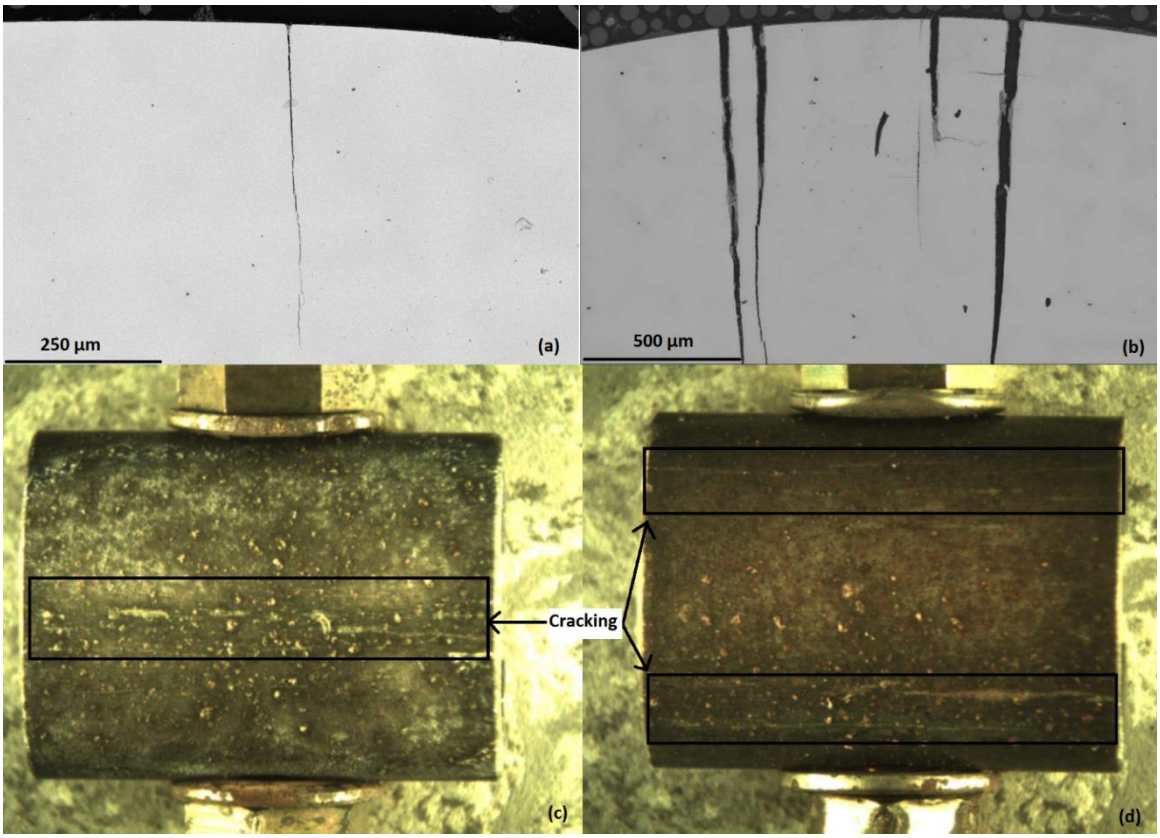

Figure 2.6 : Cracking of C-rings at 800 MPa with a 5 µg/cm^2/h deposition flux and a test gas of air - 300 vppm SO_2 (a) 100 h exposure cross section (b) 300 h exposure cross section (c) 300 h central cracking (d) 500 h symmetrical cracking

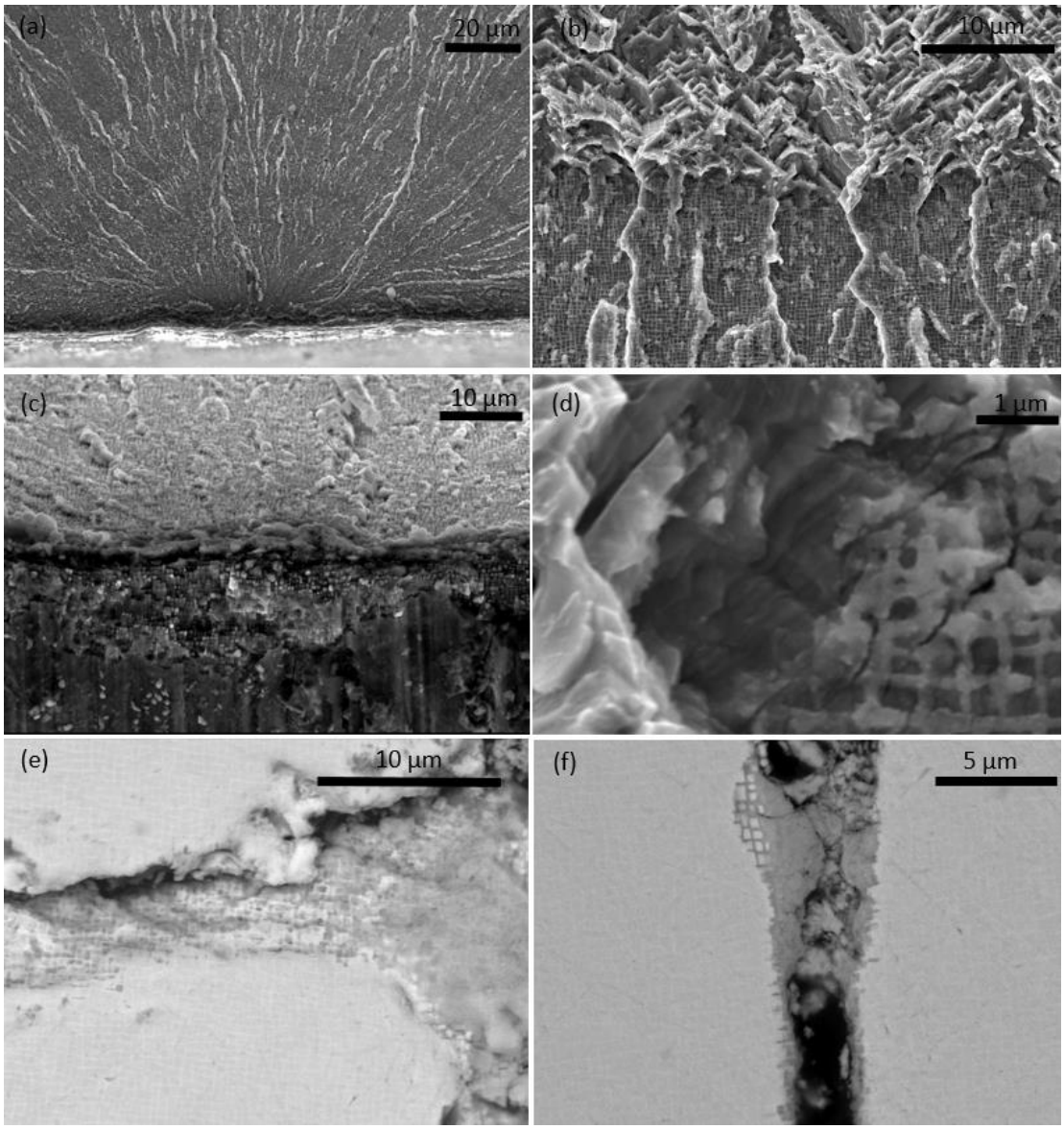

Figure 2.7 : Secondary electron images of 800 MPa C-ring with a 5 µg/cm^2/h deposition flux and a test gas of air - 300 vppm SO_2 (a) 100 h fracture face showing signs of beaching marks (b) 100 h fracture face, crack tip showing attack of γ' (c) 100 h specimen surface showing attack of γ (d) 100 h high mag fracture surface at crack tip (e) 300 h corrosion attack of γ' precipitate (f) 500 h corrosion attack of γ matrix

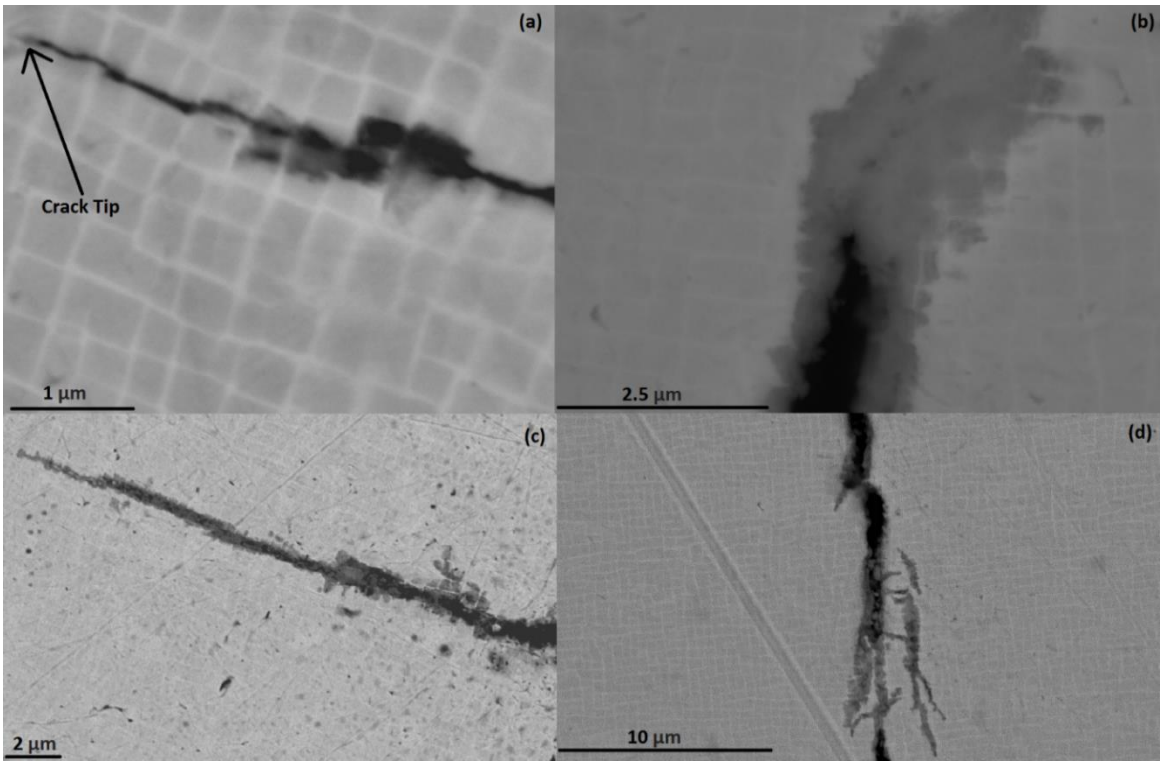

Figure 2.8 : SEM images near crack tips from CMSX-4 C-ring samples stressed to 800 MPa and exposed to a corrosion environment with a deposit flux of 5 µg/cm^2/h and test gas of air – 300 vppm SO_2 (a) 300 h exposure (b) 300 h exposure (c) 300 h (d) 100 h exposure

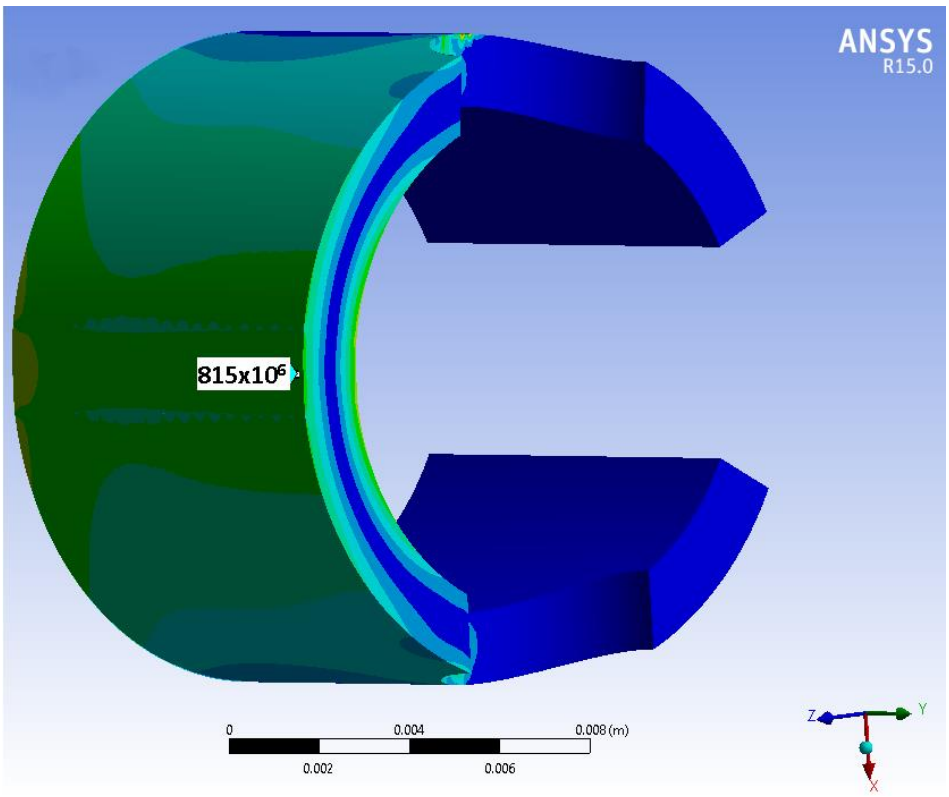

Figure 2.9 : Axis orientation for C-ring modelling, showing normal stress distribution within a C-ring in the principal x-axis, for a boundary condition of ΔD= 0.612 mm

Using the FEA calculated geometry factor Υ of 0.836. This gives a theoretical reduced K_{th} of 3.748 MPa.m$^{1/2}$ when hot corrosion is simultaneously acting with a stress of 800 MPa, a 75% reduction. This means that cracking can occur at considerably lower applied stresses.

A Kitagawa diagram [23] has been plotted to demonstrate the stress and crack or defect size needed to exceed the materials k_{th} (Figure 2.11). This is done both for the calculated theoretical K_{th} in hot corrosive conditions, and using the reported K_{th} for air.

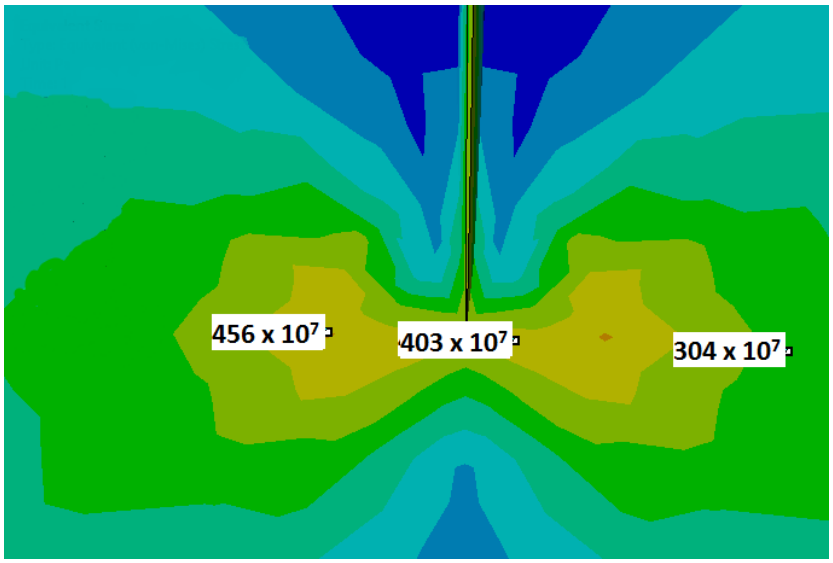

Figure 2.10 : Stress distribution around a centrally located 100 µm crack tip in a C-ring at 890 MPa

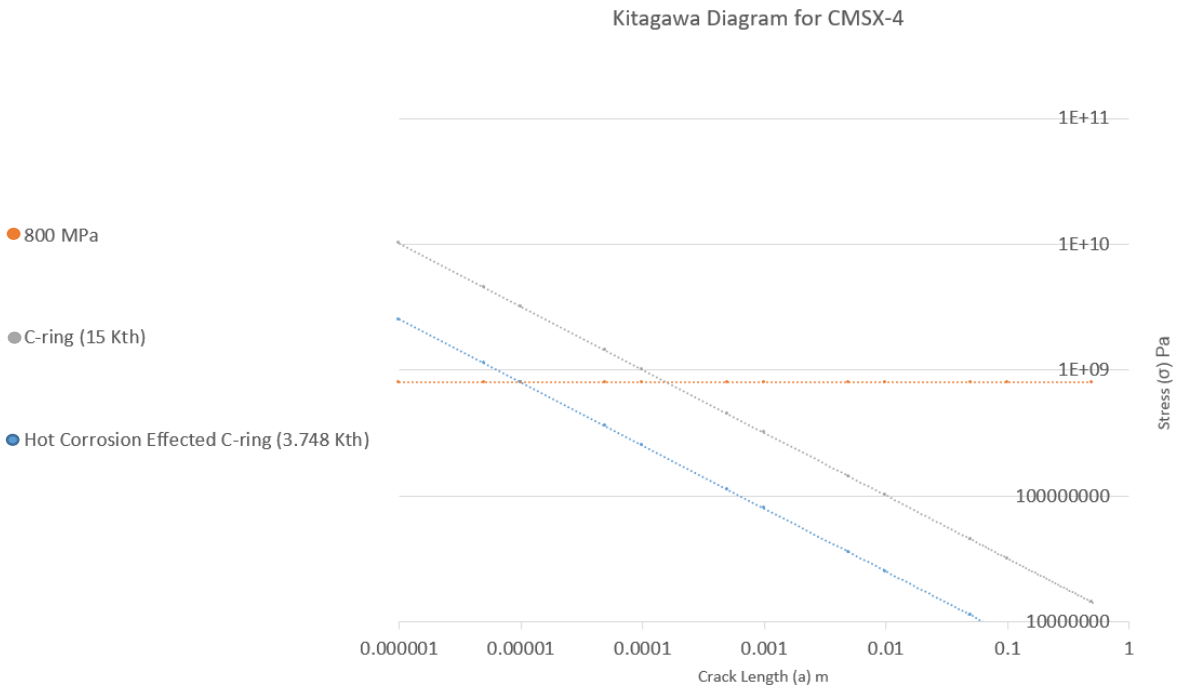

Figure 2.11: Kitagawa diagram produced from FEA corrosion crack stress intensity analysis, showing the crack defect size required to initiate cracking both with and without the presence of hot corrosion

2.5. Paper 1 conclusions

SEM/EDX characterisation of the corrosion product produced by stress corrosion in CMSX-4 C-rings at 550 °C is consistent with type II hot corrosion.

Hot corrosion conditions at 550 °C combined with static stresses of greater than 500 MPa can cause a significant hot corrosion stress cracking mechanism. A lower limit seems to exist around 500 MPa. However at exposures greater than 100 hours with a flux of 5 μg/cm^2/h cracking is still visibly present.

FEA modelling predicts the multiaxial nature of the stress state within a clamped C-ring and the observed cracking in experimental testing supports the modelling results. By determining the effective stress through the von Mises criterion, FEA calculated equivalent stress concurs with that from ISO 7539-5.

FEA stress intensity modelling around crack tips estimates that fatigue/fracture (K_{th}) can be reduced by up to 75% with the combined effect of hot corrosion in CMSX-4.

SEM imaging suggests the combined hot corrosion stress mechanism initially attacks γ' precipitates, cracks then propagate through precipitates as the mechanism attacks features ahead of its propagation path. A switch to attack of the γ matrix is observed, it is hypothesised that this occurs in order to form the NiO/CoO oxide scale which depletes Co from the γ matrix.

Acknowledgements

The authors acknowledge the support of the Engineering and Physical Research Council (EPSRC) for their support for the project - Flexible and Efficient Power Plant: Flex-E-Plant (Grant number: EP/K021095/1). They also thank the following partners for their the valuable contributions: GE Energy, Doosan Babcock Limited, Centrica plc., EDF Energy (West Burton Power) Limited., Uniper Technology Limited, Goodwin Steel Castings Limited, NPL Management Limited, R-MC Power Recovery Limited., RWE Generation UK plc., Scottish and Southern Energy (SSE) plc., Siemens Industrial Turbomachinery, and TWI Limited.

2.6. Paper 1 references

[1] M. M. Rahman, T. K. Ibrahim, and A. N. Abdalla, "Thermodynamic performance analysis of gas-turbine power-plant," *Phys. Sci.*, vol. 6, no. 14, pp. 3539–3550, 2011.

[2] K. Harris and J. B. Wahl, "Improved single crystal superalloys, CMSX-4 (SLS) [La+Y] and CMSX-486," *Superalloys 2004 (Tenth Int. Symp.*, no. Figure 1, pp. 45–52, 2004.

[3] J. Sumner, A. Encinas-Oropesa, N. Simms, and J. R. Nicholls, "Type II hot corrosion: Behaviour of CMSX-4 and IN738LC as a function of corrosion environment," *Mater. Corros.*, no. 2, pp. 188–196, 2014.

[4] K. L. Luthra and O. H. LeBlanc, "Low Temperature Hot Corrosion of Co-Cr-AI Alloys*," *Mater. Sci. Eng.*, vol. 87, pp. 329–335, 1987.

[5] N. Birks, G. H. Meier, and F. S. Pettit, "High-Temperature Corrosion Resistance," *JOM*, vol. 39, no. 12, pp. 28–31, 1987.

[6] J. R. Nicholls and N. J. Simms, "Gas turbine oxidation and corrosion," in *Shreir's Corrosion*, 2010, pp. 518–540.

[7] D. Young, "High Temperature Oxidation and Corrosion of Metals," in *Elsevier Corrosion Series*, vol. 1, 2015, p. 576.

[8] N. Eliaz, G. Shemesh, and R. M. Latanision, "Hot corrosion in gas turbine components," *Eng. Fail. Anal.*, vol. 9, no. 1, pp. 31–43, 2002.

[9] J. A. Goebel and F. S. Pettit, "Na2SO4-induced accelerated oxidation (hot corrosion) of nickel," *Metall. Trans.*, vol. 1, no. 7, pp. 1943–1954, 1970.

[10] P. Lortrakul, R. W. Trice, K. P. Trumble, and M. A. Dayananda, "Investigation of the mechanisms of Type-II hot corrosion of superalloy CMSX-4," *Corros. Sci.*, vol. 80, pp. 408–415, 2014.

[11] K. L. Luthra, P. A. Begman, D. J. Wortman, and R. E. Fryxell, "MECHANISM OF LOW TEMPERATURE HOT CORROSION: BURNER RIG STUDIES," *Thin Solid Films*, vol. 64, pp. 281–288, 1979.

[12] N. S. Zadorozne, M. C. Giordano, A. E. Ares, R. M. Carranza, and R. B. Rebak, "Anodic characteristics and stress corrosion cracking behavior of nickel rich alloys in bicarbonate and buffer solutions," *Corros. Sci.*, vol. 108, pp. 1–10, 2016.

[13] O. K. Chopra, W. K. Soppet, and W. J. Shack, "Effects of Alloy Chemistry , Cold Work , and Water Chemistry on Corrosion Fatigue and Stress Corrosion Cracking of Nickel Alloys and Welds," *Corrosion*, p. 50, 2001.

[14] S. Ishihara, S. Saka, Z. Y. Nan, T. Goshima, and S. Sunada, "Prediction of corrosion fatigue lives of aluminium alloy on the basis of corrosion pit growth law," *Fatigue Fract. Eng. Mater. Struct.*, vol. 29, no. 6, pp. 472–480, 2006.

[15] K. S. Chan, M. P. Enright, and J. P. Moody, "Development of a Probabilistic Methodology for Predicting Hot Corrosion Fatigue Crack Growth Life of Gas Turbine Engine Disks," *J. Eng. Gas Turbines Power*, vol. 136, no. 2, p. 22505, 2014.

[16] ISO 7539-5, “Corrosion of metals and alloys - Stress corrosion testing - Part 5: Preparation and use of C-ring specimens,” no. 1, 1989.

[17] D. Siebörger, H. Knake, and U. Glatzel, “Temperature dependence of the elastic moduli of the nickel-base superalloy CMSX-4 and its isolated phases,” *Mater. Sci. Eng. A*, vol. 298, no. 1–2, pp. 26–33, 2001.

[18] “ANSYS Workbench 15.0.” ANSYS, 2013.

[19] M. Gupta, R. C. Alderliesten, and R. Benedictus, “A review of T-stress and its effects in fracture mechanics,” *Eng. Fract. Mech.*, vol. 134, pp. 218–241, 2015.

[20] N. E. Dowling, *Mechanical Behavior of Materials*, 4th ed. Boston, MA : Pearson, 2012.

[21] M. R. Joyce, X. Wu, and P. a S. Reed, “The effect of environment and orientation on fatigue crack growth behaviour of CMSX-4 nickel base single crystal at 650 °C,” *Mater. Lett.*, vol. 58, no. 1–2, pp. 99–103, 2004.

[22] R. B. Bird, W. E. Stewart, and E. N. Lightfoot, “Transport Phenomena,” *J. Wiley*, 2007.

[23] J. Maierhofer, H. P. Gänser, and R. Pippan, “Modified Kitagawa-Takahashi diagram accounting for finite notch depths,” *Int. J. Fatigue*, vol. 70, pp. 503–509, 2015.

3. Paper 2: Interaction of hot corrosion fatigue and load dwell periods on a nickel-base single crystal superalloy

L.Brooking*, S.Gray, J.Sumner, J.R.Nicholls, N.J.Simms

*Corresponding Author: l.b.brooking@cranfield.ac.uk

Cranfield University, College Road, Cranfield, MK43 0AL, UK

Abstract. The effects of type II hot corrosion on the fatigue resistance of turbine blade superalloys is of growing interest as gas turbine (GT) original equipment manufacturers (OEMs) strive to optimise the operational efficiencies and versatilities of GT systems. Hot corrosion fatigue has been observed in the under platform regions of first stage GT blades, this location is subject to both relatively high principal stresses and stress gradients, combined with temperatures up to those associated with type II hot corrosion (500 °C-700 °C). The effects of the deposition flux of corrosive salt species and the tensile stress dwell period on the fatigue performance and resultant crack morphologies of single crystal (SC) superalloy CMSX-4 has been studied at 550 °C. Deposit recoat methodologies were applied to specimens that were cyclically fatigued with a load-controlled trapezoidal waveform. It was observed that introducing a longer dwell period increased the number of {100} crack initiations and reduced the fatigue life (load cycles to failure). Optical and SEM microscopy and EDX techniques were used to examine specimen fractography, and mechanisms of crack advance and propagation discussed.

Keywords: Hot corrosion, Fatigue Dwell Period, Single Crystal Superalloy

3.1. Introduction

Gas turbines (GTs) are used for a range of power generation applications; some of the more common being industrial power generation and aviation engines. With GTs relevance to the future of energy and aerospace industries looking to remain high [1], and demand for GTs to generate sustainable clean and efficient power being significant [2][3][1], GT original equipment manufacturers (OEMs) are constantly striving to optimise operation and efficiencies. One of the key limiting factors effecting the power density and thermal efficiencies that can be achieved by GTs is the operational gas temperatures reached in the turbine section of the engine. These gas temperatures are largely limited by the material capabilities in the following areas; high temperature oxidation/corrosion performance, and high temperature mechanical performance such as creep and fatigue [4]. Often blade cooling is used in first stage turbines in order to reduce the blade temperatures and improve the mechanical properties, however the increasing temperatures can result in the extended effect of hot corrosion. In addition to increasing temperatures the low cycle fatigue (LCF) duty cycles GTs are subjected to can also be intensified as a result of increased multi start up and shut down procedures. This can be as a result of increased

renewables and peak loads on the energy grid in the case of industrial GTs, and increased short haul flights in the case of aviation engines. These combined factors provide the motivation for conducting combined hot corrosion fatigue testing.

Due to the importance of the high temperature material properties and degradation models for GT component design, there is a large amount of research available and a good understanding of them [5][6][7]. However, whilst it has been observed [8], the interactions and mechanisms generated as a result of combined hot corrosion and mechanical fatigue is not currently a heavily researched area and as such there is a limited understanding of these interactions. As a result, combined material degradation mechanisms not predicted by current design life methods have resulted from simultaneous hot corrosion and mechanical fatigue [9]. Type II hot corrosion has been reported to both assist crack initiation due to corrosion pitting, and accelerate fatigue crack propagation [10]. The work presented in this paper focuses on type II hot corrosion and fatigue interactions, and studies the effect of extended dwell periods on fatigue life in the single crystal turbine blade alloy CMSX-4. Dwell effects on hot corrosion fatigue have been studied in a disk alloy [11], it was found that increased dwell resulted in a decrease in fatigue life, which was attributed to time dependant mechanisms such as crack tip oxidation. This paper further hypothesises that this effect could in part be due to additional crack growth occurring in a period of static load, such as a fatigue dwell period. This hypothesis is informed by previous research showing that cracks can initiate and propagate under static loads when combined with type II hot corrosion [12][13]. Dwell periods were introduced using a trapezoidal waveform, on the first stage turbine blade material, single crystal nickel based superalloy CMSX-4 (Table 3.1).

Table 3.1: Composition of CMSX-4 (wt%), Ni Bal.

Cr	W	Co	Mo	Al	Ti	Ta	Re	Hf
6.5	6.0	9.6	0.6	5.6	1.0	6.5	3..0	0.1

Type II hot corrosion is induced through salt deposition combined with a regular supply of SO_x [14]. Salt species typically deposit on the surface of GT components, forming low melting point mixtures with alloying elements. This mechanism commonly produce corrosion products rich in $CoSO_4$ and $NiSO_4$ for nickel-based superalloys such as CMSX-4 [15][16]. In gas turbines, sulphur can be introduced into the system through both fuel and air contaminants. However salt species are normally introduced into the turbine via the air intake; this can be in the form of particulate or liquid matter, which can then deposit onto turbine components via two mechanisms. The salt species can either be vaporised or sublimated in the combustion process, and then condense onto turbine components, this is commonly referred to as vapour deposition [17]. Additionally, salt species can deposit due to particles sticking onto turbine components; resulting in a build-up of deposit [18]. A combination of these mechanisms can occur depending on the temperatures and pressures at certain locations in the turbine, a model for similar deposition mechanisms in pulverised coal boilers was proposed by Tomeczek et al [19].

The effect of the deposition flux of corrosive salts on the fatigue resistance and resulting crack morphologies of single crystal (SC) superalloy CMSX-4 was previously experimentally studied at 550°C [13]. It was found that an increase in the deposition flux had a detrimental effect on the

fatigue resistance of CMSX-4. Additionally, the increase in flux generated a shift in the crack propagation plane from the conventional {111} slip systems [20][21], to a orthogonal {100} propagation. This was observed in plane cylindrical specimens with no stress concentration. This behaviour was associated with the orthogonal corrosion attack and embrittlement of the primary gamma-prime strengthening phase at the crack tip.

The stability of a crack under fatigue loading can be simplistically assessed through the use of linear elastic fracture mechanics (LEFM) [22]. In order for fatigue crack propagation to occur the stress intensity has to overcome the fatigue threshold value (K_{TH}). For CMSX-4 at a temperature of 550 ^{o}C this has been determined to be in the range of 15 $\mathrm{MPa}\sqrt{\mathrm{m}}$ [23].

Conventional fatigue is defined as occurring in three stages defined as follows [25][26]. Stage 1 is defined as crack nucleation and initiation and is arguably the least well understood and most heavily researched area of fatigue. Crack nucleation and initiation is thought to occur due to cyclic loading causing shear slip and resulting in the generation and accumulation of micropours which initiate a fatigue crack. Stage 2 is the propagation stage which is arguably the most well understood stage and can be simplistically modelled using Paris law and fracture mechanics. Fatigue crack propagation is thought to occur due to cyclic loading generating plastic slip which results in dislocation emissions ahead of the crack tip. Stage 3 is the final rupture stage where the reduction in cross-section leads to mechanical over load.

3.2. Methodology

3.2.1. Experimental methodology

Accelerated type II hot corrosion conditions were generated by depositing an 80/20 mol% mix of Na_2SO_4 /K_2SO_4 over 100 h intervals in order to maintain a consistent deposition flux. A test gas of 300 ppm SO_x and air was passed through the test chamber to maintain a partial pressure of SO_x. Specimens were subjected to a temperature of 550 ^{o}C via radiated heat from a sheath which was in turn induction heated (Figure 3.1). Specimens were pre-corroded for 500 h with either a 1.25 or 5 µg/cm^2/h flux.

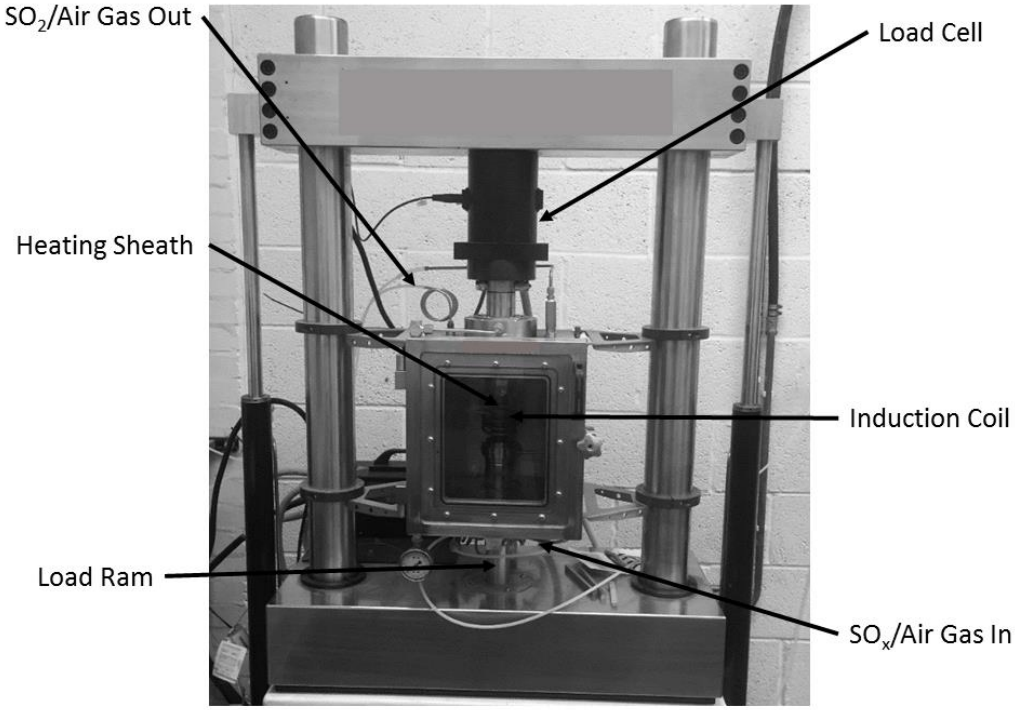

Figure 3.1: Cranfield load controlled corrosion fatigue rig

The specimens used were cylindrical plain specimens oriented in the [001] direction, meaning the [001] axis is aligned to the length of the cylindrical gauge length of the specimen to within a tolerance of ±20°. Therefore the crystallographic groups for directions and planes can be determined from this known [001] axis alignment. The cylindrical gauge length of 6 mm diameter generates a uniaxial stress state within the specimen.

The procedure used for fatigue testing is outlined in Figure 3.2 where all specimens were exposed for 500 h of pre corrosion in order to accelerate the corrosive environment. Fatigue specimens were subjected to a fully tensile un-reversed (R=0) trapezoidal load controlled waveform (Figure 3.3). The waveforms used were 1-1-1-1 s and 1-60-1-1 s. Fatigue cycles were controlled through a servo hydraulic load feedback control loop and S-N curves were plotted for stress levels between 700 – 850 MPa.

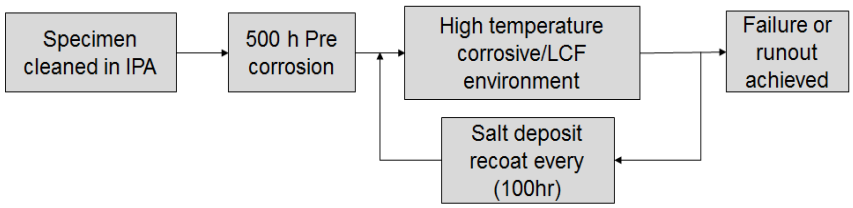

Figure 3.2: Flow chart outlining the type II hot corrosion fatigue testing procedure

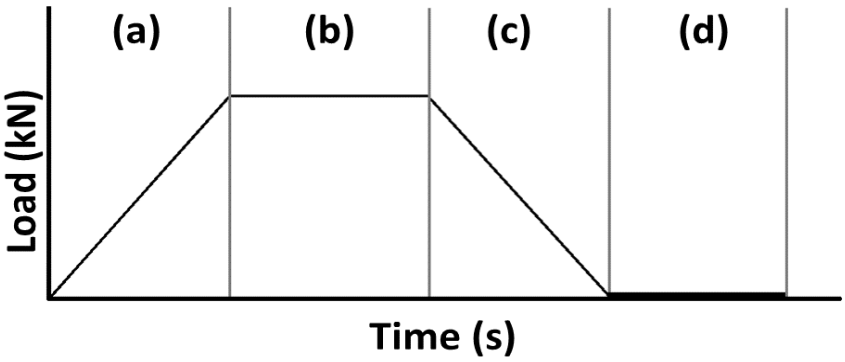

Figure 3.3: Trapezoidal Load Wave Form: **(a)** Ramp up period, **(b)** Maximum stress dwell period, **(c)** Ramp down period, **(d)** Minimum load dwell period

3.2.2. Analytical methodology

Post testing specimens were examined using scanning electron microscopy (SEM) and characterised with energy dispersive X-rays (EDX). Both Phillips FEI XL-30 and JEOL 7800F systems were used to analyse fracture surfaces and cross-sections. Cross-sections were mounted in a 50:50 mixture of epoxy resin and ballotini (40-70 µm diameter glass beads), then polished using oil lubricant to preserve the corrosion products.

Analysis of the banding observed on fracture faces was conducted using Image-J [27] to assess crack propagation paths and environmentally induced banding spacing.

3.3. Results

3.3.1. Experimental results

For the 5 µg/cm^2/h deposition flux curves a reduction in fatigue life of up to four times was observed with the introduction of a 60 s dwell period (Figure 3.4). However as the gradient of the 60 s dwell curve is shallower than that of the 1-1-1-1 curve. It should be noted that dwell has a detrimental effect on fatigue life, and the data suggests that this is more marked at higher stresses.

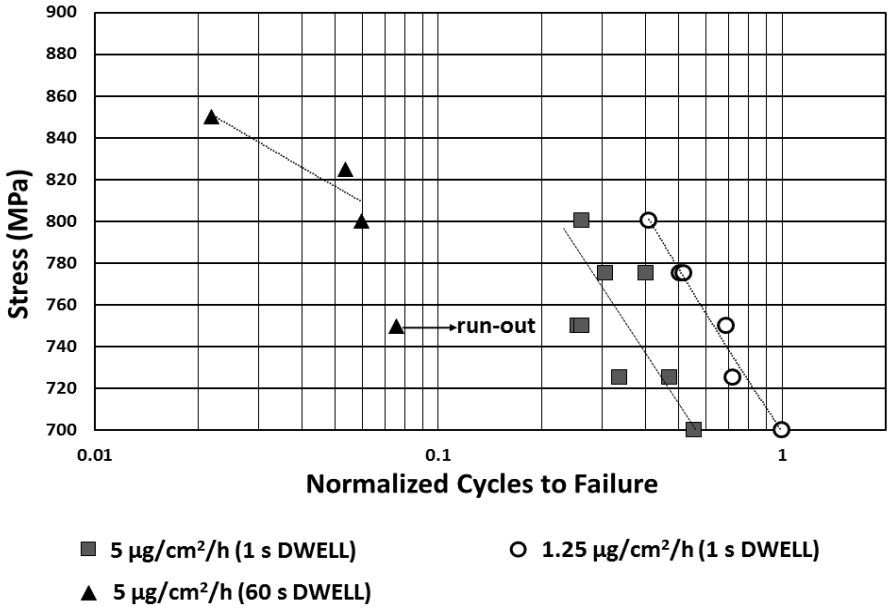

Figure 3.4: Normalised cycles to failure S-N curve, 1s dwell curves are previously presented in [13]

To provide an additional comparison, the 1.25 and 5 µg/cm^2/h deposition flux curves for 1-1-1-1 cycle has been included, as previously presented in [13]. It can be seen that the relative effect of dwell from 1-1-1-1 to 1-60-1-1 is significantly greater than the increased flux from 1.25 to 5 µg/cm^2/h.

When considering the time to failure, due to the increased cycle length of the 1-60-1-1 waveform compared with that of the 1-1-1-1, the longer dwell has the impact of increasing the time to failure by up to two times (Figure 3.5). Similarly the shallower gradient of the 60 s dwell curve suggests that longer dwell specimens take a relatively greater time to fail at lower stresses. However due to the length of 60 s dwell tests, testing with lower stresses achieved a runout defined as over 200 h of testing.

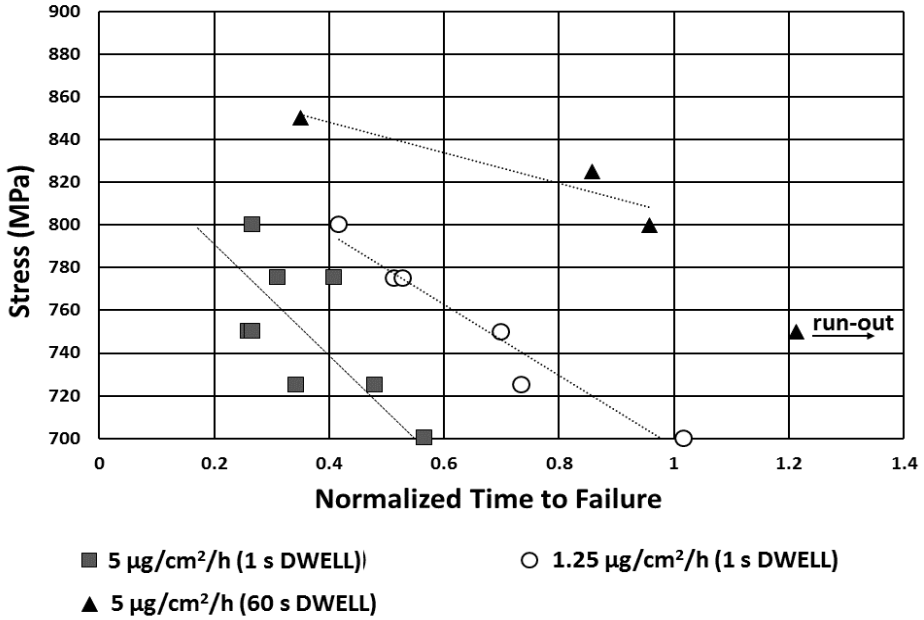

Figure 3.5: Normalised time to failure

3.3.2. Fractographic analysis

Optical images of fracture faces on 60 s dwell samples show multiple {100} crack initiations and subsequent propagation in the form of semi elliptical thumbnails (figure 3.6). After a period of {100} propagation the cracks transition to {111} propagation. During this rapid {111} mechanical crack growth driven by fatigue cycles, fatigue striations were observed on the fracture face/facets. In relation to the presented analysis, striations were defined as rigged demarcation formed as a result of fatigue crack propagation and generated predominantly on {111} facets on the fracture faces examined. Environmental banding were defined as corrosion/oxidation demarcation generated predominantly on {100} planes on the fracture faces examined.

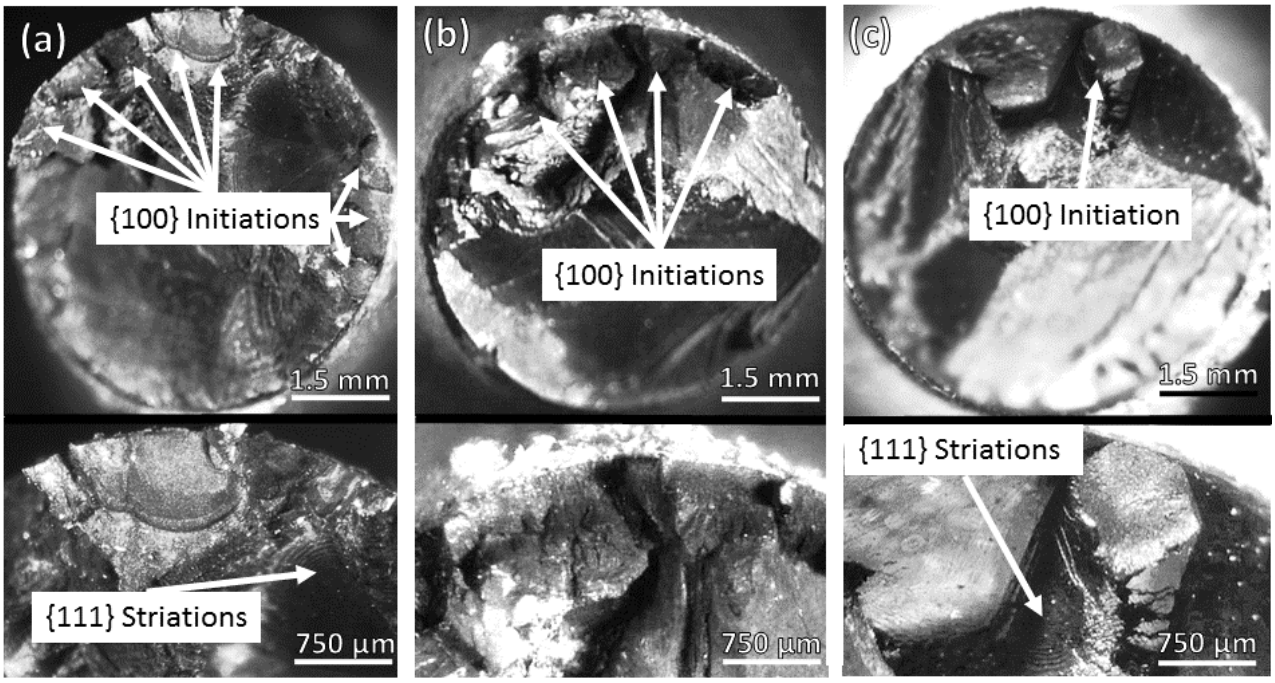

Figure 3.6: Optical microscope images of fracture surfaces **(a)** 800 MPa, 5 µg/cm^2/h deposit flux, 1-60-1-1 **(b)** 850 MPa, 5 µg/cm^2/h, 1-60-1-1 **(c)** 800 MPa, 5 µg/cm^2/h, 1-1-1-1 [13]

Energy dispersive X-ray (EDX) analysis performed on an SEM, of environmental banding on a fracture face (Figure 3.7) is presented in Table 3.2. It can be see that the spectrum locations 1 and 2, taken in the oxide banding contain Ni, O and S, suggesting they are a corrosion product of type II hot corrosion [15][16]. Spectrum location 1 taken in the γ/γ' microstructure contains a comparable wt% of elements as to the substrate alloy CMSX-4, presented in Table 3.1.

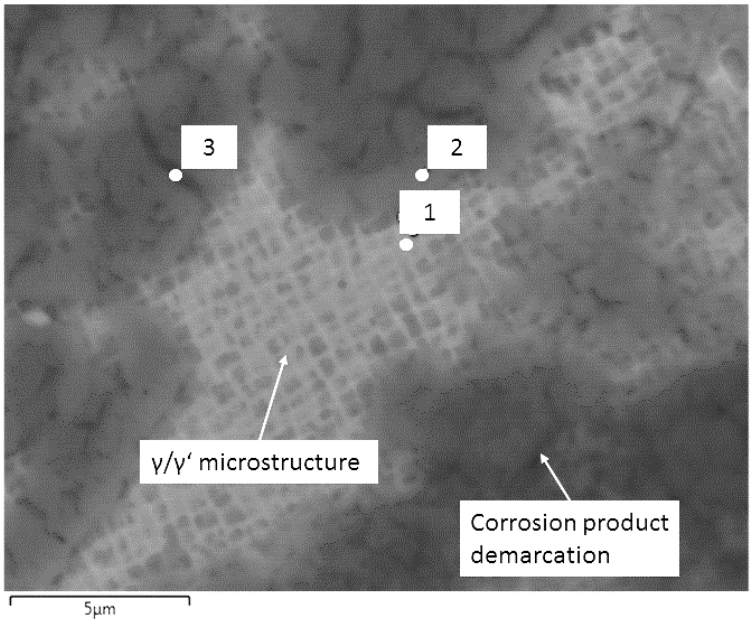

Figure 3.7: Back scattered SEM image of environmental/corrosion banding on a {100} fracture face, EDX spectra were taken in locations 1, 2 and 3 and are presented in table 3.2.

Table 3.2: EDX analysis in wt% from spectrum locations given in Figure 3.7

Spectrum	Ni	Co	Cr	O	W	Al	C	S	Ta
1	52	9	8	9	8	8	0	0	5
2	41	7	4	22	2	3	8	5	0
3	45	9	4	21	3	2	9	5	0

SEM fracture face images of a 750 MPa, 1-1-1-1 loaded specimen are shown in Figure 3.8. Closely spaced environmentally induced oxidation/corrosion banding can be seen on the {100} fracture face. Additionally fatigue striations can be seen on the same sample later in the crack propagation path, these are generated on a {111} fracture face and are most likely produced in the cycles just prior to mechanical overload, when a relatively high ΔK is present at the crack tip. Similar oxidation banding and marking can also be seen on the fracture face of an 800 MPa, 1-1-1-1 loaded specimen presented in Figure 3.9, along with build-up of corrosion product on the fracture surface.

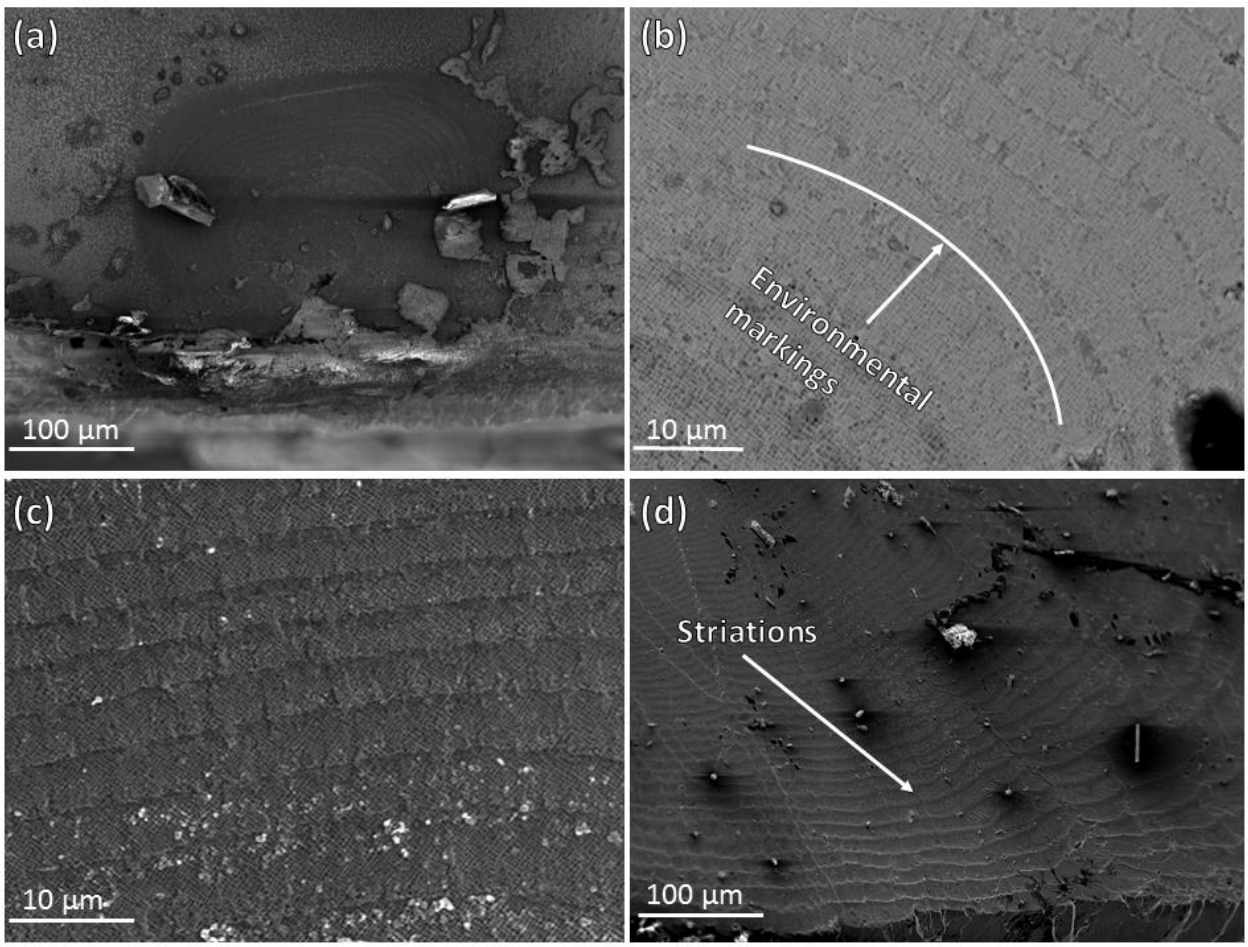

Figure 3.8: Fracture face images of specimen exposed to 750 MPa, 1-1-1-1, 5 µg/cm^2/h deposit flux **(a)** Secondary electron (SE) image of {100} crack initiation and propagation showing environmental oxidation/corrosion banding close to initiation point **(b)** Back scattered electron (BSE) image of environmental oxidation/corrosion banding **(c)** SE image of environmental oxidation/corrosion banding **(d)** SE image of {111} fatigue striations prior to mechanical overload located on {111} facets

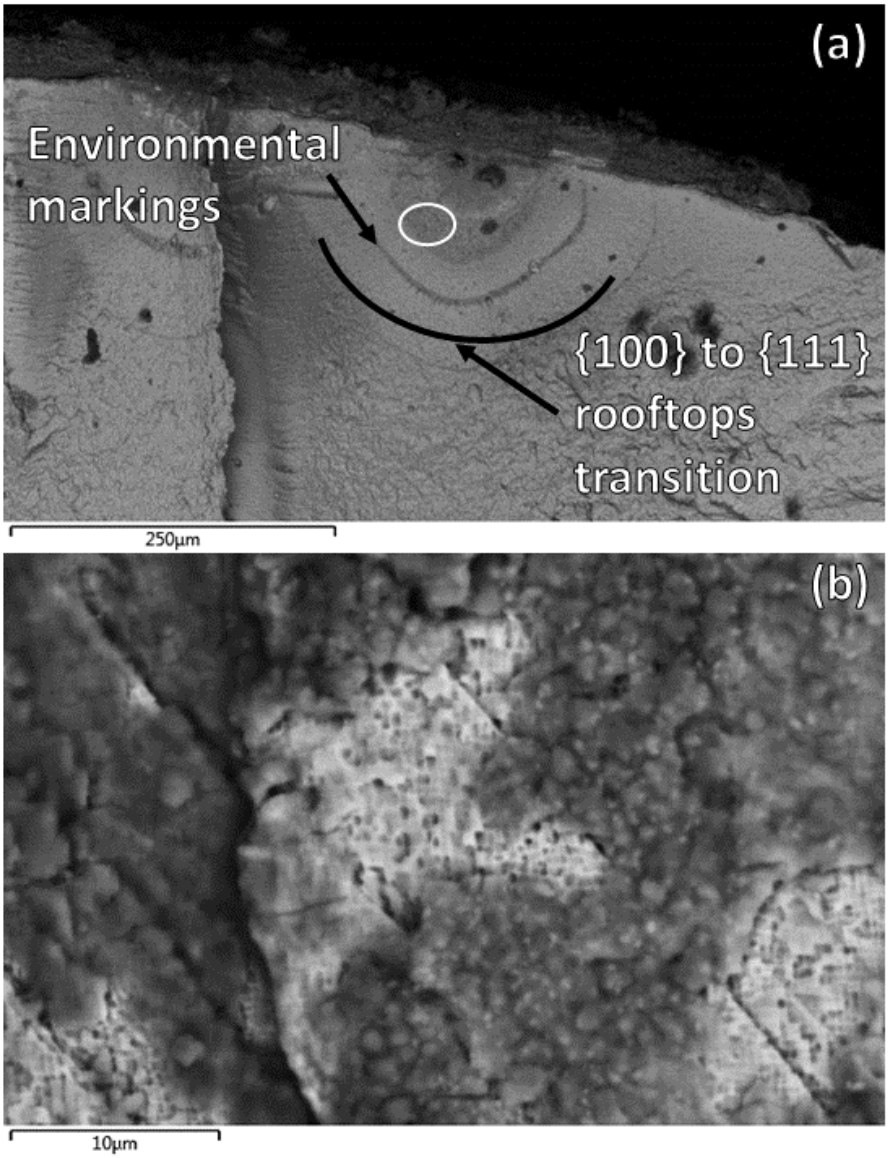

Figure 3.9: BSE, SEM images of an 800 MPa , 5 µg/cm^2/h, 1-1-1-1 specimen **(a)** Fracture face showing transition between {100} and {111} [13] **(b)** Higher magnification of circled location in image (a) showing corrosion product build up on fracture surface

Comparative SEM images of fracture faces from 800 and 850 MPa specimens, with a 1-60-1-1 waveform are given in Figure 3.10 and Figure 3.11. These images demonstrate the initial transitioning from the {100} fracture plane to {111} rooftop peaks as the fatigue threshold is exceeded. Environmental oxide/corrosion banding, and {111} fatigue striations are also visible.

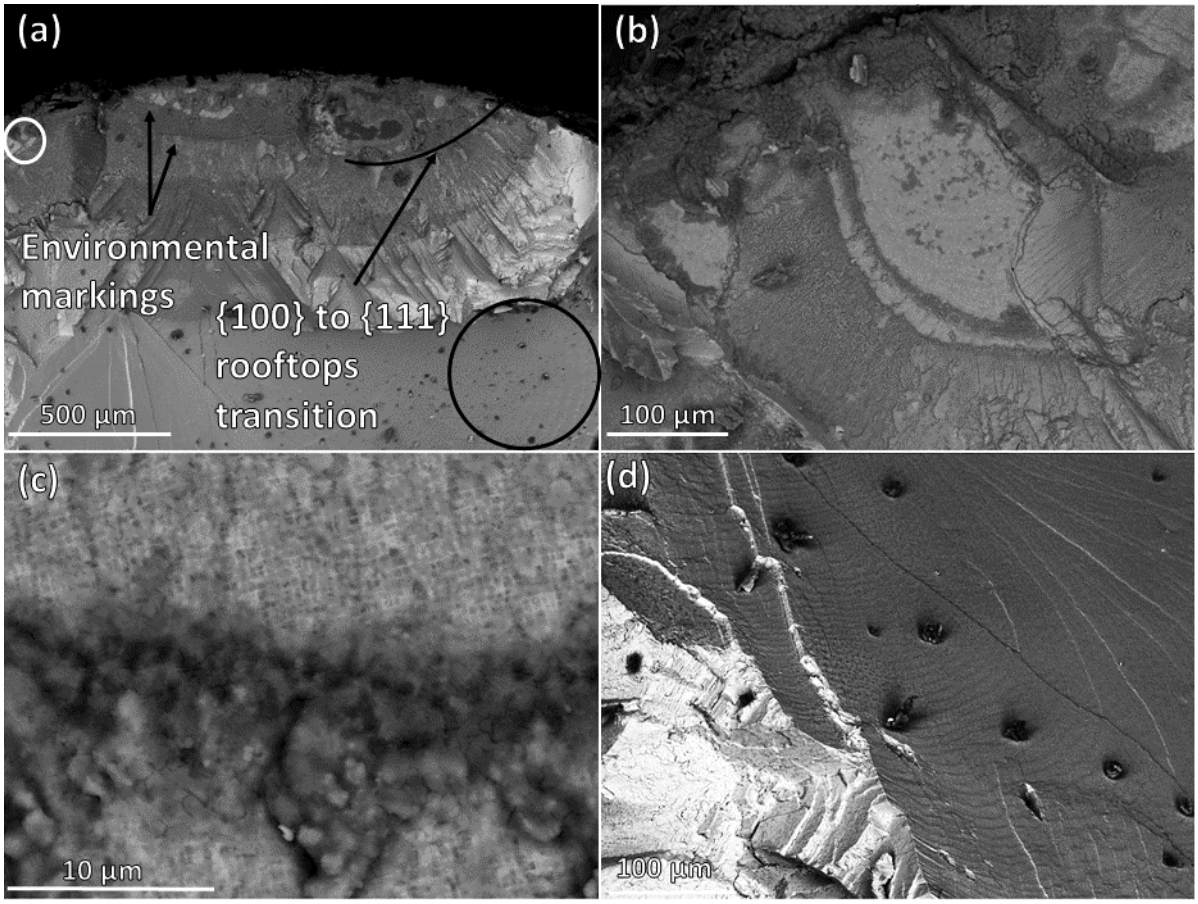

Figure 3.10: SE SEM images of fracture face of specimen exposed to 800 MPa, 1-60-1-1, 5 µg/cm^2/h deposit flux **(a)** environmentally induced oxidation/corrosion markings and {100} to {111} transitioning **(b)** & **(c)** semi-circular oxide banding taken from white circled location in image (a) **(d)** fatigue striations taken from black circled location in image (a)

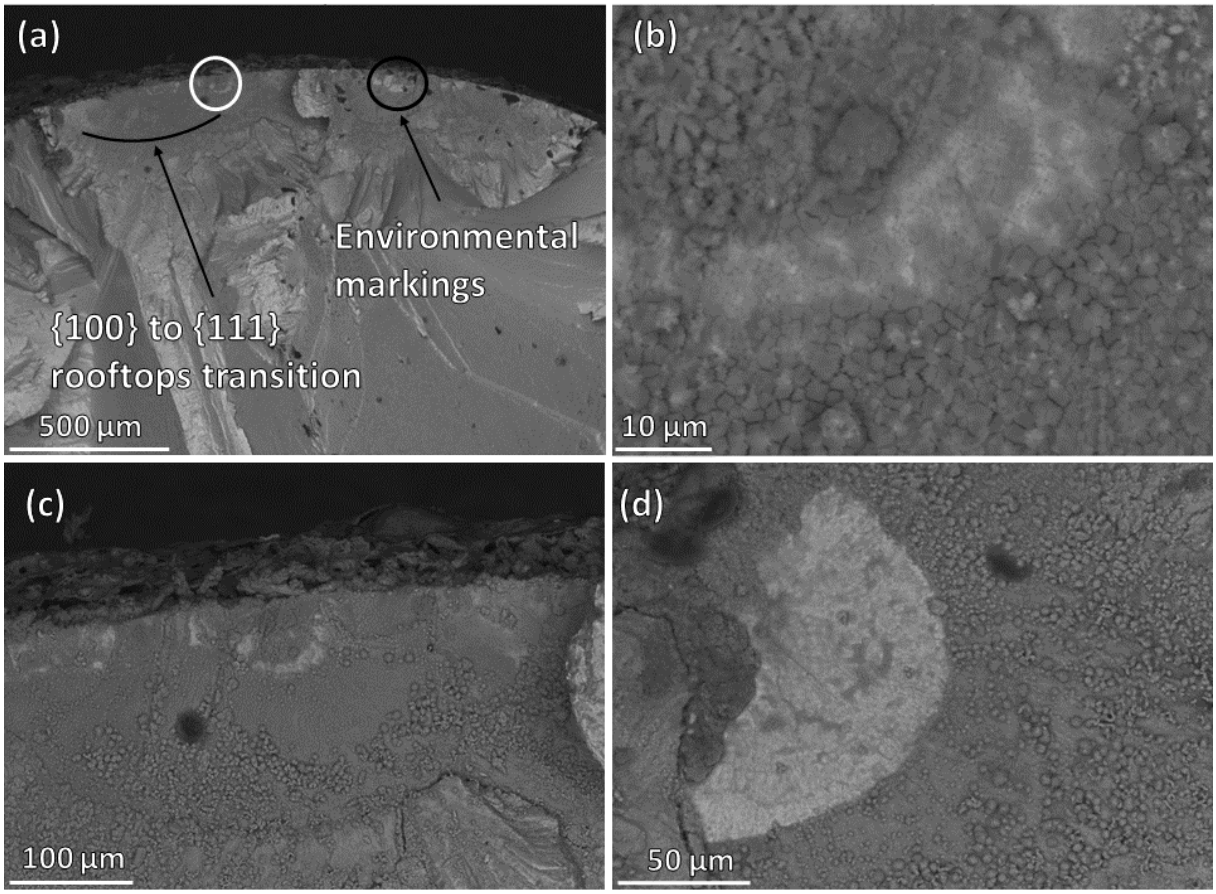

Figure 3.11: SE SEM images of fracture face from a specimen exposed to 850 MPa, 1-60-1-1, 5 µg/cm^2/h deposit flux **(a)** environmentally induced oxidation/corrosion banding and {100} to {111} transitioning **(b)** & **(c)** semi-circular oxide banding taken from white location **(d)** shell shaped feature in the oxide scale taken from the black location

It was noted that the small environmental banding spacing, such as those visible on the 1 s dwell fracture face shown in Figure 3.8 and Figure 3.9, were not clearly visible on 60 s dwell faces (Figure 3.10 and Figure 3.11). It is possible that this banding, generated during fatigue crack initiation, has subsequently been covered up by corrosion product in the 60s dwell test due to the longer durations specimens were exposed to resulting in higher levels of corrosion on the fractured face.

A summary of the number of initiation sites visible over the fracture face area, and of the environmentally induced oxidation/corrosion banding markings are presented in Table 3.3. These values are estimations taken from measurements of optical and SEM images.

Table 3.3: Environmental {001} spacing and fracture face analysis for 5 μg/cm²/h flux

Stress (MPa)	Dwell time (s)	Number of {100} initiations over fracture face	Oxidation banding spacing (μm)	{100} to {111} transition length (μm)
800	60	8	150-180	150-200
850	60	4	185-250	100-150
800	1	1	15-20	150-200

3.4. Discussion

Dwell had a significant impact on reducing the fatigue life when acting in combination with type II hot corrosion. There are several plausible mechanisms as to why dwell has this effect. One is that holding the crack open for prolonged dwell periods allows the corrosive contaminates to diffuse to the crack tip. This results in increased oxidation around the crack tip, enabling the fatigue/cracking mechanism to continue to propagate. A second mechanism is based upon previous research that demonstrated a combined static stress and type II hot corrosion cracking [12][13]. It is therefore plausible that under similar conditions crack propagation can occur during static load dwell periods as well as due to conventional fatigue cycling. This static crack propagation would aid the nucleation and initiation of a fatigue crack. It is also possible however that a combination of enhanced diffusion of corrosive species to the crack tip and static load crack propagation is also occurring and accelerating crack propagation under longer dwell exposures.

It was observed that, whilst dwell reduced the cycles to failure, it took a relatively longer test duration for 60 s dwell specimens to fail. This can also be explained by considering the dwell as accelerating crack initiation and being dependant on exposure time at maximum stress, however when the fatigue threshold is exceeded , the fatigue frequency and ΔK become the dominate factors behind crack propagation. With service conditions generating much longer max stress dwell periods in combination with high cycle fatigue (HCF) and low cycle fatigue (LCF) [28], it is possible that dwell propagation could be the dominate propagation mechanism for crack initiation, and HCF/LCF for fatigue crack propagation until final fracture.

An increased number of {100} crack initiations where observed with the introduction of 60 s dwell and with lower stress dwell tests. It is proposed that there are two contributors for this. Firstly as a result of crack tip oxidation/corrosion resulting in crack tip blunting and enhanced crack initiations [29], and secondly as a result of the static stress crack propagation associated with fatigue crack initiation, being partly independent of stress concentration/intensity.

It can be theorised from fracture face analysis that the combined type II hot corrosion fatigue cracking mechanism exhibits a stop/start behaviour during crack initiation both with 1 and 60 s dwell. This generates the environmental oxidation/corrosion banding. It is postulated that

this results from a time dependant embrittlement mechanism at the crack tip causing crack arresting or abrupt changes in the propagation rate.

Measuring the spacing between environmental oxidation/corrosion banding demonstrates that the spacing can be significantly different between 1 s dwell and 60 s dwell waveform. Additionally the banding looks visibly different, with 1 s dwell leaving light surface discolorations in the γ/γ' microstructure, whereas 60 s dwell leaves a thick scale banding on top of the γ/γ' microstructure. This difference in resultant fracture face could be due to the early environmental banding being masked by corrosion scale on the longer 60 s dwell tests. Additionally it could be due to the dominance of static stress corrosion cracking generating larger beach mark type banding such as those seen in static stress testing [12].

The shell shaped and semi-circular markings observed in the scale on the 60 s dwell fracture faces have contours which match those of the environmental oxidation markings. And are therefore likely to be associated with crack arresting or abrupt changes in the propagation rate.

Changes in the fracture face morphology can in part be associated with the crack transitioning from stage 1 sub fatigue threshold crack initiation, to stage 2 Paris crack growth occurring above the fatigue threshold. Previously conducted finite element (FE) modelling [13] analysing the crack length at which the K_{TH} is exceeded, suggests that it is overcome at a length of around 114 µm for a plain specimen geometry loaded at 800 MPa uniaxial. This is of a similar magnitude to the measured values for {100} to {111} rooftop transition presented in Table 3.2, supporting this theory.

It is proposed that this transition in fracture face morphology is due to stage 1 crack initiation being associated to the time dependant, static-load driven crack growth. This accelerated stage 1 initiation has been observed to take the form of {100} crystallographic propagation, due to preferential γ' corrosion attack at the crack tip [13]. However when stage 2 propagation is reached, propagation results from fatigue driven shear slip contributions in the crystallographic octahedral <111> directions.

3.5. Paper 2 conclusions

- The introduction of a 60 s dwell period reduced the fatigue life of single crystal superalloy CMSX-4 when acting in combination with type II hot corrosion. Considering previous research into static stress cracking combined with type II corrosion, it was suggested that cracks could additionally propagate during the dwell period most notably aiding fatigue crack nucleation and initiation. Fatigue cracks demonstrated consistent surface initiation when exposed to a type II hot corrosion environment.

- It was found that 60 s dwell tests required a relatively longer test duration to fail than comparative 1 s dwell tests. It was proposed that this was due to dwell enhancing the fatigue crack nucleation and initiation, however when cracks exceeded the fatigue

threshold K_{TH} and entered stage 2 propagation, loading frequency and ΔK were the critical drivers determining crack propagation rates.

- The introduction of a 60 s dwell had the effect of increasing the number of {100} crack initiations particularly at lower stresses. This is proposed to be due to crack tip blunting due to oxidation and static stress cracking being less sensitive to stress intensity/concentration.

- Analysis of fracture faces suggests that the crack propagation mechanism propagates in a start/stop fashion. This maybe a result of a time-dependant corrosion embrittlement or crack tip oxidation.

- A correlation in the transition of fracture morphology from {100} to {111} rooftops with the K_{TH} being exceeded was observed. This suggests corrosion has an influence in the crack propagation plane.

- Further research to confirm the nature of crack growth and determine crack growth rates under type II corrosion fatigue conditions is needed in order to account for its effects when designing GT components.

Acknowledgements

The authors acknowledge the support of the Engineering and Physical Research Council (EPSRC) for their support for the project - Flexible and Efficient Power Plant: Flex-E-Plant (Grant number: EP/K021095/1). They also thank the following partners for their the valuable contributions: GE Energy, Doosan Babcock Limited, Centrica plc., EDF Energy (West Burton Power) Limited., Uniper Technologies Limited, Goodwin Steel Castings Limited, NPL Management Limited, R-MC Power Recovery Limited., RWE Generation UK plc., Scottish and Southern Energy (SSE) plc., Siemens Industrial Turbomachinery, and TWI Limited.

Data underlying this paper can be accessed at https://doi.org/10.17862/cranfield.rd.6845411

3.6. Paper 2 references

[1] UK Department of Energy and Climate Change, "Updated energy and emissions projections 2013," *Energy White Pap.*, vol. 947, no. November, pp. 1–51, 2008.

[2] UNFCCC, "Paris Agreement," *Conf. Parties its twenty-first Sess.*, no. December, p. 32, 2015.

[3] P. E. Sikorska, "The need for legal regulation of global emissions from the aviation industry in the context of emerging aerospace vehicles," *Int. Comp. Jurisprud.*, vol. 1, no. 2, pp. 133–142, 2015.

[4] B. W. Lagow, "Materials Selection in Gas Turbine Engine Design and the Role of Low Thermal Expansion Materials," *Jom*, vol. 68, no. 11, pp. 2770–2775, 2016.

[5] P. Caron and T. Khan, "Evolution of Ni-based superalloys for single crystal gas turbine blade applications," *Aerosp. Sci. Technol.*, vol. 3, no. 8, pp. 513–523, 1999.

[6] V. Sass, U. Glatzel, and M. Feller-Kniepmeier, "Anisotropic creep properties of the nickel-base superalloy CMSX-4," *Acta Mater.*, vol. 44, no. 5, pp. 1967–1977, 1996.

[7] J. J. Moverare, S. Johansson, and R. C. Reed, "Deformation and damage mechanisms during thermal-mechanical fatigue of a single-crystal superalloy," *Acta Mater.*, vol. 57, no. 7, pp. 2266–2276, 2009.

[8] H. L. Cockings, K. M. Perkins, and M. Dowd, "Influence of environmental factors on the corrosion-fatigue response of a nickel-based superalloy," *Mater. Sci. Technol. (United Kingdom)*, vol. 33, no. 9, pp. 1048–1055, 2017.

[9] R. Dewangan, J. Patel, J. Dubey, P. K. Sen, and S. Kumar Bohidar, "Gas Turbines Blades—a Critical Review of Failure on First and Second Stages," *Int. J. Mech. Eng. Rob. Res.*, vol. 4, no. 1, 2015.

[10] G. S. Mahobia *et al.*, "Effect of hot corrosion on low cycle fatigue behavior of superalloy IN718," *Int. J. Fatigue*, vol. 59, pp. 272–281, 2014.

[11] H. Rosier, K. Perkins, A. Girling, J. Leggett, and G. Gibson, "Factors affecting the corrosion fatigue life in nickel based superalloys for disc applications," *MATEC Web Conf.*, vol. 14, p. 03001, 2014.

[12] L. Brooking, J. Sumner, S. Gray, and N. J. Simms, "Stress corrosion of Ni-based superalloys," *Mater. High Temp.*, vol. 35, no. December, pp. 120–129, 2017.

[13] L. Brooking, J. Sumner, S. Gray, J. R. Nicholls, G. Marchant, and N. J. Simms, "Effect of Stress State and Simultaneous Hot Corrosion on the Crack Propagation and Fatigue Life of Single Crystal Superalloy CMSX-4," *Int. J. Fatigue*, 2018.

[14] D. A. Shifler, "Hot corrosion: a modification of reactants causing degradation," *Mater. High Temp.*, vol. 35, no. 1–3, pp. 225–235, 2018.

[15] N. Eliaz, G. Shemesh, and R. M. Latanision, "Hot corrosion in gas turbine components," *Eng. Fail. Anal.*, vol. 9, no. 1, pp. 31–43, 2002.

[16] J. Sumner, A. Encinas-Oropesa, N. J. Simms, and J. R. Nicholls, “Type II hot corrosion: Kinetics studies of CMSX-4,” *Oxid. Met.*, vol. 80, no. 5–6, pp. 553–563, 2013.

[17] G. J. Santoro, S. A. Gokoglu, F. J. Kohl, C. A. Stearns, and D. A. Rosner, “Deposition of Na2SO4 From Salt-Seeded Combustion Gases of a High Velocity Burner Rig,” *AIME, Metall. Soc*, pp. 417–434, 1984.

[18] F. Birello, D. Borello, P. Venturini, and F. Rispoli, “Modelling of Deposit Mechanisms Around the Stator of a Gas Turbine,” *Vol. 2 Aircr. Engine; Coal, Biomass Altern. Fuels; Cycle Innov.*, vol. 2, no. May 2016, p. V002T03A019, 2013.

[19] J. Tomeczek, H. Palugniok, and J. O. Ochman, “Modelling of deposits formation on heating tubes in pulverized coal boilers,” *Fuel*, vol. 83, no. 2, pp. 213–221, 2004.

[20] B. Rengara, S. Baba, and M. Okazaki, “Influence of Crystal Orientation on Cyclic Sliding Friction and Fretting Fatigue Behavior of Single Crystal Ni-Base Superalloys,” in *Superalloys 2016: Proceedings of the 13th International Symposium on Superalloys*, 2016, pp. 395–404.

[21] V. Sass, U. Glatzel, and M. Feller-Kniepmeier, “Creep anisotropy in the monocrystalline nickel-base superalloy CMSX-4,” *Superalloys 1996 8th Int. Symp. Superalloys.*, pp. 283–290, 1996.

[22] N. E. Dowling, *Mechanical Behavior of Materials*, 4th ed. Boston, MA : Pearson, 2012.

[23] M. R. Joyce, X. Wu, and P. a S. Reed, “The effect of environment and orientation on fatigue crack growth behaviour of CMSX-4 nickel base single crystal at 650 °C,” *Mater. Lett.*, vol. 58, no. 1–2, pp. 99–103, 2004.

[24] N. Pugno, M. Ciavarella, P. Cornetti, and A. Carpinteri, “A generalized Paris’ law for fatigue crack growth,” *J. Mech. Phys. Solids*, vol. 54, no. 7, pp. 1333–1349, 2006.

[25] T. L. Anderson, *Fracture Mechanics: Fundamentals and Applications*, vol. 58, no. 1. 2012.

[26] R. Pippan, “Dislocation Emission a N D Fatigue Crack Growth Threshold,” vol. 39, no. 3, pp. 255–262, 1990.

[27] “Image-J.” Oxford Instruments, 2017.

[28] Y. G. Li and P. Nilkitsaranont, “Gas turbine performance prognostic for condition-based maintenance,” *Appl. Energy*, vol. 86, no. 10, pp. 2152–2161, 2009.

[29] S. X. Mao and A. G. Evans, “the Influence of Blunting on Crack Growth Oxide / Metal Interfaces,” *Acta Metall.*, vol. 45, no. 10, pp. 4263–4270, 1997.

4. Paper 3: Effect of stress state and simultaneous hot corrosion on the crack propagation and fatigue life of single crystal superalloy CMSX-4

L.Brooking[1*], S.Gray[1], J.Sumner[1], J.R.Nicholls[1], G.Marchant[2], N.J.Simms[1]

[1] Cranfield University, College Rd, Cranfield, MK43 OAL

[2] Siemens Industrial Turbomachinery, 1 Waterside S, Lincoln, LN5 7FD

*Corresponding author: l.b.brooking@cranfield.ac.uk

Abstract. Operating conditions within industrial gas turbines are changing in response to pressures to reduce environmental impact and enable use of renewable sources. This is driving an increase in the operational temperatures and pressures of combustion in turbine systems. Additionally, diverse operating environments can result in higher sulphur and trace metal contaminant levels, exacerbating hot corrosion in GT systems. Low cycle fatigue (LCF) cycling can also be intensified as a result of increased start/stop shutdowns. The combined effects of hot corrosion and stress are experimentally studied on CMSX-4 single crystal (SC) γ/γ' system under both fatigue and static stress conditions, with either a multi-axial bending or uniaxial stress state. The associated stress intensity thresholds (K_{TH}) under the various stress conditions were evaluated using finite element analysis (FEA). Cracking was observed both under static and fatigue stress conditions in a hot corrosion environment. Crack morphologies were analysed using SEM techniques. Bending stresses and fatigue cycles demonstrated increased crack propagation in the presence of hot corrosion with static uniaxial stresses showing the longest nucleation times and lowest propagation rates.

Keywords: Hot Corrosion, Fracture Mechanics, FEA, Single Crystal Superalloys

Nomenclature and Units

K – Stress intensity (Pa·m$^{1/2}$)

K_{TH} – Fatigue stress intensity threshold

K_{cr} – Critical stress intensity threshold

K_I – Mode I Stress intensity

σ – Stress (Pa)

Y – Linear elastic fracture mechanics geometry factor

C – Paris law constant

n – Paris law exponent

J – J-integral (J/m^2)

x, y, z – Cartesian coordinates

v – Poisson's ratio

E – Young's modulus (Pa)

σ_G – Stress gradient parameter (Pa/m)

σ_A – Specimen surface stress at location *A* (Pa)

σ_B – Specimen surface stress at location *B* directly opposite *A* (Pa)

t_{AB} – Specimen thickness from *A*-*B* (m)

4.1. Introduction

Developments to improve the operational efficiencies of gas turbines (GT) in recent times have led to increases in the operational temperatures of turbine blade components. Type II hot corrosion is caused by the formation of an $Na_2SO_4/CoSO_4$ eutectic on the surface, resulting in pitting type attack [1]. Whilst turbines are designed to operate outside of the corrosion temperature ranges, it is thought that type II hot corrosion can be assisted by local stress and strain. As such, cracking and degradation mechanisms not accounted for by current design life models [2][3] have been observed in regions such as the under-platform area. It is proposed that this is due to such locations being subject to simultaneous high stresses and corrosive conditions, resulting in a hot corrosion assisted fracture and/or fatigue mechanism.

The superalloy CMSX-4 is an example of a 1st stage turbine blade alloy with a single crystal γ/γ' system. CMSX-4 has favourable high temperature creep and rupture properties combined with good production affordability when compared with other single crystal (SC) superalloys [4]. However its lower Cr content compromises its corrosion resistance. As such CMSX-4 is susceptible to hot corrosion at temperatures below type II reported at 680 °C – 800 °C [5][6]. It has been reported that type II hot corrosion can occur at temperatures as low as 575 °C [7]. The impact of static stress assisted hot corrosion on CMSX-4 was studied in previous work and was found to occur at a temperature of 550 °C [8], also supported by [2]. It was demonstrated in this work [8], that a type II mechanism can occur at these lower temperatures when assisted by stress. Additionally a switch in the corrosion mechanism from attack of the γ at locations towards the specimen surface to attack of the γ' at the stress assisted crack tip was observed.

It was further observed that cracks appear to then subsequently interact with and split γ' precipitates. Resulting in propagation along {100} planes perpendicular to the specimen surface. Without the presence of hot corrosion, cracks in a uniaxial stress state propagate and fracture along slip bands of the {111} family [9][10][11] in SC superalloys such as CMSX-4 at

temperatures up to 850 °C. In complex multi axial stress states for low ΔK levels cracks propagate along macroscopic {100} or {110} planes due to opposing slip contributions from the {111} slip systems, at higher ΔK levels they propagate along {111} systems [12].

A detrimental effect of hot corrosion on the fatigue life of superalloys has been observed in previous research [2][13][14][15][16]. It can also be concluded from these works that the longer the duration of the fatigue testing, the greater the relative effect of hot corrosion on reducing fatigue life. However the effects of multi-axial stress states and static stress gradients on crack propagation in superalloys, combined with hot corrosion fatigue, is not well studied. A study into the effects of stress state on the fatigue crack growth in polycrystalline Inconel 718 exposed to an oxidising environment, found that with increased oxidation cracks became less influenced by stress intensity (ΔK) and more by stress state [17]. With many superalloys such as CMSX-4 demonstrating anisotropic behaviour [11][9], and the under-platform region of GT blades being under a multiaxial bending stress [18], it is important to develop an understanding of the materials behaviour under these combined conditions.

Finite element analysis (FEA) uses computational solvers to solve a chain of simultaneous equations in order to calculate the local stresses within a defined geometry mesh subjected to boundary conditions. FEA combined with linear elastic fracture mechanics (LEFM) provides a capable tool to assess crack stability and propagation for fatigue that follows Paris' law behaviour [19].

This paper proposes a combined mechanism for fracture under type II hot corrosion conditions, the mechanism is based upon the following fracture principles. Firstly under static load conditions the local stress intensity (K_I) has to overcome the critical stress threshold of the material (K_{cr}), resulting in the complete fracture of a brittle body or a body under plane strain conditions. Secondly Paris-law fatigue propagation occurs as a result of the change in stress intensity (ΔK) which exceeds the fatigue threshold (K_{TH}). The proposed mechanism works on the observation that hot corrosion had the impact of locally lowering both the K_{cr} critical fracture threshold and the fatigue threshold K_{th} at the crack tip. Therefore blades subject to hot corrosion conditions in highly stressed regions can undergo localised fracture due to a combination of static stress-hot corrosion cracking and accelerated Paris fatigue cracking, resulting in accelerated combined crack propagation similar to the SCC mechanism proposed by [20]. Additionally stop start type environmental fatigue models have been proposed, these mechanisms are based on the time dependant nature of species diffusing ahead of the crack tip causing embrittlement [21].

4.2. Experimental

4.2.1. Material

The single crystal superalloy CMSX-4 (Table 4.1) was used to produce all the samples for this paper. The samples were machined from directionally solidified bars such that the orientations given in Figure 4.1 were controlled for specific specimen geometries. Literature suggests that the fatigue stress intensity threshold for CMSX-4 in air is around 15 MPa·$m^{1/2}$ [12]. The critical stress intensity threshold is given in air at 650 ^{o}C as 60 MPa·$m^{1/2}$ [22].

Table 4.1 : Composition of CMSX-4 (wt%)

Alloy	Cr	W	Co	Mo	Al	Ti	Ta	Re	Hf	Ni
CMSX-4	6.5	6.0	9.6	0.6	5.6	1.0	6.5	3.0	0.1	Bal.

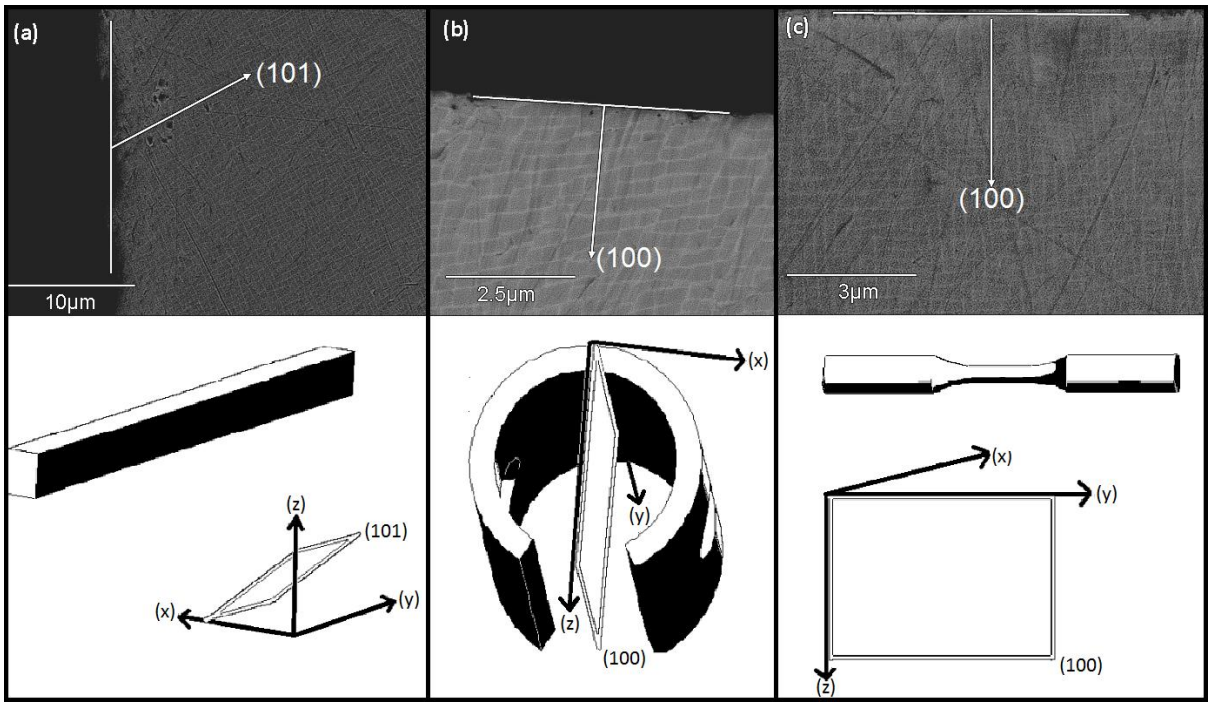

Figure 4.1: Microstructure orientation determined from backscatter SEM images showing γ/γ' orientation in relation to specimen surface. The crystallographic orientation is illustrated/defined within the geometry axis below the relevant SEM image, **(a)** Three point bend 30°- 45° (201)-(101), **(b)** C-ring 90° (100), **(c)** Plain specimen 90° (100)

4.2.2. Experimental methodologies

The corrosive deposit flux used for experimental testing was maintained through a deposit recoat methodology, where recoats were applied every 100 h. The salt used was an 80/20 mol% mix of Na_2SO_4 - K_2SO_4 and all tests were conducted at 550 °C with a test gas of 300 ppm SO_2 and air. The sulphate salt deposit and test gas was used in order to simulate sulphidation or low temperature hot corrosion as seen in a GTs. Testing systematically varied the stress state and deposit flux. A balance accurate to 0.01 mg was used to measure the salt quantities deposited.

Three geometries were used for static testing: C-rings, 3-point bend specimens and plain geometry fatigue specimens (Figure 4.2). This was in order to achieve three different stress states: multi-axial high stress gradient, multi-axial high von Mises and uniaxial uniform tensile stress state.

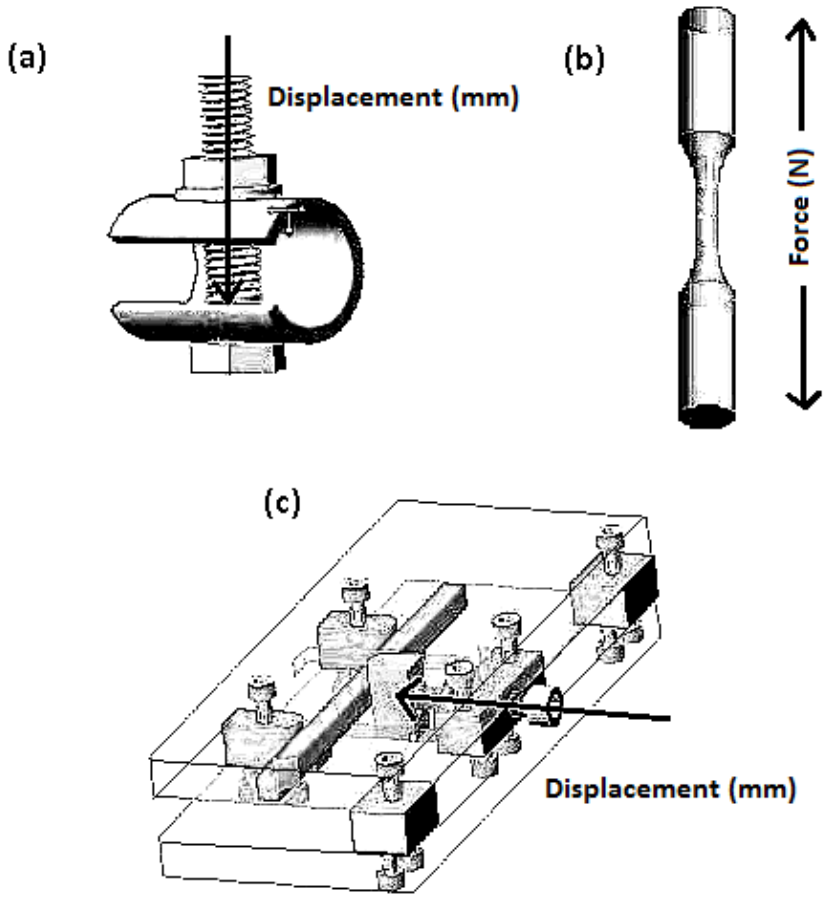

Figure 4.2: Specimen geometry loadings shown through illustration, **(a)** C-ring strain control, **(b)** Plain specimen load control, **(c)** 3-point bend strain control

Target stresses for C-rings and three point bend specimens were achieved by tensioning to calculated displacements using equations from standards [23] & [24] respectively. Statically loaded specimens were checked for cracking using an optical microscope every 100 h. If no cracking was detected using an optical microscope then specimens were re-salted checked for relaxation and further exposed in 100 h intervals.

Additional statically stressed C-ring tests were run, where tests were systematically terminated at 100,300 and 500 hours in order to assess crack damage and propagation as a function of time and stress. This was achieved through measuring the {100} corrosion driven crack planes and crack initiation points.

Fatigue specimens were tested until failure, testing was conducted using a load-controlled fatigue rig equipped with induction heating. The induction system heated a sheath around

the fatigue specimens in order to maintain a more consistent temperature across the specimen. Cycles to failure (S-N) graphs were produced for a range of tensile stresses where R=0 using a trapezoidal wave form. Samples were exposed for 500 h of pre-corrosion prior to fatigue testing, this was done with one of two set pre corrosion fluxes of 1.25 µg/cm^2/h or 5 µg/cm^2/h representative of a lower and higher under platform deposit flux.

4.3. Analytical methodologies

Optical microscopy and field electron gun (FEG) SEM imaging techniques were used to study and characterise samples post exposure. Image-J [25] image processing software was used to take measurements from images, such as crack size and depth, and AZtec [26] was used to process EDX data.

FEG SEM microscopy was conducted on both Phillips FEI XL-30 and JEOL 7800F systems. Specimen surfaces, and fracture surfaces were analysed before being prepared by mounting in a 50:50 mixture of epoxy resin and ballotoni (40-70 µm diameter glass beads). They were then cross sectioned, ground and polished in oil to preserve corrosion products, enabling crack tip and microstructure analysis.

Crack size measurements were spilt into three parameters, crack depth was defined as the [100] propagation depth into the specimen. Crack width was measured as the total width of all joined thumbnail cracks on the {100} plane if multiple initiations were visible on the fracture face. The crack rate of initiation and propagation for static stress conditions was calculated as the average [100] crack depth over the total test duration. The {100} area was calculated as half of an ellipse making an individual thumbnail fracture, these were added where multiple {100} fractures were visible.

FEA was conducted using ANSYS R15 [27] and ABAQUS [28]. An idealised isotropic material model was used for the <001> direction, this was derived from published data [9]. 3D models were used to assess the axial directions and magnitudes of the stresses within the three geometries. Additionally the J-integral energies were calculated for cracks propagating in the [100] crystallographic direction using 2D models. Boundary conditions for FEA modelling were set up to represent the experimental parameters where strain control was represented by a displacement boundary condition and load control by a load boundary condition. In order to quantify the stress gradient present in the geometries, a macro stress gradient parameter is proposed (Equation 4.1.).

Equation 4.1*:* Stress gradient parameter

$$\sigma_G = (\sigma_A - \sigma_B)/t_{AB}$$

4.4. Theory/calculation

The general LEFM (Equation 4.2) was used as a model to assess crack stability and growth and determine threshold crack lengths. LEFM assess crack stability as a function of the macroscopic elastic stress field (σ) crack length (a) and geometry factor (Y).

Equation 4.2: Linear elastic fracture mechanics equation [29]

$$K = \sigma Y \sqrt{a\pi}$$

The Paris law (Equation 4.3) is then commonly used to model crack propagation da/dN as a function of the change in stress intensity (ΔK), constant (C) and an exponent (n).

Equation 4.3: Paris law crack growth equation [29]

$$\frac{\partial a}{\partial N} = C(\Delta K)^n$$

4.5. Results and discussion

4.5.1. Static stress results and discussion

In the C-ring geometry modelling predicted that the principal compressive stresses are relatively higher than the tensile equivalents. This can be explained by the smaller inner circumference producing a larger compressive strain and resultant stress than the relatively larger outer circumference in tension. Similarly modelling predicted higher compressive stresses in the three point bend specimen relative to the tensile equivalents. However these results are associated to the additional contact force of the three point bend roller at the point of maximum compressive deflection.

Table 4.2 presents a summary of the predicted maximum principal stress, the stress gradient parameter and von Mises surface stresses present in the three geometries. This is given as a function of the target stress which was the stress used to calculate the displacement required from the relevant standard. These stress components were calculated using FEA, the specimen loading is defined in Figure 4.2 and an example FE model is presented in Figure 4.3. Comparing the stress conditions of the three geometries presented in Table 4.2, shows that C-rings provide both the highest stress gradient and the highest (mode I) principal crack opening stress, the three point bend geometry however produces the highest localised von Mises stress. In the C-ring geometry modelling predicted that the principal compressive stresses are relatively higher than the tensile equivalents. This can be explained by the smaller inner circumference producing a larger compressive strain and resultant stress than the relatively larger outer circumference in tension. Similarly modelling predicted higher compressive stresses in the three point bend specimen relative to the tensile equivalents.

However these results are associated to the additional contact force of the three point bend roller at the point of maximum compressive deflection.

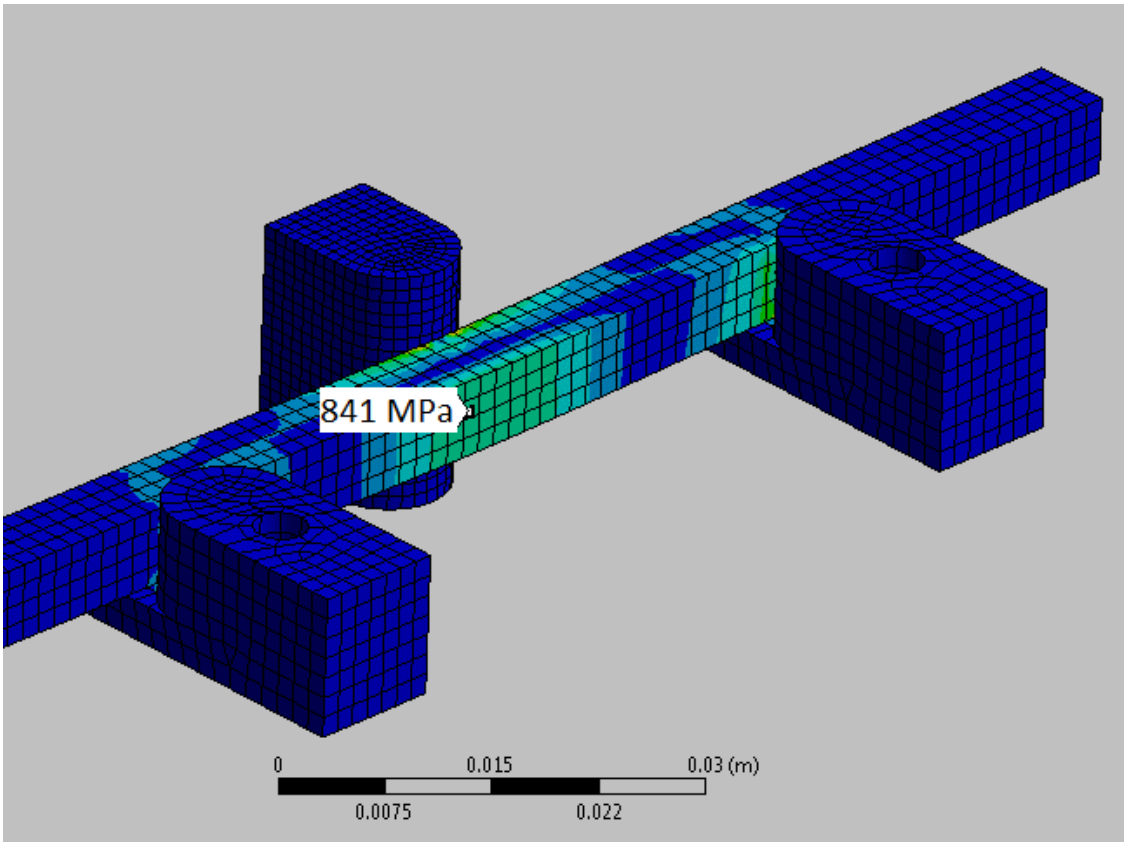

Figure 4.3: FE model of von-Mises stress distribution in three point bend geometry, showing elevated compressive stresses at contact point with roller

Table 4.2 : Stress states present in the three specimen geometries

Geometry	Target Stress (MPa)	Principal (mode 1) Tension (MPa)	Principal (mode 1) Compression (MPa)	Principal Stress Gradient Parameter (σ_G) (MPa/mm)	von Mises Tension (MPa)
Plain Specimen	800	800	0	0	800
C-ring	800	935	-1100	127.19	820
Three Point Bend	800	880	-980	31	849

The static stress hot corrosion results presented in Table 4.3 suggest a time dependant cracking mechanism. Stress induced hot corrosion cracks generated in these static stress environments all followed an orthogonal microstructure plane as shown in Figure 4.4. It is hypothesised that this occurs as a result of a localised reduction in K_{cr} (embrittlement) of the γ' at or ahead of the crack tip, with the next closest γ' to be embrittled being orthogonal to the crack tip, as illustrated in Figure 4.5.

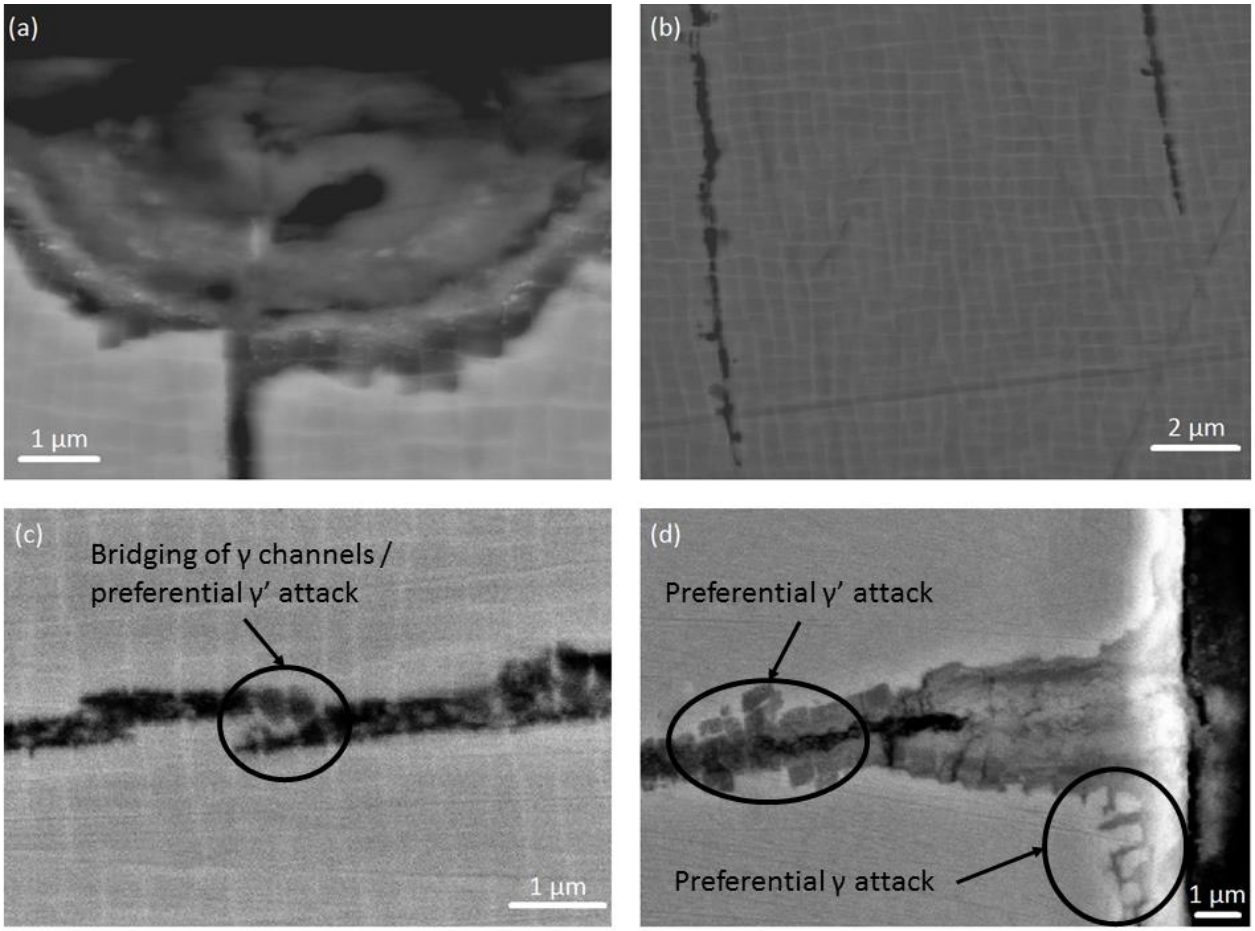

Figure 4.4: SEM micro section images of statically loaded specimens, **(a)** & **(b)** Back scattered SEM images of a three point bend specimen, 800 MPa statically loaded, 200 h, 5 µg/cm^2/h flux, 550 °C, showing a crack initiating from an apparent corrosion pit corroding and propagating through γ' precipitates, **(c)** Secondary SEM images of a C-ring, 800 MPa statically loaded, 100 h, 5 µg/cm^2/h flux, 550 °C, showing preferential γ' attack down the crack with cracks, with cracks propagating through γ' leaving γ channel bridging, **(d)** Back scattered SEM image showing preferential γ attack towards the stress relaxed surface and preferential γ' attack further down the crack

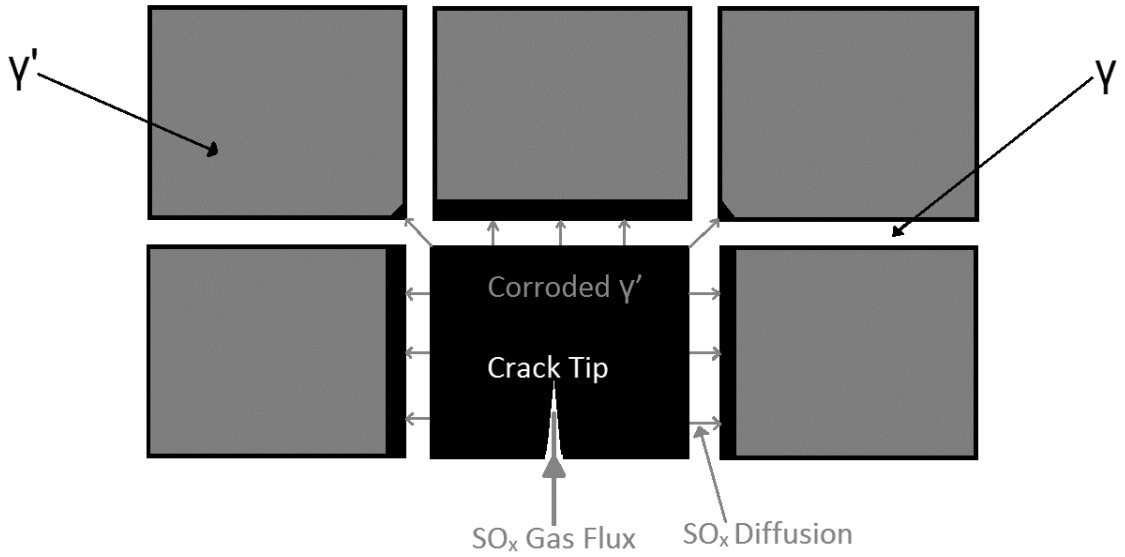

Figure 4.5: Proposed mechanism for gas induced fluxing at the crack tip, showing stress assisted corrosive species diffusion into the γ' and resulting in orthogonal embrittlement and thus crack propagation.

The results demonstrate that C-rings induce the most aggressive stress state for static stress-hot corrosion as they produced optically visible cracking after the shortest exposure times. The second most aggressive stress state tested was the three point bend specimen with this specimen showing cracking 100 h after the comparable C-ring specimen. Plain specimens required longer exposure times in order to crack still, cracking a further 100h after the comparable three point bend specimen. These results suggest a trend that the static stress hot corrosion cracking mechanism was exacerbated by the magnitude of the stress gradient induced through bending. The plain specimen tested for 200 h at 800 MPa and a 1.25 $\mu g/cm^2/h$ flux was further cross sectioned and examined under an SEM to look for microscopic crack initiations, however no initiations or cracks could be found on this specimen, implying stress and flux are crucial in order for this mechanism to occur.

Table 4.3 : Static stress, exposure for visible cracking

Geometry	Deposition Flux (μg/cm^2/h)	Stress (MPa)	Time to Crack 100 h intervals (hours)
C-ring	5	800	100
C-ring	5	700	100
C-ring	5	500	200
C-ring	1.25	800	100
C-ring	1.25	700	200
C-ring	1.25	500	300
Plain Specimen	5	800	300
Plain Specimen	1.25	800	No Cracking after 200
Plain Specimen	5	900	200
Three Point bend	5	800	200

Optical image analysis of the (100) thumb nail fracture surfaces on C-rings after set exposures allowed for the calculation of the average static stress crack initiation and propagation rates over the exposure duration, these are presented in Table 4.4.

For C-rings crack propagation rates decrease as cracks propagate through the C-ring section. This is likely due to a couple of reasons: firstly because as the crack propagates the stress gradient at the crack tip reduces; and secondly because of stress relaxation due to the presence of the crack.

In C-rings, static stress cracks form a broad fronted propagation generated from multiple initiations, which results in conjoined thumbnail cracks right across the specimen width. Whereas in statically loaded plain specimens cracks form a similar morphology but propagate and initiate at a slower rate (Figure 4.6). Both optical and SEM analysis of the fracture surfaces of statically loaded specimens show beach type markings on the fracture faces. These are associated to the “stop-start” time dependant nature of hot corrosion stress cracking, however the exact mechanism needs further study to fully explain the changes in growth rate.

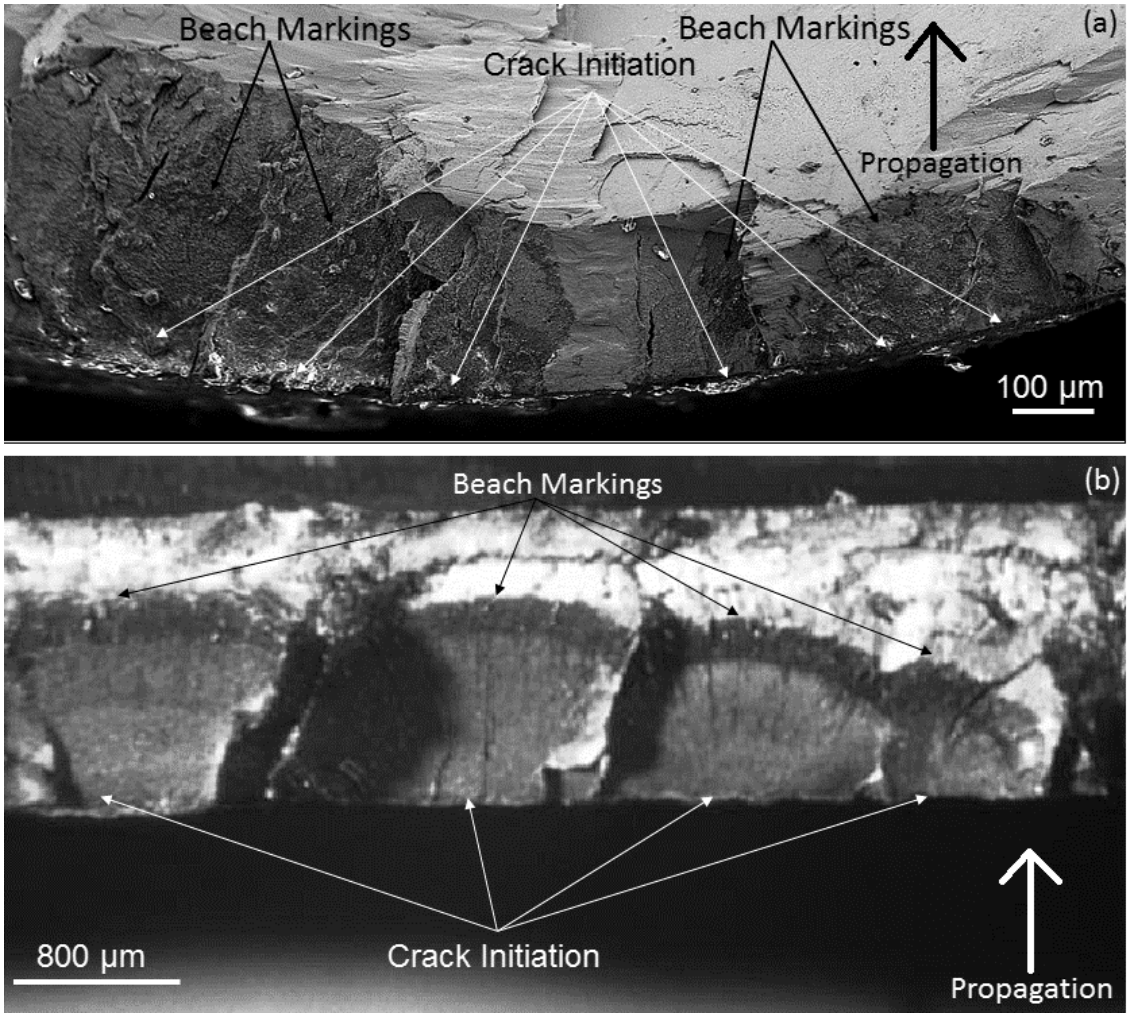

Figure 4.6: Microscope images of statically loaded specimen fracture faces, **(a)** secondary electron SEM image of a 900 MPa, 5 µg/cm^2/h flux, 550 °C, 200 h, statically loaded plain specimen [001] propagation **(b)** optical image of a 500 MPa, 5 µg/cm^2/h flux, 550 °C, 100 h, statically loaded C-ring specimen [001] propagation markings

Table 4.4 : Static stress crack propagation rates of C-rings and plain specimens subject to specific exposure intervals

Geometry	Target Stress (MPa)	Exposure Time (h)	Flux (µg/cm^2/h)	[100] Crack Depth (mm)	AVE da/dt (µm/h)
C-ring	800	100	5	0.46	4.6
C-ring	800	500	5	1.45	2.9
C-ring	700	300	5	0.97	3.2
C-ring	700	500	5	1.35	2.7
Plain Specimen	900	200	5	0.398	1.9
Plain Specimen	800	300	5	0.519	1.73

Under static conditions a conventional form of type II hot corrosion occurred on the specimen surface forming a Co/Ni rich outer oxide scale. In addition an inner Al/Cr rich mixture of oxides and the salts K_2SO_4 and Na_2SO_4 formed. Whilst the temperature of 550 ^oC is considered too low to form the eutectic mixtures required for type II hot corrosion, in a stress assisted system the corrosion mechanism appears to be consistent with type II (Figure 4.7). At the crack tip however, the corrosion mechanism seems to switch and interact with the γ' precipitates. It is hypothesised that this could be due to a change in the fluxing mechanism. As the sulphate salt species are not mobile enough to travel down the crack, it is proposed that the fluxing mechanism at the crack tip occurs through the stress assisted diffusion of SO_x and potentially other corrosive species into the γ' precipitates.

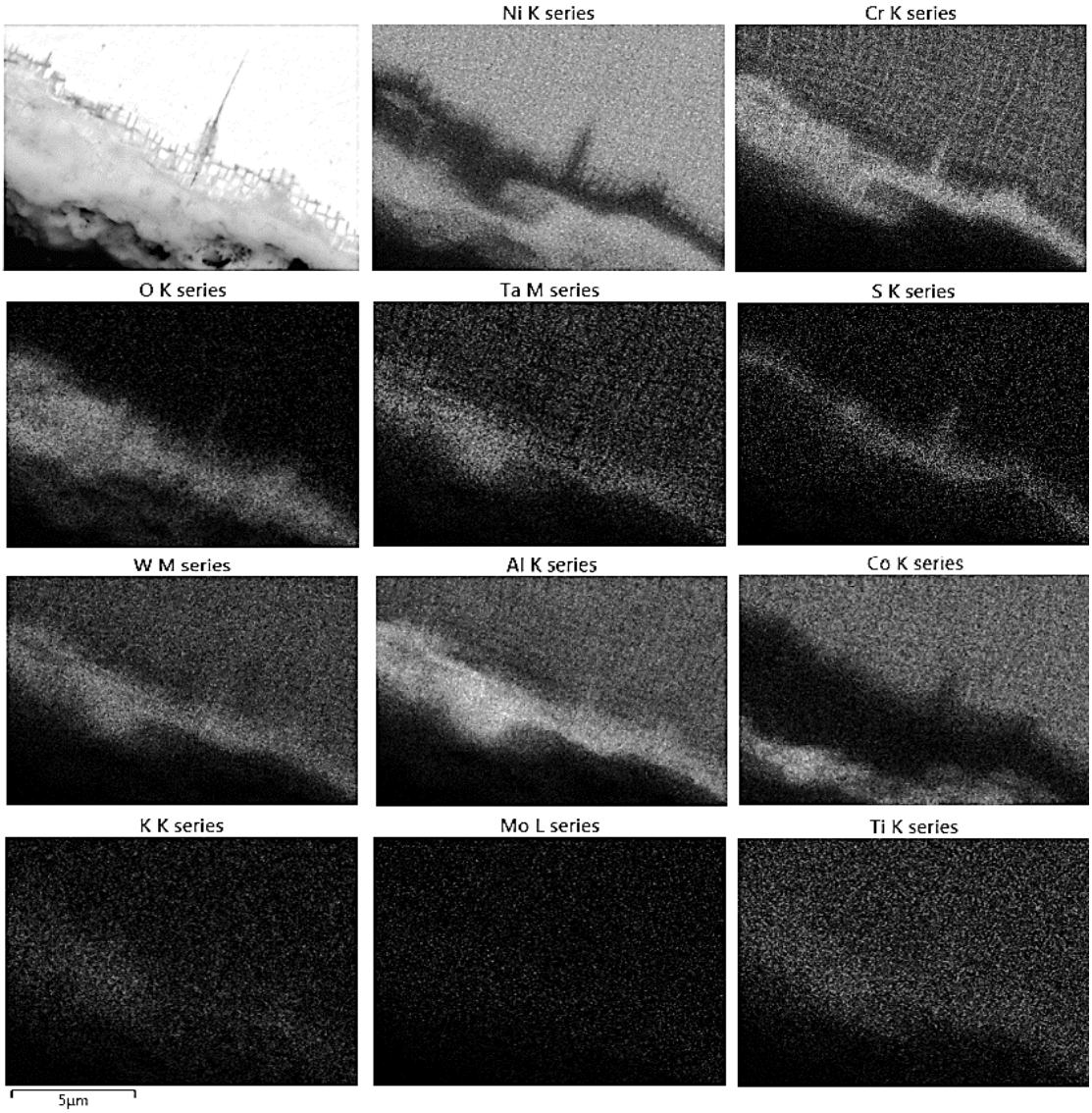

Figure 4.7: C-ring exposed for 300h at 800 MPa, and 5 µg/cm^2/h, shows segregation of elements within the corrosion products forming an outer oxide scale of Ni/Co and an inner Cr/Al rich layer with a sulphur rich band reacting with the substrate. Also visible is some elemental segregation in the γ/γ' microstructure showing the γ being rich in Cr and the γ‘ in Al

4.5.2. Fatigue results and discussion

Two experimental S-N curves are presented in Figure 4.8 for a 1.25 and a 5 µg/cm^2/h deposition flux for CMSX-4 pre corroded for 500 h at 550 ^{o}C. The tabulated experimental results are given in (Table 4.5). Both deposition fluxes fail in fewer cycles than the predicted baseline fatigue data in air.

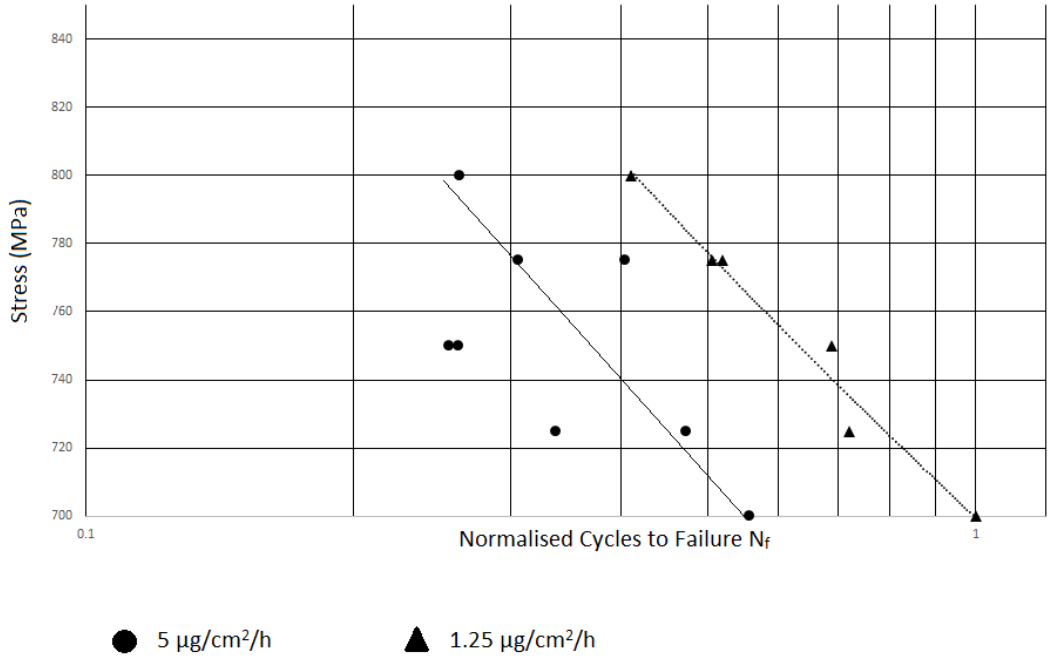

Figure 4.8: 1-1-1-1 (s) S-N curves for CMSX-4 with 500 h of 1.25 or 5 µg/cm^2/h pre corrosion flux at 550°C. This shows a reduction in fatigue life correlating to the salt deposition rate

Optical examination of the fracture faces reveal that the 1.25 µg/cm^2/h flux fractured predominately along a conventional (111) slip plane, whereas 5 µg/cm^2/h flux specimens have a thumb nail feature that failed along the corrosion driven (100) crack plane. Further adding in a 60 second dwell period with a 1-60-1-1 (s) trapezoidal wave form generates multiple crack initiation points comparable to static stress fracture faces (Figure 4.9). These multiple cracks are also visible when viewing the specimen from the side (Figure 4.10). The observation of these additional cracks suggests that short cracks are initiating and growing in dwell periods due to a hot corrosion cracking mechanism.

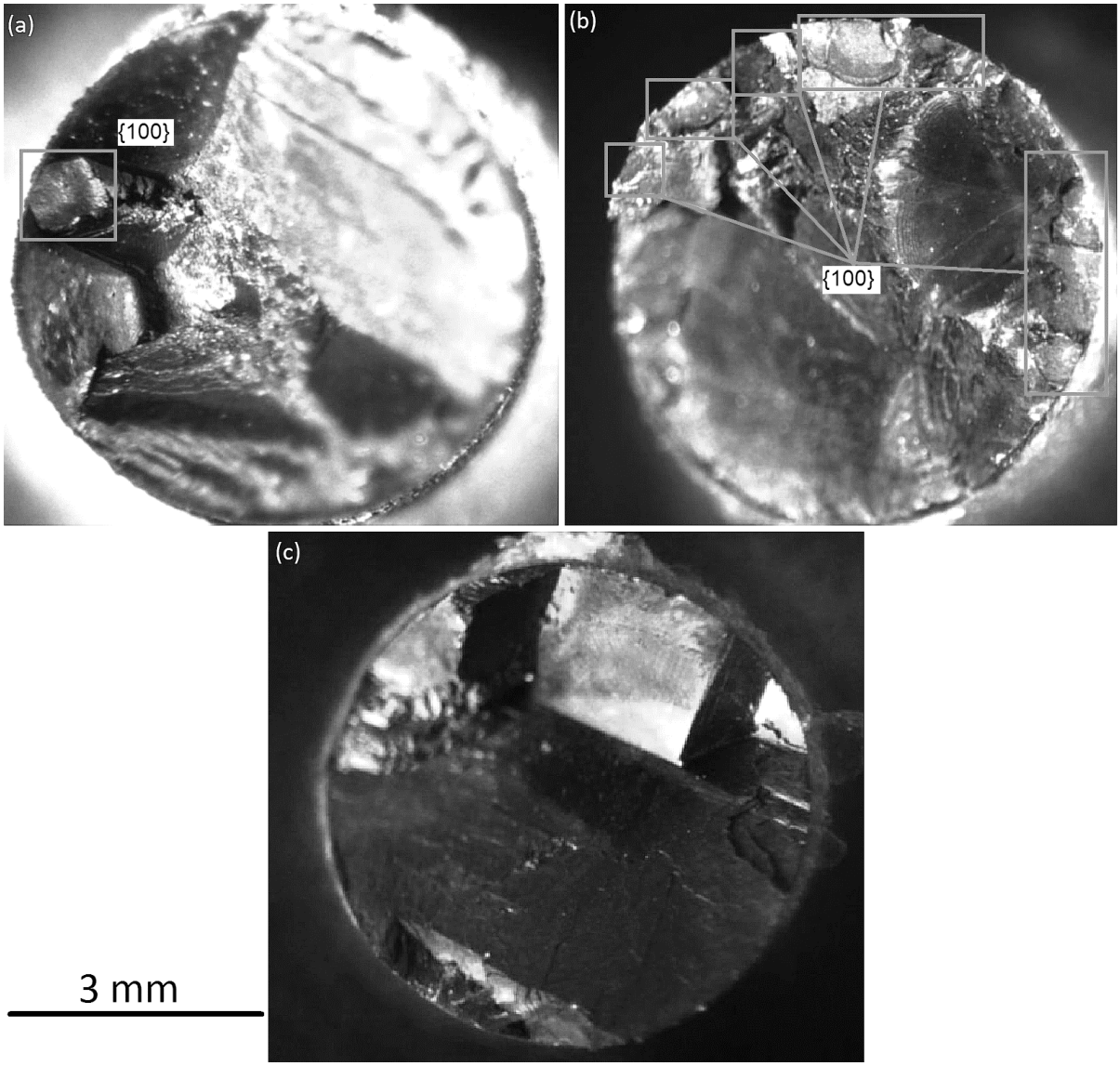

Figure 4.9: Optical images of plain specimen fracture faces, **(a)** 800 MPa, 1-1-1-1 (s) trapezoidal loaded fatigue specimen, 500 h pre corrosion with 5 µg/cm^2/h flux at 550 °C, showing one {100} thumb nail fracture site, **(b)** 800 MPa, 1-60-1-1 (s) trapezoidal loaded fatigue specimen, 500 h pre corrosion with 5 µg/cm^2/h flux at 550 °C, showing multiple {100} thumb nail fracture sites, **(c)** 775 MPa, 1-1-1-1 (s) trapezoidal fatigue specimen, 500 h pre corrosion with 1.25 µg/cm^2/h at 550 °C, showing no optically visible {100} thumb nail fracture sites at this magnification

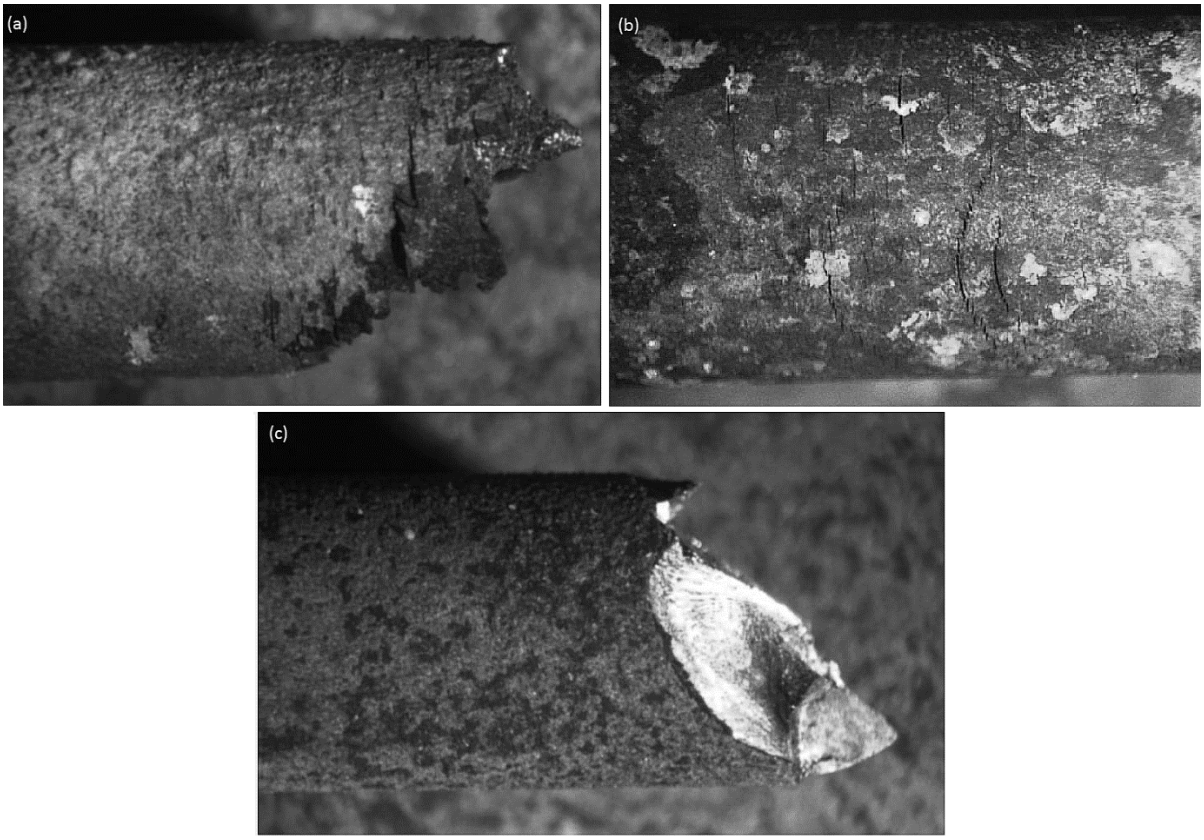

Figure 4.10: Optical images showing side views of plain specimens after test exposures, **(a)** 800 MPa, 1-60-1-1 trapezoidal wave fatigue specimen, 500 h pre corrosion with 5 µg/cm^2/h flux at 550 °C, showing multiple cracks, **(b)** 900 MPa statically loaded 200 h specimen showing multiple cracks comparable with (a), **(c)** 725 MPa, 1-1-1-1 trapezoidal wave fatigue specimen, 500 h pre corrosion with 5 µg/cm^2/h flux at 550 °C showing one optically visible crack

The accelerated failure of fatigue specimens exposed to the lower flux of 1.25 µg/cm^2/h but not exhibiting (100) fracture features, could be attributed to stress concentration due to pitting from type II corrosion generated during pre-corrosion. It is additionally possible that a reduced K_{TH} is induced at the crack tip but that the fracture is still dominated by (111) slip planes, however this short crack growth behaviour requires further investigation.

Examining the corrosion fatigue fracture faces under SEM revealed that darkened beach mark type features were visible (Figure 4.11), mapping of these markings demonstrates that they are associated with oxygen-rich bands (Figure 4.12). These features appear to be too infrequent and have too large a spacing to be associated solely with fatigue striation markings, and are therefore most likely associated with corrosion dwell steps similar to those seen in static stress cracking.

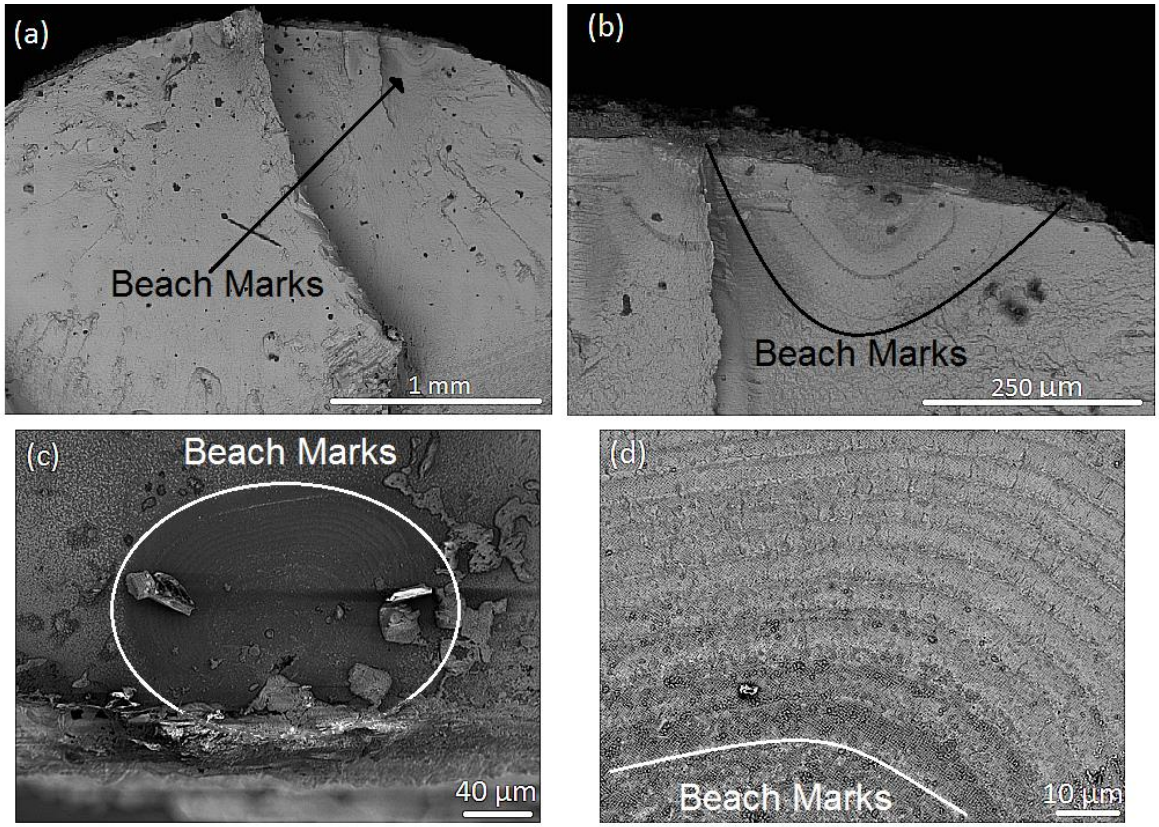

Figure 4.11: SEM microscope images of fatigue specimen fracture surfaces, **(a)** 1-1-1-1 800 MPa, 500 h of 5 µg/cm^2/h pre corrosion showing beach type markings propagating from an initiation point, **(b)** 1-1-1-1 800 MPa, 500 h of 5 µg/cm^2/h pre corrosion at higher magnification showing ta smooth {100} crack plane with environmental markings, **(c)** 1-1-1-1 750 MPa, 500 h of 5 µg/cm^2/h pre corrosion showing smaller microscopic environmentally induced beach type markings propagating from an initiation point, **(d)** 1-1-1-1 750 MPa, 500 h of 5 µg/cm^2/h pre corrosion at higher magnification showing 5-10 µm jumps in environmentally induced markings

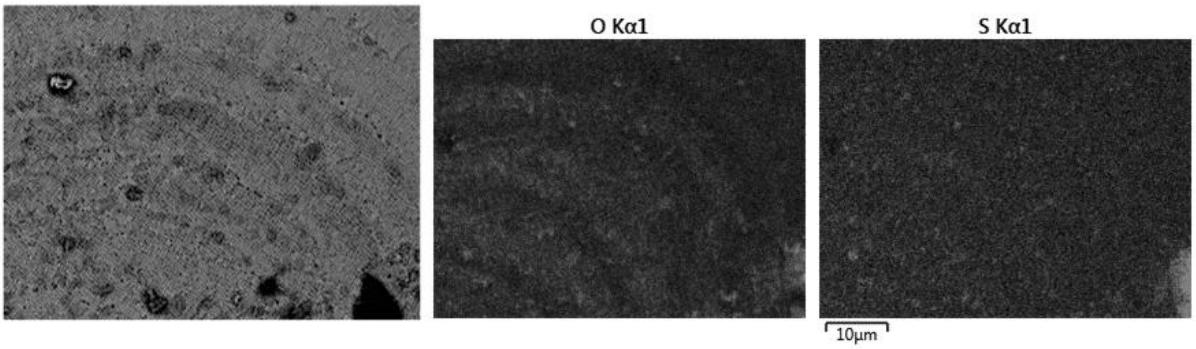

Figure 4.12: SEM EDX mapping of a 1-1-1-1 800 MPa, 500 h of 5 µg/cm^2/h pre corrosion fracture face, showing some banding of oxygen and sulphur maps in correlation with microscopic environmentally induced beach mark type markings

Table 4.5 : Trapezoidal wave form fatigue results with 500 h pre corrosion cycles to failure

R=0 Stress (MPa)	500 h Pre Corrosion (μg/cm^2/h)	[100] Length (mm)	(100) Area Estimate mm^2	Wave Form (s)	Normalised Cycles to Failure N_f	(100) Visible Crack Initiations on Fracture Face
700	5	1.344	4.10	1-1-1-1	0.557	1
725	5	0.6	0.80	1-1-1-1	0.473	1
725	5	1.23	3.54	1-1-1-1	0.338	1
750	5	0.303	0.35	1-1-1-1	0.256	1
750	5	1.221	2.95	1-1-1-1	0.262	1
775	5	1.538	4.68	1-1-1-1	0.307	1
775	5	0	0	1-1-1-1	0.404	0
800	5	0.711	0.80	1-1-1-1	0.263	1
800	5	0.751	2.74	1-60-1-1	0.0597	9
700	1.25	0	0	1-1-1-1	1.001	0
725	1.25	0	0	1-1-1-1	0.722	0
750	1.25	0	0	1-1-1-1	0.689	0
775	1.25	0	0	1-1-1-1	0.505	0
775	1.25	0	0	1-1-1-1	0.52	0
800	1.25	0	0	1-1-1-1	0.411	0

The increased deposition flux rate of 5 μg/cm^2/h exhibited a reduced fatigue life when compared with 1.25 μg/cm^2/h. This reduction in fatigue life was as high as 45% at lower stresses where corrosion had more time to interact with the alloy.

The corrosion mechanisms for fatigue specimens resembled those observed in static stress conditions (Figure 4.13). It is similarly hypothesised that the [100] orthogonal crack growth is driven by gas induced corrosion interacting initially with orthogonal γ' precipitates (Figure 4.5). However this is more prevalent at shorter crack lengths or a lower crack tip ΔK, as a higher ΔK exceeding the K_{TH} of the material fail on the conventional [111] fracture facets causing ridges or rooftops.

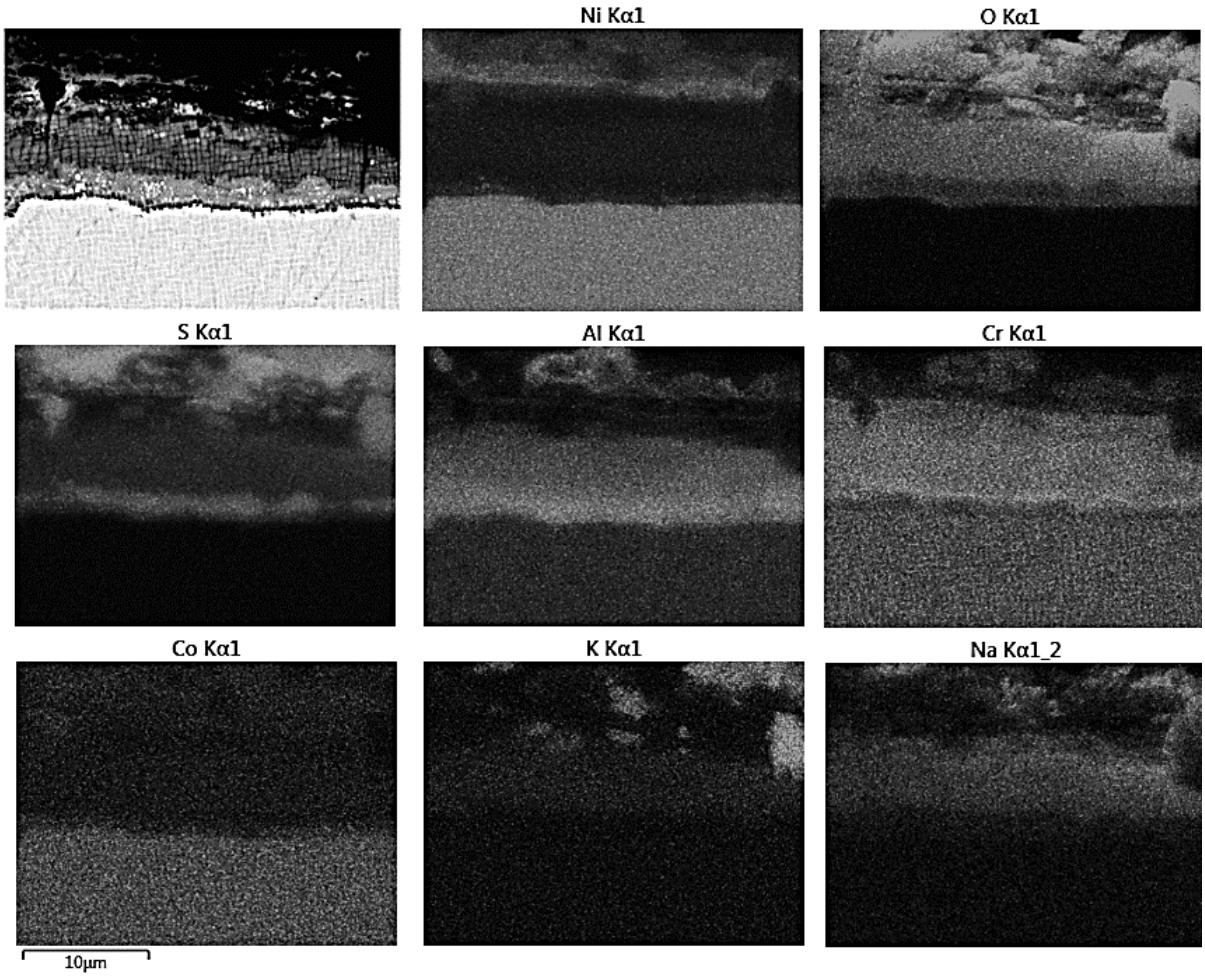

Figure 4.13: SEM EDX mapping of a 1-1-1-1 800 MPa, 500 h of 5 µg/cm^2/h pre corrosion, corrosion fatigue product, this mapping is consistent with EDX mapping of statically loaded specimens and shows segregation in the corrosion products, forming an outer oxide scale of Ni/Co and an inner Cr/Al rich layer with a sulphur rich band reacting with the substrate interface

4.5.3. Fracture analysis

The stress intensities for 50 and 10 µm cracks are presented in Table 4.6 for the three geometries along with the geometry factors. These parameters were calculated from J-integral energies using integrated FE code [28]. For comparison the crack lengths required to exceed the published K_{TH} of 15 MPa·m$^{1/2}$ are also presented.

Table 4.6 : Fracture parameters calculated using FEA for 10 and 50 µm cracks in bodies loaded to a target stress of 800 MPa

Geometry	Crack Length (µm)	K_I (MPa·m$^{1/2}$)	LEFM Geometry Factor	Crack Length needed to exceed K_{TH} (µm)
C-ring	50	10.8	1.08	96
	10	4.8	1.07	98
Plain Specimen	50	10.07	0.99	114
	10	4.45	0.99	114
Three Point Bend	50	7.2	0.72	216
	10	3.33	0.74	204

Review of the fracture mechanics analysis shows that the geometry which generate the most rapid crack initiation and propagation under static loading is the C-rings, followed by the plain specimen and lastly the three point bend. The three point bend specimen is likely less aggressive than the plain specimen due to stress relaxation over the specimen span as a crack initiates and propagates modelling conducted on increasing crack lengths supports this. Conversely the constant uniform stress present in the plain specimen leads to a more conventional increase in stress intensity at the crack tip as a crack propagates.

Comparing the fracture analysis with static stress experimental shows that cracks propagate well below the published K_{cr} of 60 MPa·m$^{1/2}$. Suggesting that localised hot corrosion attack allows the crack to propagate with a static tensile stress present.

Additionally relating the fracture analysis to fatigue testing results demonstrates that fatigue cracks can propagate below the published K_{TH} of 15 MPa·m$^{1/2}$. Suggesting that localised hot corrosion additional has the net effect of reducing the fatigue threshold.

4.6. Paper 3 conclusions

Type II hot corrosion combined with stress, results in a form of stress corrosion cracking, the mechanism was exacerbated by stress gradient. This mechanism initiates and propagates cracks on orthogonal {100} planes.

The presence of Type II hot corrosion also demonstrated an increase in the rate of fatigue propagation, similarly switching the crack propagation direction from <111> to <100> with higher salt deposition fluxes, demonstrating corrosion's influence in on the crack propagation plane.

Longer fatigue dwell periods of 1-60-1-1 and static stress cracking showed increased crack initiations when compared with more fatigue dominated mechanisms. This suggests that cracks could initiate and propagate under dwell periods during fatigue cycles.

Microscopy studies suggested a form of stress assisted type II embrittlement preferential to the γ' occurred at the crack tip.

A stress assisted SO_x gas induced fluxing mechanism at the crack tip was proposed to explain sulphate dependant crack tip embrittlement and <100> orthogonal propagation. More widely documented diffusion/absorption mechanisms for stress corrosion cracking (SCC), such as hydrogen embrittlement and stress assisted grain boundary oxidation (SAGBO) share similar characteristics. But they are not considered particularly active in SC CMSX-4 at these temperatures, and would not be dependent on sulphate fluxing like the mechanism presented in this paper demonstrated.

Micrograph studies of cracks suggest that the propagation mechanism in the more plastic γ channels may differ from that in the more brittle γ'. This resistance of the γ phase to propagation could suggests the importance of Cr in resisting the mechanism.

Further experimental and microscopy work is needed to properly understand the mechanism, specifically if and what species diffuses through the material and how, as well as what affect they have on the plasticity of the γ/γ' microstructure.

Further work to record accurate crack propagation data is required to fully understand and quantify the effects of the mechanism in relation to modelling, particularly at short crack lengths where cracks are more influenced by type II hot corrosion.

Acknowledgements

The authors acknowledge the support of the Engineering and Physical Research Council (EPSRC) for their support for the project - Flexible and Efficient Power Plant: Flex-E-Plant (Grant number: EP/K021095/1). They also thank the following partners for their the valuable contributions: GE Energy, Doosan Babcock Limited, Centrica plc., EDF Energy (West Burton Power) Limited., Uniper Technology Limited, Goodwin Steel Castings Limited, NPL Management Limited, R-MC Power Recovery Limited., RWE Generation UK plc., Scottish and Southern Energy (SSE) plc., Siemens Industrial Turbomachinery, and TWI Limited.

4.7. Paper 3 references

[1] (ASM International), “Hot Corrosion in Gas Turbines,” *High Temp. Corros. Mater. Appl.*, pp. 249–258, 2007.

[2] H. Rosier, K. Perkins, A. Girling, J. Leggett, and G. Gibson, “Factors affecting the corrosion fatigue life in nickel based superalloys for disc applications,” *MATEC Web Conf.*, vol. 14, p. 3001, 2014.

[3] M. M. Rahman, T. K. Ibrahim, and A. N. Abdalla, “Thermodynamic performance analysis of gas-turbine power-plant,” *Phys. Sci.*, vol. 6, no. 14, pp. 3539–3550, 2011.

[4] K. Harris and J. B. Wahl, “Improved single crystal superalloys, CMSX-4 (SLS) [La+Y] and CMSX-486,” *Superalloys 2004 (Tenth Int. Symp.*, no. Figure 1, pp. 45–52, 2004.

[5] N. Birks, G. H. Meier, and F. S. Pettit, “High-Temperature Corrosion Resistance,” *JOM*, vol. 39, no. 12, pp. 28–31, 1987.

[6] N. Eliaz, G. Shemesh, and R. M. Latanision, “Hot corrosion in gas turbine components,” *Eng. Fail. Anal.*, vol. 9, no. 1, pp. 31–43, 2002.

[7] P. Lortrakul, R. W. Trice, K. P. Trumble, and M. A. Dayananda, “Investigation of the mechanisms of Type-II hot corrosion of superalloy CMSX-4,” *Corros. Sci.*, vol. 80, pp. 408–415, 2014.

[8] L. Brooking, J. Sumner, S. Gray, and N. J. Simms, “Stress corrosion of Ni-based superalloys,” *Mater. High Temp.*, vol. 35, no. December, pp. 120–129, 2017.

[9] D. Siebörger, H. Knake, and U. Glatzel, “Temperature dependence of the elastic moduli of the nickel-base superalloy CMSX-4 and its isolated phases,” *Mater. Sci. Eng. A*, vol. 298, no. 1–2, pp. 26–33, 2001.

[10] B. Rengara, S. Baba, and M. Okazaki, “Influence of Crystal Orientation on Cyclic Sliding Friction and Fretting Fatigue Behavior of Single Crystal Ni-Base Superalloys,” in *Superalloys 2016: Proceedings of the 13th International Symposium on Superalloys*, 2016, pp. 395–404.

[11] V. Sass, U. Glatzel, and M. Feller-Kniepmeier, “Creep anisotropy in the monocrystalline nickel-base superalloy CMSX-4,” *Superalloys 1996 8th Int. Symp. Superalloys.*, pp. 283–290, 1996.

[12] M. R. Joyce, X. Wu, and P. a S. Reed, “The effect of environment and orientation on fatigue crack growth behaviour of CMSX-4 nickel base single crystal at 650 °C,” *Mater. Lett.*, vol. 58, no. 1–2, pp. 99–103, 2004.

[13] G. Jianting, D. Ranucci, and E. Picco, “Low cycle fatigue behaviour of cast nickel-base superalloy IN-738LC in air and in hot corrosive environments,” *Materials Science and Engineering*, vol. 58, no. 1. pp. 127–133, 1983.

[14] G. S. Mahobia *et al.*, “Effect of hot corrosion on low cycle fatigue behavior of superalloy IN718,” *Int. J. Fatigue*, vol. 59, pp. 272–281, 2014.

[15] M. Y. Nazmy, “The effect of environment on the high temperature low cycle fatigue

behaviour of cast nickel-base IN-738 alloy," *Mater. Sci. Eng.*, vol. 55, no. 2, pp. 231–237, 1982.

[16] (Westinghouse Combustion Turbine Systems) Allen, J, M and (Westinghouse Reaserch and Development Center) Whitlow, G, A, "Observations on the Interaction of High Mean Stress and Type II Hot Corrosion on the Fatigue Behavior of a Nickel Base Superalloy," *J. Eng. Gas Turbines Power*, vol. 107, pp. 220–224, 1985.

[17] P. De Marrocos and A. R. Pais, "Influence of stress state on high temperature fatigue crack growth in," pp. 127–135, 2001.

[18] M. Rezazadeh, M. Alizadeh, and A. Fathi, "Turbine blade temperature calculation and life estimation - a sensitivity analysis," *Propuls. Power Res.*, vol. 2, no. 2, pp. 148–161, 2013.

[19] T. L. Anderson, *Fracture Mechanics: Fundamentals and Applications*, vol. 58, no. 1. 2012.

[20] J. R. Donahue, A. B. Lass, and J. T. Burns, "The interaction of corrosion fatigue and stress-corrosion cracking in a precipitation-hardened martensitic stainless steel," *npj Mater. Degrad.*, vol. 1, no. 1, p. 11, 2017.

[21] G. Henaff, K. Marchal, and J. Petit, "On fatigue crack propagation enhancement by a gaseous atmosphere: Experimental and theoretical aspects," *Acta Metall. Mater.*, vol. 43, no. 8, pp. 2931–2942, 1995.

[22] X. J. Wu, M. Miller, Z. Zhang, J. Miller, and P. A. S. Reed, "Fracture Mechanics Analysis of Notch Fatigue of A Single Crystal Superalloy—CMSX-4," *Icf11*, pp. 6–10, 2005.

[23] ISO 7539-5, "Corrosion of metals and alloys - Stress corrosion testing - Part 5: Preparation and use of C-ring specimens," no. 1, 1989.

[24] British Standards Institutions, "BSI Standards Publication Plastics — Determination of flexural properties," 2013.

[25] "Image-J." Oxford Instruments, 2017.

[26] "AZtec." Oxford Intsruments, 2015.

[27] "ANSYS Workbench 15.0." ANSYS, 2013.

[28] "Abaqus/CAE." SIMULA, 2017.

[29] N. E. Dowling, *Mechanical Behavior of Materials*, 4th ed. Boston, MA : Pearson, 2012.

5. Paper 4: Analysis of combined static load and low temperature hot corrosion induced cracking in a Ni-based single crystal superalloy

L.Brooking[1], S.Gray[1*], K.Dawson[2], J.R.Nicholls[1], N.J.Simms[1], J.Sumner[1], G. J.Tatlock[2]

[1]Cranfield University, College Rd, Cranfield, MK43 OAL

[2]Department of Mechanical, Materials and Aerospace Engineering, School of Engineering, University of Liverpool, Liverpool L69 3GH

Abstract. Gas turbine (GT) designers aim to optimise material selection and component design in order to increase turbine efficiencies and reduce component life cycle costs. Due to the demanding environments, in which turbine blades are required to operate, there are a number of degradation mechanisms that have to be considered in the design process, such as creep, high temperature corrosion and fatigue. Historically, material data for independent degradation mechanisms have been used to predict GT blade lives under given conditions, however, recent research has led to developments demonstrating interactions between low temperature hot corrosion and load, resulting in an environment and time dependent cracking mechanism in superalloys. This paper uses SEM, (S)TEM and EDX techniques to analyse cracking generated in a single crystal alloy (CMSX-4) statically loaded three point bend specimen that was subjected to stress assisted low temperature hot corrosion conditions. It was observed that cracks propagate through γ' precipitates resulting in propagation on {001} planes. Octahedral <111> faults or slip traces were also present ahead of the crack tip, as well as sulphur, chlorine, sodium and oxygen at the crack tip. An influence of loading/deformation on the corrosion mechanism's preference to interaction with either the γ or γ' was observed. The findings suggest that the corrosive mechanism could be a stress assisted electrochemical reaction linked with low temperature hot corrosion, where crack propagation occurs as a result of localised corrosion enhanced interatomic de-cohesion. Steep segregation profiles for W and Ta were also observed near the edges of the γ' regions and may be linked to a strain induced mechanism.

Keywords: Single crystal superalloy, Hot corrosion, Stress corrosion cracking, TEM

5.1. Introduction

Gas turbine (GT) systems are used for a range of applications in the aerospace and power generation sectors. In addition to economic pressures to improve the efficiencies of GT systems, emissions legislation and incentives are further driving the industry to develop more efficient designs [1][2][3]. In response to these factors, GT manufacturers are looking for ways to increase the turbine inlet temperatures to improve the thermodynamic efficiency of the turbine system [4] . One of the key limiting factors in achieving this is the turbine blade's material capabilities at high temperature e.g. its corrosion resistance and performance. In recent times it has been observed that tensile loading combined with conditions approaching those required for low temperature hot corrosion (LTHC), can lead to crack propagation not predicted by conventional fatigue or corrosion models [5][6]. This mechanism could prove particularly significant in lower temperature regions of GT blades at 450-650^{o}C, that are additionally under tensile loading conditions such as experienced by under platform regions. Due to their good high temperature properties, Ni-based single crystal (SC) superalloys are commonly used for 1st stage turbine blades [7][8]. These materials consist of a coherent SC structure made up of two phases, the gamma-prime (γ') strengthening phase (which is an ordered $L1_2$ structure such as Ni_3Al) and the face centred cubic (FCC) gamma-matrix (γ) [9][10].

SC superalloys demonstrate anisotropic behaviour. For example the elastic modulus of CMSX-4 in the [111] direction is about three times larger than along [001] [11]. The [001] direction however, exhibits the best creep resistance [12]. Therefore, turbine blades are normally oriented with the [001] direction aligned to the critical creep direction. In SC superalloys, and specifically CMSX-4, the γ' phase is typically thought to contain Ni, Ti, Al and Ta; whilst the γ is typically thought to contain Ni, Mo, Co, Cr, W and Re [13][14].

Previous research into similar cracking mechanisms has largely focused on two mechanisms in order to quantify and explain the effects of combined loading and LTHC. In the first, the effect of LTHC on increasing the rate of fatigue crack propagation is a result of load cycles [6][15][16][17].In the second stress concentration generated by LTHC pitting, results in accelerated fatigue crack initiation [18][19][20].

Recent research conducted on statically loaded C-rings and three point bend specimens, however, demonstrated a combined static stress and LTHC crack initiation and propagation mechanism [21][5]. This work highlighted the significance of a third, time-dependant mechanism which requires a corrosive salt deposit, in this case of 80/20 wt% Na/K sulphate, a gas flow containing SO_x and a tensile loading condition. It was found that a time dependant LTHC assisted crack propagation mechanism occurred below the expected fatigue stress intensity threshold (K_{TH}), and propagated on preferential orthogonal {001} planes, as opposed to on the {111} octahedral planes expected for quasi-brittle/brittle fracture at temperatures below 750^{o}C under mode I crack opening [22][23][24][12].

Parallels between static load/stress LTHC cracking can be drawn with more conventional stress corrosion cracking (SCC) mechanisms. Generally, SCC is considered to be interactions

between mechanical load and corrosion of the material, resulting in crack initiation and propagation [25]. Whilst SCC generated in LTHC environments is not well studied, there are three normally lower temperature mechanisms commonly attributed with SCC in both ferritic and nickel-based alloys, these are described below.

Firstly, SCC can be generated with electrochemical corrosion conditions; this has been studied in ferritic and nickel-based alloys, where corrosion was controlled through adjustment of the electrochemical potential [26][27]. SCC in SC stainless steels has been studied, where corrosion was generated through electrochemistry. Specimens were submerged in a liquid electrolyte and an electrical potential applied across them, generating corrosion at a localised anodic region resulting in SCC initiation and propagation [28][29][30].

Secondly, SCC can be generated through stress assisted grain boundary oxidation (SAGBO), occurring in polycrystalline materials [31][32][33]. It has been hypothesised that SAGBO occurs due to the formation of niobium oxides on grain boundaries in Ni-based superalloys [34]. Whilst not directly applicable to SC alloys, SAGBO is an example of stress assisting oxidation in crystalline materials. It has additionally been found that Cl and S containing vapours can further accelerate gas phase induced SAGBO in Ni-based superalloys [35][36].

Thirdly, SCC can be generated by the active element, hydrogen; this is referred to as hydrogen embrittlement and has been reported in Ni-based alloys at temperatures between 250-430^{o}C [37][38]. Whilst there is no definitive mechanism for hydrogen embrittlement, it is generally considered to occur as a result of absorption or diffusion of cathodic H^{+} hydrogen, and requires a wet environment, or high partial pressure of hydrogen for significant adsorption to occur [39][40].

Several mechanisms for hydrogen embrittlement have been proposed; these were summarised by Lynch [41], with the overall mechanism being referred to as adsorption induced dislocation emissions (AIDE). AIDE is thought to occur as a result of both adsorbed hydrogen enhancing de-cohesion and weakening of interatomic bonds (HEDE), and hydrogen enhancing local plasticity (HELP) [42]. Hydrogen diffusion has been studied and measured in SC nickel FCC systems [43][44]. It was demonstrated that hydrogen diffusion is anisotropic in such systems, with the diffusion rate being faster in the <111> crystallographic directions.

Corrosion mechanisms such as chloridation (the formation of metal chlorides) [45], and sulphidation (the formation of metal sulphides) [46][47], can facilitate/accelerate the corrosion and oxidation of alloys. LTHC is a fluxing mechanism which historically was reported to occur between 600^{o}C – 800^{o}C [48][49][50].

Recent studies have generated LTHC in CMSX-4 at temperatures as low as 575^{o}C [51], and stress has been credited as further lowering the temperature required for LTHC to propagate [6]. LTHC is dependent on both a deposit flux of salts and a gas flow containing S (with/without Cl), this environment results in the formation of a liquid eutectic on the surface.

Superalloys form oxide scales which protect against further oxidation of the substrate alloy. The most protective of these oxides are chromium oxide and aluminium oxide, where chromia

is often considered more stable for lower temperatures up to 700°C and alumina at higher temperatures above 900°C [52].

It is generally thought that LTHC accelerates/enables corrosion through the formation of a liquid eutectic, which results in the dissolution of the protective oxide scale, e.g. through acidic fluxing where dissolved SO_x is the oxidising agent. It has further been proposed that the local oxidising potential of LTHC is the result of an electrochemical reaction, where the liquid eutectic mixture acts as an electrolyte [53][54].

Crystalline materials form atomic defects and dislocations when loading and deformation occurs. These atomic defects are the microstructural mechanisms behind plastic deformation and conventional fatigue crack initiation and propagation. Atomic defects are often categorised into three main categories: point defects on specific sites, line defects such as edge dislocations and screw dislocation and planar defects such as stacking faults and grain boundaries [55]. These atomic defects can aid and/or enable the diffusion and absorption of atoms into the material which can then further disturb the atomic structure.

Stress/strain effects on the electrochemical potential or mechanical chemical interactions have been observed and reported in crystalline materials [56][57]. It was demonstrated that increased tensile deformation can result in an increase in the anodic potential and result in accelerated corrosion. Relationships between deformation and potential difference are more commonly referred to as piezoelectric effects.

This paper considers the mechanisms proposed in the literature for other more widely understood forms of SCC and compares them with detailed microscopy of the LTHC mechanism presented in this work. A mechanism is then proposed for crack propagation occurring under static load and LTHC conditions.

5.2. Experimental methods

A three point bend jig was designed for use within a hot corrosion furnace, which applied a constant displacement condition to a specimen (Figure 5.1). Three point bend specimens were machined with the [001] direction aligned as shown in Figure 5.1, while the secondary orientation was not controlled. To calculate the displacement required to meet the initial load condition, BSI standard calculations were used [58], these were further confirmed with finite element (FE) analysis, the results of which have been previously published [5].

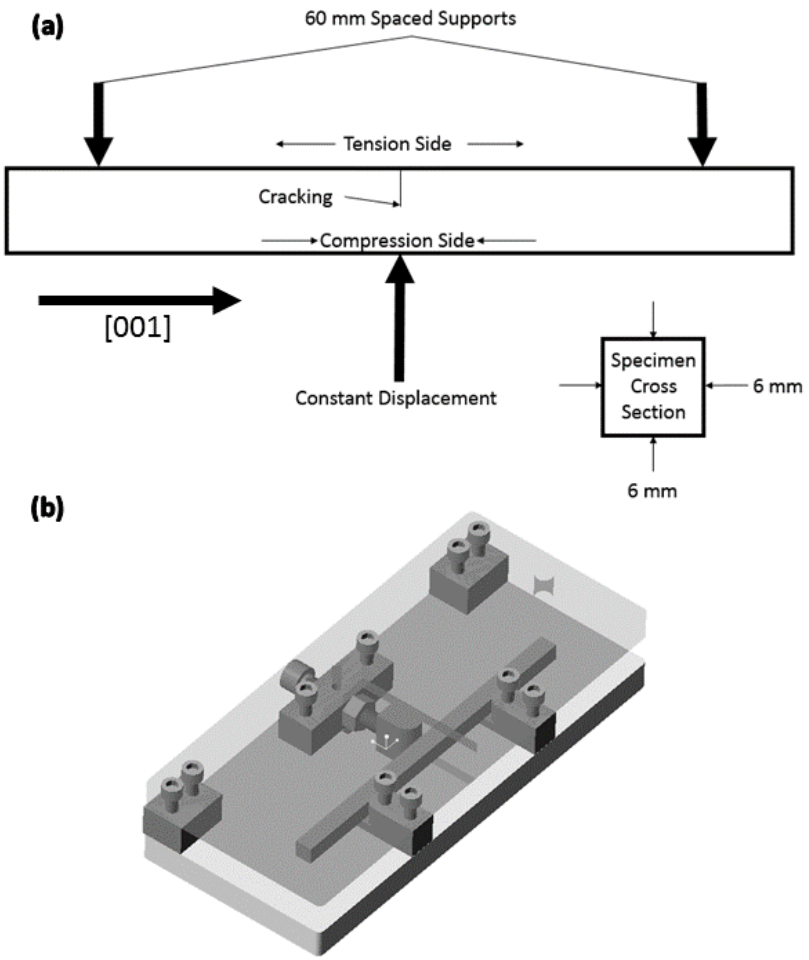

Figure 5.1: (a) Specimen geometry (b) Three point bend test jig

LTHC conditions representative of under platform turbine conditions were produced at 550°C using a deposit recoat methodology [59]. The deposit used was 80/20 wt% Na/K sulphate, which was deposited every 100 h of testing to maintain a flux of 5 $\mu g cm^{-2} h^{-1}$. A test gas of air/300 ppm SO_x was used and the test specimen was exposed for 200 h in total by which time cracks were clearly visible under an optical microscope.

To compare corrosion effects under both tension and compression, both the opposing tensile and compressively loaded sides of the specimens were coated with salt deposit equally. The remaining sides were masked off using aluminium foil in order to prevent their exposure to LTHC and more accurately control corrosion in the areas being studied.

TEM/STEM images were taken with a JEOL 2100F microscope, fitted with an aberration corrector and operating at 200kv. EDX analysis was carried out using an EDAX Optima 60 windowless SDD detector, and the analytical data was analysed using EDAX TEAM software.

5.3. Results and discussion

Cracking was observed exclusively on the specimen surface exposed to tensile loading. SEM imaging of the cracked cross section of the specimen is presented in Figure 5.2. Crack propagation in the <100> direction can be seen, with corrosion preferentially interacting with the γ′ precipitates around the crack tip region. Comparison of corrosion occurring under tensile load with that occurring on the same specimen under compressive load, shows a preference for corrosion to attack the γ′ precipitates under tension and γ channels under compression. This suggests a stress related effect is influencing the balance of preferential γ′/γ attack. It could be suggested that corrosion would normally be preferential to the γ′ at these temperatures, due to higher levels of Cr in the γ providing more protection against LTHC at 550°C.

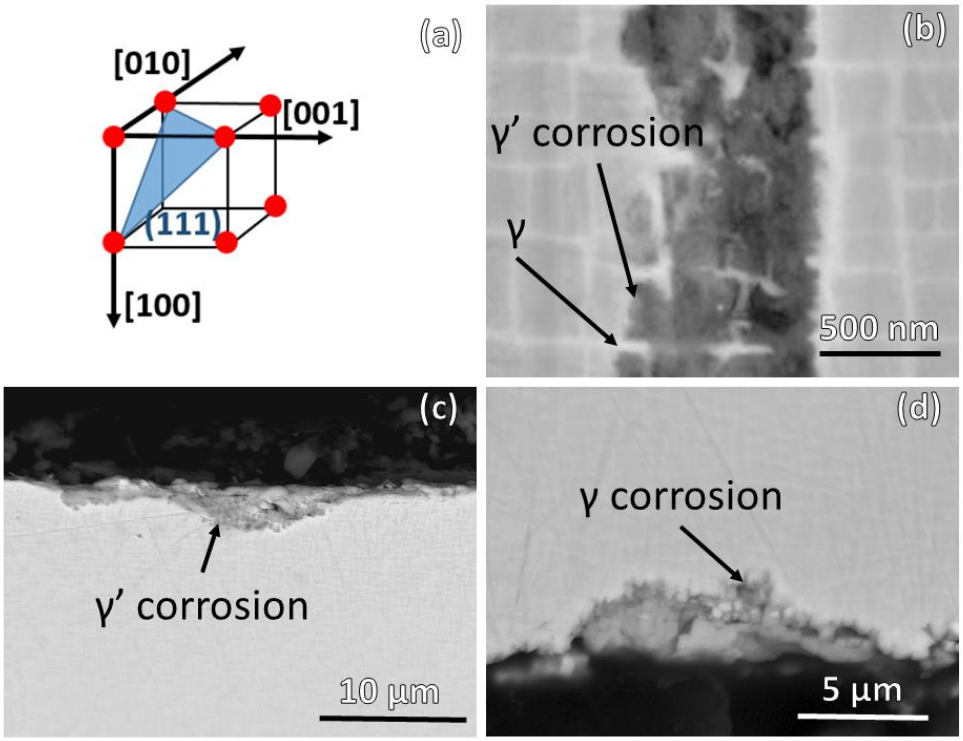

Figure 5.2: (a) General crystallographic alignment for SEM/TEM images presented (b) Back scattered SEM image showing <100> crack propagation with preferential gamma-prime corrosion attack (c) Back scattered SEM image showing corrosion attack under tensile load with preferential gamma-prime attack (d) Back scattered SEM image showing corrosion attack under compressive load with preferential gamma attack

High magnification dark field TEM imaging of the γ/γ′ interface confirmed good crystallographic coherence between these phases (Figure 5.3) at room temperature. Imaging of the crack tip (Figure 5.4) showed cracks cutting through γ′ precipitates and propagating in the <100> direction. Ahead of the crack tip, localised {111} slip traces/stacking faults were visible in γ′. These crystal defects were local to the crack tip, however, and do not appear to have influenced the propagation path of the crack in previous crack growth. Indeed, remnants

of other faults were not found along the path of the crack and it could therefore be suggested that plasticity and defect based mechanisms of crack propagation such as corrosion enhanced plasticity, were not key contributors to the crack advancement in this mechanism.

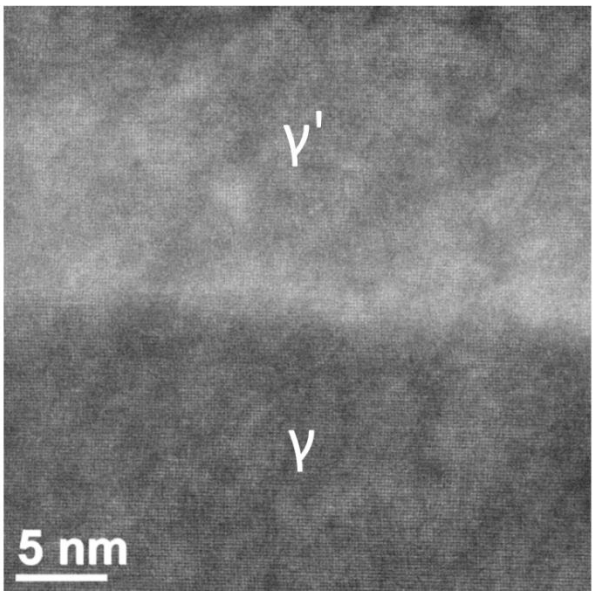

Figure 5.3: Dark-field TEM image of gamma/gamma-prime interface showing good lattice coherence between the phases

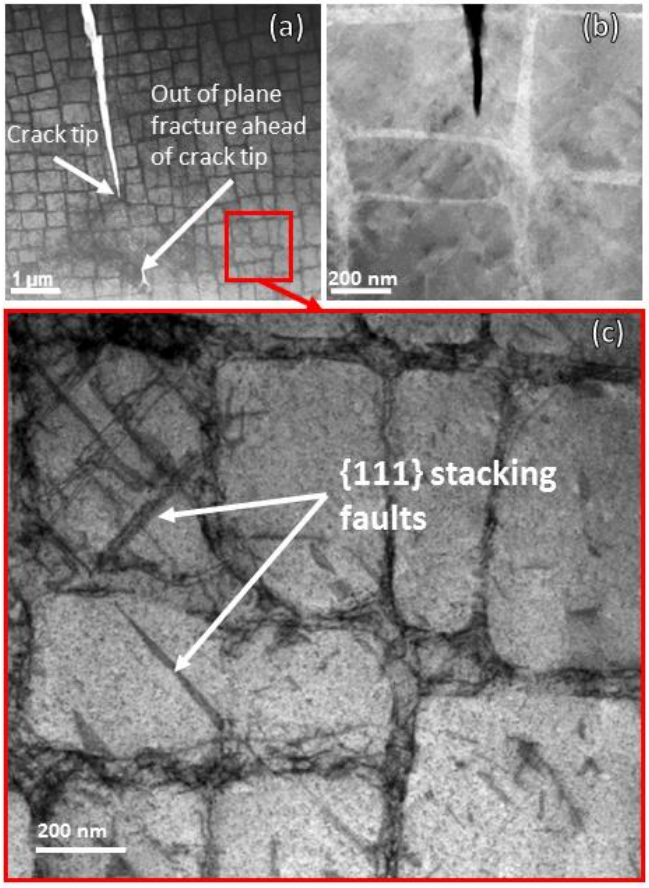

Figure 5.4: (a) Dark field TEM image of the crack tip showing defect contrast (b) Back scattered SEM image of crack tip (c) Higher magnification TEM image from shown location in image (a) ahead of the crack tip, showing stacking defects in the gamma-prime on {111} planes

High magnification dark field TEM imaging of the γ/γ' interface confirmed good crystallographic coherence between these phases (Figure 5.3) at room temperature. Imaging of the crack tip (Figure 5.4) showed cracks cutting through γ' precipitates and propagating in the <100> direction. Ahead of the crack tip, localised {111} slip traces/stacking faults were visible in γ'. These crystal defects were local to the crack tip, however, and do not appear to have influenced the propagation path of the crack in previous crack growth. Indeed, remnants of other faults were not found along the path of the crack and it could therefore be suggested that plasticity and defect based mechanisms of crack propagation such as corrosion enhanced plasticity, were not key contributors to the crack advancement in this mechanism.

Figure 5.5 appears to show strong segregation of elements between the γ and γ' phases, with a higher concentration of Cr, Co and Mo in the γ channels, and a higher concentration of Ni, Al, Si, Ti and Ta in the γ' precipitates. However, elemental maps such as these need to be analysed with care, since overlapping peaks in the EDX spectra can lead to anomalous results in the elemental maps, if not taken into account. Overlapping or adjacent peaks for O and Cr, Si and W, S and Mo, and Ni and Ta, for example, should all be borne in mind. All the segregation effects noted above do seem to accord with previously published EPMA, STEM

and APT results on this alloy. The exceptions are W, Ta and Al, which show segregation gradients towards the γ'/ γ interfaces, but within the γ' precipitates.

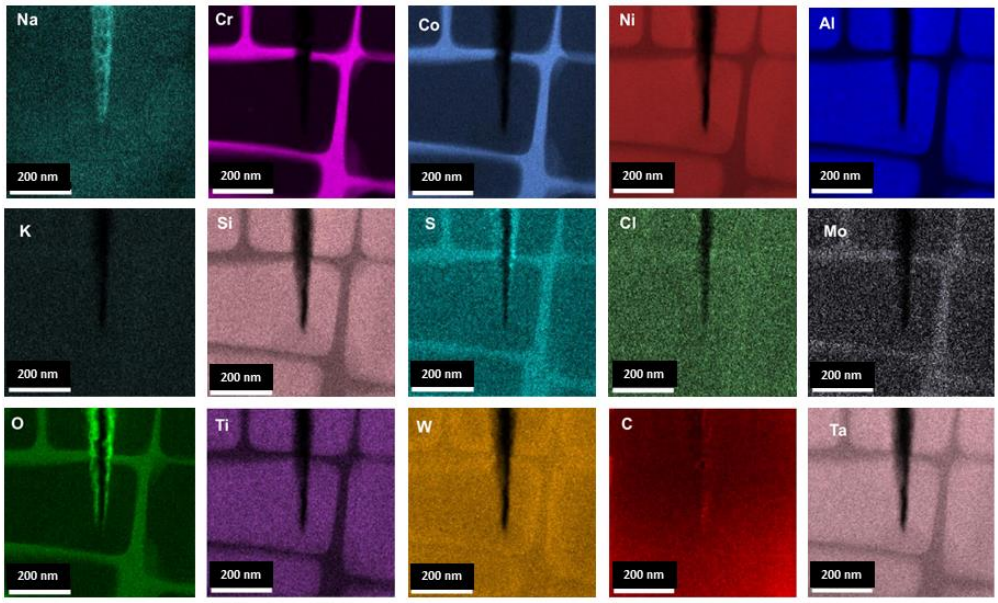

Figure 5.5: STEM EDX mapping showing elemental segragation between the bulk γ'/ γ and the crack tip post-exposure

The starting point for any discussion about segregation between the γ and γ' phases is the Ni-Al phase diagram [60]. This shows that although Al is soluble in a Ni matrix, the solubility decreases markedly as the temperature is reduced. However, even at 400°C, a Ni solid solution can absorb about 8 at% of Al before the ordered γ' phase is formed. To a first approximation, this can be understood when the sizes of the respective elements are considered. Table 1 lists the Goldschmidt radii of the most common elements in CMSX-4 [61]. In particular the table shows that Al is much larger than Ni; hence as the composition of the alloy becomes richer in Al, the ordered γ' phase is preferred, since this keeps the Al atoms as far apart as possible in a face centred cubic lattice. The sizes of Cr and Co are also similar to that of Ni so it is hardly surprising that they tend to sit on the Ni sites in the γ or γ' phases. In the specific case of CMSX-4, they tend to segregate primarily to the γ phase. On the other hand, the refractory elements such as Mo, W and Ta have much larger radii than Ni and hence might be expected to substitute for Al in the γ' structure. Indeed Ta, with a similar radius to Al does indeed segregate strongly to the aluminium sites in the γ' structure [62]. The situation for Mo and W is less clear cut, with Mo reported to segregate to the γ phase in a Ni-Al-Mo ternary alloy [63]. First-principles calculations by the same authors, however, do suggest that when Mo is present in the γ' structure, it would substitute preferentially on the Al sub-lattice.

Table 5.1 : Goldschmidt atomic radii (in nm) of the main elements in CMSX-4 [61]

Ni	**0.125**
Al	**0.143**
Co	**0.126**
Cr	**0.128**
Ta	**0.147**
W	**0.141**
Re	**0.138**
Ti	**0.147**
Mo	**0.140**

The partitioning between γ and γ′ is often described by a partitioning ratio $K_i^{\gamma'/\gamma}$, which is defined as the ratio of the concentration of element *i* in the γ′ precipitate to its concentration in the γ matrix. Hence in the case of Ta, for example, $K_{Ta}^{\gamma'/\gamma} >> 1$. The partitioning of W is more complex. In a quaternary Ni-Al-Cr-W alloy, for example, it has been reported [64] that there was twice as much W found in the γ′ phase as the γ phase. However, Amouyal et al [65] showed that partitioning of W is strongly influenced by the presence of Ta in a Ni based superalloy. Hence, for example, in a ternary Ni-Al-W alloy, W segregates to the γ′ phase with $K_W^{\gamma'/\gamma} = 1.4$ but in a multicomponent alloy containing 1 at% Ta the W segregates to γ with $K_{Ta}^{\gamma'/\gamma} = 0.92$. Ta is such a strong γ′ segregant that its presence leads to site competition between the Ta and W. Indeed, Thermo-Calc calculations by Amouyal et al [66] suggest that the value of $K_W^{\gamma'/\gamma}$ decreases with increasing Ta concentration with a cross-over ($K_W^{\gamma'/\gamma} >1$ to $K_W^{\gamma'/\gamma} <1$) for a Ta concentration of 2 at% at 800°C. In an alloy such as CMSX-4, which contains additions of Mo and Re as well as W and Ta, all the interactions between the different components may need to be considered. However, the results reported here would appear to show that the W/Ta and W/Al interactions are the most dominant. Ta does segregate very strongly to the γ′ phase in CMSX-4 but there also appears to be an inverse correlation between the Ta concentration and the concentration of W near the edges of the γ′ precipitates. The W concentration is similar at the centre of the γ and γ′ regions, but the W signal rises strongly within the γ′ as the edges of the precipitates are approached. It then falls sharply at the γ/γ′ interface. The Ta and Al concentrations are very high at the centre of the γ′ precipitates but drop near the edges of the γ′ as the W signal increases, as shown in the line profiles in Figure 5.6. The distance over which these changes are observed is several nm – too wide for beam broadening or instrumental broadening effects due to the proximity of the interface – and are not mirrored in the Cr or Re profile, for example. Hence there must be another explanation for the change in W segregation near the edges of the γ′ regions. Since the change extends over several nm, it is unlikely to be due to electronic structure changes associated with the γ/γ′ interface, which are usually confined to first or second nearest neighbours [66]. A more likely explanation is the influence of strain on the segregation profile. It has been shown, for example, that variations in Mo concentration can have a major influence on lattice misfit and creep resistance of multicomponent alloys, although there was no evidence of Mo segregation at the γ/ γ′ interface [67,68].

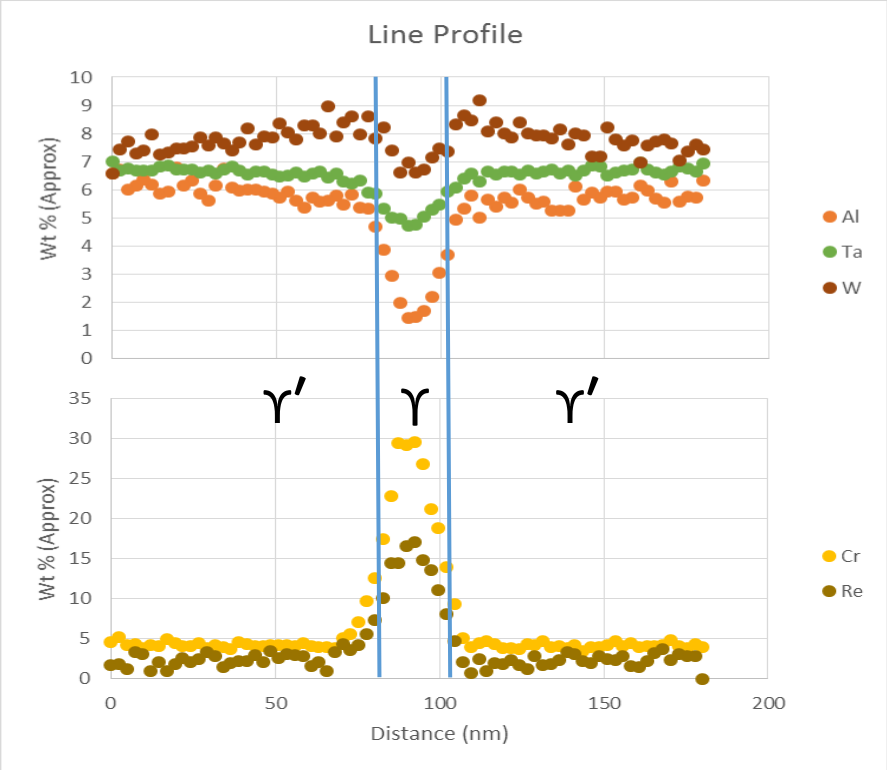

Figure 5.6: Line profiles for Al, Ta, W, Cr and Re across a ϒ′/ϒ/ϒ′ interface showing the build-up of W near the edge of the ϒ′ particles and the corresponding reduction in Ta and Al.

It has been reported that the misfit parameter, δ, given by $\delta = 2(a_{\gamma'} - a_{\gamma})/(a_{\gamma'} + a_{\gamma})$, where $a_{\gamma'}$ and a_{γ} are the lattice parameters of the γ′ phase and the γ matrix respectively [69], should have a positive value at both low and high temperatures, but decrease in magnitude at high temperatures, to achieve optimum creep performance [70]. In order to minimise any major interface strain, the segregation of W from the γ matrix into the γ′ zone may occur, either during high temperature heat treatment – a steady state condition – or in a more transitory way, as the sample is cooled. Given the low diffusivity of W in a Ni matrix compared to other substitutional elements [71], the former explanation seems more likely. The presence of a W gradient prior to testing at 550°C would appear to reinforce that view.

Further EDX mapping of the fracture feature visible ahead of the crack tip in Figure 5.4 is presented in Figure 5.7. It can be concluded that the feature has been exposed to the corrosive environment as it contains environmental contaminants Na, O and S. This supports the hypothesis that the feature is a section of an out of plane crack rather that an internal defect. The feature also contains a small amount of Cl, the presence of which is most likely explained by contamination in the Na/K sulphate compound used for the deposit during testing. However, its presence at the crack tip suggests that chlorides could be significant in regards to load and LTHC interaction mechanisms, and further chloride based salts should be considered in future research.

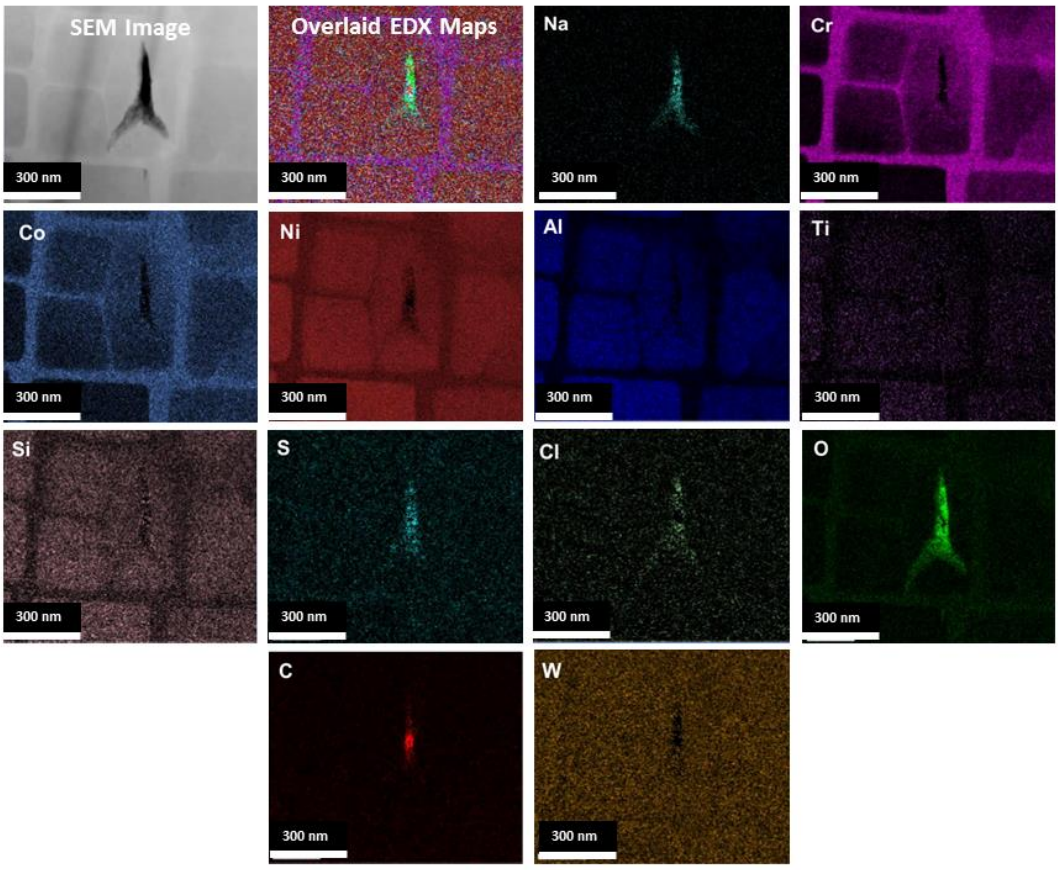

Figure 5.7: STEM EDX mapping of feature ahead of the crack tip containing environmental elements, determined to be related to an out of plane crack

There was no evidence found to support hydrogen embrittlement as the key crack advancement/propagation mechanism. Additionally, hydrogen is unlikely to play a key role in experimental testing due to the dry environment present, and the resultant low partial pressures of hydrogen. However, service conditions of GT blades often contain higher concentrations and therefore the effects of hydrogen should also be studied in future research.

The presence of electrolytes, specifically Na_2SO_4 at the crack tip is supportive as to there being an electrochemical aspect to the LTHC mechanism in this critical location. Due to the static loading condition, it is clear that crack advancement is enabled by the local environment and conditions at the crack tip under LTHC conditions.

Following the same deduction that an electrochemical corrosion mechanism is plausible at the crack tip, mechanical-chemical effects in the γ/ γ’ microstructure provide an explanation for the preference of corrosion attack to the phases independently. It is postulated that this could be as a result of the local strain conditions of the phases affecting the anodic potential of the two phases to a differing extent [56][57].

A schematic of a proposed localised electrochemical hot corrosion mechanism at the crack tip is presented in Figure 5.8. The mechanism defines a general electrochemistry also commonly associated with other more widely understood forms of SCC and pitting corrosion.

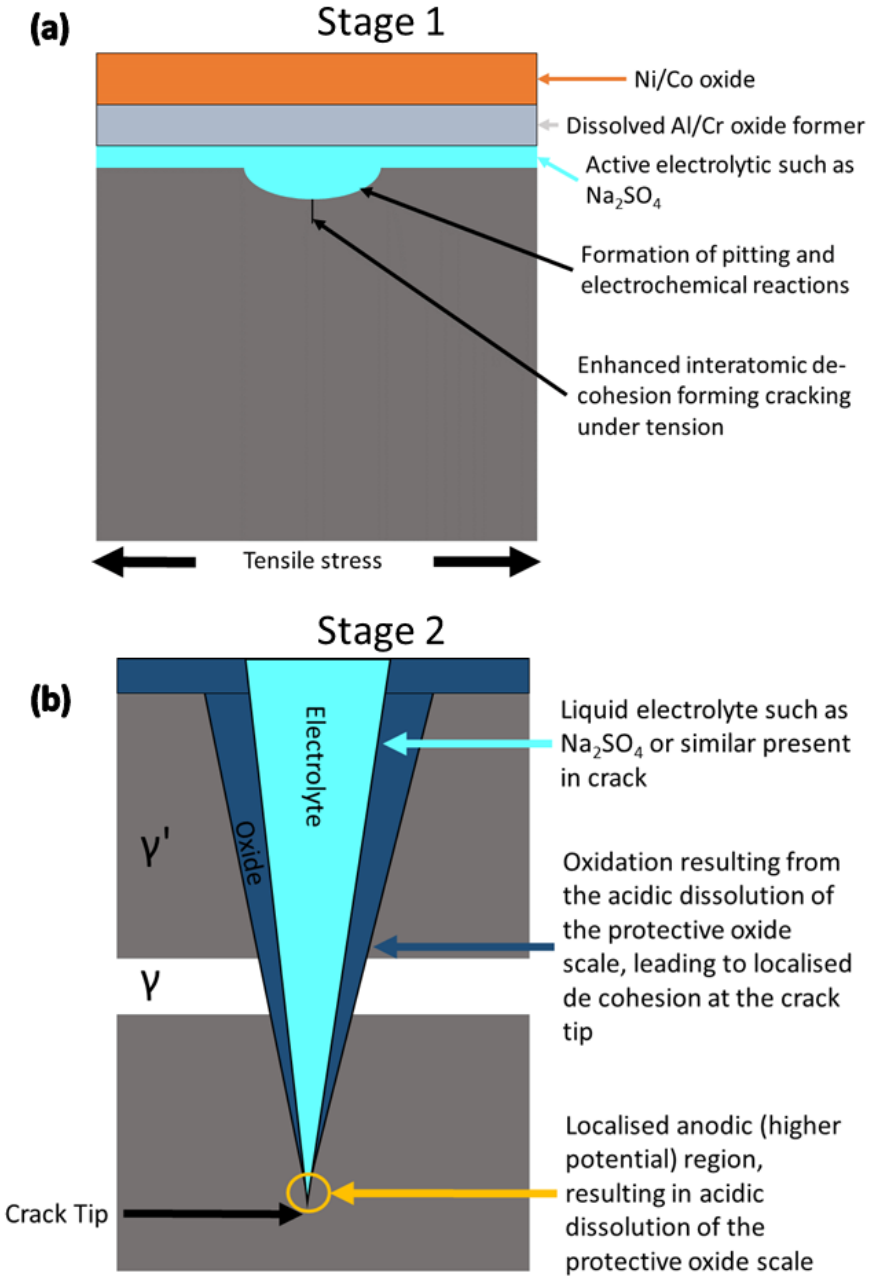

Figure 5.8: Proposed mechanism of electrochemical corrosion at the crack tip (a) Stage 1 where LTHC initiates and small pits start to form (b) Stage 2 where a crack has propagated and electrochemically driven corrosion is established at the crack tip

5.4. Paper 4 conclusions

A form of high temperature SCC has been studied. Crack initiation and advancement was dependant on the simultaneous occurrence of LTHC and loading/deformation. The local chemistry at the crack tip suggested the role of liquid Na_2SO_4 on crack advancement.

It is suggested that electrochemistry may have an important role in both the LTHC mechanism, and the more local crack tip corrosion mechanism, specifically by stress/deformation locally increasing the electrochemical potential.

It is also suggested that deformation of the γ/ γ' could result in mechanical-chemical interactions effecting the chemical potential of the microstructural phases and resulting in preferential corrosion attack under different loading conditions such as compression and tension.

Due to the lack of evidence of absorption or diffusion ahead of the crack tip, or corrosion enhanced plasticity driving crack propagation. It is proposed that the strain/stress required for interatomic de-cohesion is reduced by the localised corrosion occurring at the crack tip, and this results in crack advancement and propagation under static loading.

Detailed EDX mapping found that tungsten segregated close to the γ/ γ' interface, but was concentrated in the γ' in this alloy. This has not been observed before, but a possible cause of W occupying Ta or Al sites on the edges of the γ' has been suggested although this requires further exploration.

Due to the prominence of Cl in lower temperature hot corrosion mechanisms such as the 550 ^{o}C mechanism studied in this paper, further work to analysis the effect of Cl based salts on this mechanism is recommended.

Acknowledgements

The authors acknowledge the support of the Engineering and Physical Research Council (EPSRC) for their support for the project - Flexible and Efficient Power Plant: Flex-E-Plant (Grant number: EP/K021095/1). They also thank the following partners for their the valuable contributions: GE Energy, Doosan Babcock Limited, Centrica plc., EDF Energy (West Burton Power) Limited., Uniper Technology Limited, Goodwin Steel Castings Limited, NPL Management Limited, R-MC Power Recovery Limited., RWE Generation UK plc., Scottish and Southern Energy (SSE) plc., Siemens Industrial Turbomachinery, and TWI Limited.

5.5. Paper 4 references

[1] P. E. Sikorska, “The need for legal regulation of global emissions from the aviation industry in the context of emerging aerospace vehicles,” *Int. Comp. Jurisprud.*, vol. 1, no. 2, pp. 133–142, 2015.

[2] UK Department of Energy and Climate Change, “Updated energy and emissions projections 2013,” *Energy White Pap.*, vol. 947, no. November, pp. 1–51, 2008.

[3] UNFCCC, “Paris Agreement,” *Conf. Parties its twenty-first Sess.*, no. December, p. 32, 2015.

[4] K. Tsukagoshi, J. Masada, A. Muyama, Y. Iwasaki, and E. Ito, “Operating Status of Uprating Gas Turbines and Future Trend of Gas Turbine Development,” *Mitsubishi Heavy Ind. Ltd. Tech. Rev.*, vol. 44, no. 4, pp. 1–6, 2007.

[5] L. Brooking, J. Sumner, S. Gray, J. R. Nicholls, G. Marchant, and N. J. Simms, “Effect of Stress State and Simultaneous Hot Corrosion on the Crack Propagation and Fatigue Life of Single Crystal Superalloy CMSX-4,” *Int. J. Fatigue*, 2018.

[6] H. Rosier, K. Perkins, A. Girling, J. Leggett, and G. Gibson, “Factors affecting the corrosion fatigue life in nickel based superalloys for disc applications,” *MATEC Web Conf.*, vol. 14, p. 03001, 2014.

[7] R. Hashizume, A. Yoshinari, T. Kiyono, and M. Morinaga, “Development of Ni-Based Single Crystal Superalloys for Power-Generation Gas Turbines,” *Superalloys 2004 (Tenth Int. Symp.*, pp. 53–62, 2004.

[8] R. C. Reed, “The Superalloys, Fundamentals and Applications,” in *The Superalloys*, 2006, p. various.

[9] H. Long, S. Mao, Y. Liu, Z. Zhang, and X. Han, “Microstructural and compositional design of Ni-based single crystalline superalloys — A review,” *J. Alloys Compd.*, vol. 743, pp. 203–220, 2018.

[10] W. Ren, C. Niu, B. Ding, Y. Zhong, J. Yu, Z. Ren, W. Liu, L. Ren, and P. K. Liaw, “Improvement in creep life of a nickel-based single-crystal superalloy via composition homogeneity on the multiscales by magnetic-field-assisted directional solidification,” *Sci. Rep.*, vol. 8, no. 1, pp. 1–17, 2018.

[11] D. Siebörger, H. Knake, and U. Glatzel, “Temperature dependence of the elastic moduli of the nickel-base superalloy CMSX-4 and its isolated phases,” *Mater. Sci. Eng. A*, vol. 298, no. 1–2, pp. 26–33, 2001.

[12] V. Sass, U. Glatzel, and M. Feller-Kniepmeier, “Anisotropic creep properties of the nickel-base superalloy CMSX-4,” *Acta Mater.*, vol. 44, no. 5, pp. 1967–1977, 1996.

[13] A. B. Parsa, P. Wollgramm, H. Buck, C. Somsen, A. Kostka, I. Povstugar, P. P. Choi, D. Raabe, A. Dlouhy, J. Müller, E. Spiecker, K. Demtroder, J. Schreuer, K. Neuking, and G. Eggeler, “Advanced scale bridging microstructure analysis of single crystal Ni-base superalloys,” *Adv. Eng. Mater.*, vol. 17, no. 2, pp. 216–230, 2015.

[14] B. Dubiel, P. Indyka, I. Kalemba-Rec, and T. Moskalewicz, “Analytical Electron Microscopy Studies of the CMSX-4 Single Crystal Superalloy Subjected to High Temperature Annealing,” *Acta Phys. Pol. A*, vol. 131, no. 5, pp. 1375–1379, 2017.

[15] H. L. Cockings, K. M. Perkins, and M. Dowd, “Influence of environmental factors on the corrosion-fatigue response of a nickel-based superalloy,” *Mater. Sci. Technol. (United Kingdom)*, vol. 33, no. 9, pp. 1048–1055, 2017.

[16] G. S. Mahobia, N. Paulose, S. L. Mannan, R. G. Sudhakar, K. Chattopadhyay, N. C. Santhi Srinivas, and V. Singh, “Effect of hot corrosion on low cycle fatigue behavior of superalloy IN718,” *Int. J. Fatigue*, vol. 59, pp. 272–281, 2014.

[17] N. Chapman, L. Brooking, J. Sumner, S. Gray, and J. Nicholls, “Corrosion fatigue testing: the combined effect of stress and high temperature corrosion,” *Mater. High Temp.*, vol. 35, no. 1–3, 2018.

[18] K. S. Chan, M. P. Enright, and J. P. Moody, “Development of a Probabilistic Methodology for Predicting Hot Corrosion Fatigue Crack Growth Life of Gas Turbine Engine Disks,” *J. Eng. Gas Turbines Power*, vol. 136, no. 2, p. 022505, 2014.

[19] T. P. Gabb, J. Telesman, B. Hazel, and D. P. Mourer, “The effects of hot corrosion pits on the fatigue resistance of a disk superalloy,” *J. Mater. Eng. Perform.*, vol. 19, no. 1, pp. 77–89, 2010.

[20] D. J. Child, J. Meldrum, and P. Onwuarolu, “Corrosion-fatigue testing of Ni-based superalloy RR1000,” *Mater. Sci. Technol. (United Kingdom)*, vol. 33, no. 9, pp. 1040–1047, 2017.

[21] L. Brooking, J. Sumner, S. Gray, and N. J. Simms, “Stress corrosion of Ni-based superalloys,” *Mater. High Temp.*, vol. 35, no. December, pp. 120–129, 2017.

[22] J. L. W. Carter, N. Zhou, J. M. Sosa, P. A. Shade, A. L. Pilchak, W. M. Kuper, Y. Wang, H. L. Fraser, M. D. Uchic, and M. J. Mills, “Characterization of strain accumulation at grain boundaries of nickel based superalloys,” *Superalloys 2012*, no. January, pp. 43–52, 2012.

[23] B. Rengara, S. Baba, and M. Okazaki, “Influence of Crystal Orientation on Cyclic Sliding Friction and Fretting Fatigue Behavior of Single Crystal Ni-Base Superalloys,” in *Superalloys 2016: Proceedings of the 13th International Symposium on Superalloys*, 2016, pp. 395–404.

[24] V. Sass, U. Glatzel, and M. Feller-Kniepmeier, “Creep anisotropy in the monocrystalline nickel-base superalloy CMSX-4,” *Superalloys 1996 8th Int. Symp. Superalloys.*, pp. 283–290, 1996.

[25] R. N. Parkins, “Mechanisms of Stress-corrosion Cracking,” *Corros. Third Ed.*, vol. 1, no. Ref 1, p. 8:3-8:31, 2013.

[26] J. R. Donahue, A. B. Lass, and J. T. Burns, “The interaction of corrosion fatigue and stress-corrosion cracking in a precipitation-hardened martensitic stainless steel,” *npj Mater. Degrad.*, vol. 1, no. 1, p. 11, 2017.

[27] N. S. Zadorozne, M. C. Giordano, A. E. Ares, R. M. Carranza, and R. B. Rebak, “Anodic

characteristics and stress corrosion cracking behavior of nickel rich alloys in bicarbonate and buffer solutions," *Corros. Sci.*, vol. 108, pp. 1–10, 2016.

[28] L. J. Qiao, K. W. Gao, A. A. Volinsky, and X. Y. Li, "Discontinuous surface cracks during stress corrosion cracking of stainless steel single crystal," *Corros. Sci.*, vol. 53, no. 11, pp. 3509–3514, 2011.

[29] M. Ahlers and E. Riecke, "Stress corrosion cracking in single crystals of Fe-25Cr-20Ni," *Corros. Sci.*, vol. 18, no. 1, pp. 21–38, 1978.

[30] E. I. Meletis and R. F. Hochman, "The crystallography of stress corrosion cracking in face centered cubic single crystals," *Corros. Sci.*, vol. 24, no. 10, pp. 843–862, 1984.

[31] W. Carpenter, B. S.-J. Kang, and K. M. Chang, "SAGBO Mechanism on High Temperature of Ni-base Superalloys Cracking Behavior," *Miner. Met. Mater. Soc.*, pp. 679–688, 1997.

[32] X. Liu, L. Ma, and K. Chang, "Time-dependent crack growth behaviors of five superalloys," *Miner. Met. Mater. Soc.*, pp. 543–552, 2001.

[33] A. A. N. Németh, D. J. Crudden, D. E. J. Armstrong, D. M. Collins, K. Li, A. J. Wilkinson, C. R. M. Grovenor, and R. C. Reed, "Environmentally-assisted grain boundary attack as a mechanism of embrittlement in a nickel-based superalloy," *Acta Mater.*, vol. 126, pp. 361–371, 2017.

[34] M. Gao, D. J. Dwyer, and R. P. Wei, "Chemical and Microstructural Aspects of Creep Crack Growth in Inconel 718 Alloy," *Superalloys 718, 625, 706 Var. Deriv.*, pp. 581–592, 1994.

[35] D. A. Woodford, "Gas phase embrittlement and time dependent cracking of nickel based superalloys," *Energy Mater.*, vol. 1, no. 1, pp. 59–79, 2006.

[36] J. P. Beckman and D. A. Woodford, "Gas phase embrittlement of nickel by sulfur," *Metall. Trans. A*, vol. 21, no. 12, pp. 3049–3061, 1990.

[37] M. C. Rezende, L. S. Araujo, S. B. Gabriel, D. S. dos Santos, and L. H. de Almeida, "Hydrogen embrittlement in nickel-based superalloy 718: Relationship between g' þ g 00 precipitation and the fracture mode," *Int. J. Hydrogen Energy*, vol. 40, no. 47, pp. 17075–17083, 2015.

[38] P. D. Hicks and C. J. Altstetter, "Comparison of Internal Hydrogen Embrittlement of Superalloys 718 and 625," *Superalloys 718, 625 Var. Deriv.*, pp. 635–651, 1991.

[39] Z. Ahmad, "Types of corrosion: materials and environments," in *Principles of Corrosion Engineering and Corrosion Control*, 2006, pp. 120–270.

[40] C. Duret-Thual, "Understanding corrosion: Basic principles," in *Understanding Biocorrosion: Fundamentals and Applications*, 2014, pp. 3–32.

[41] S. Lynch, "PROGRESS TOWARDS UNDERSTANDING MECHANISMS OF HYDROGEN EMBRITTLEMENT AND STRESS CORROSION CRACKING," *NACE Int. Corros. Conf.*, no. 07493, pp. 1–29, 2007.

[42] H. K. Birnbaum, "MECHANISMS OF HYDROGEN RELATED FRACTURE OF METALS," 1989.

[43] J. Li, A. Oudriss, A. Metsue, J. Bouhattate, and X. Feaugas, “Anisotropy of hydrogen diffusion in nickel single crystals: The effects of self-stress and hydrogen concentration on diffusion,” *Sci. Rep.*, vol. 7, no. February, pp. 1–9, 2017.

[44] H. Vehoff and W. Rothe, “OVERVIEW IN GASEOUS HYDROGEN EMBRITTLEMENT FeSi- AND Ni-SINGLE CRYSTALS,” vol. 31, no. 11, pp. 1781–1793, 1983.

[45] A. Zahs, M. Spiegel, and H. J. Grabke, “Chloridation and oxidation of iron, chromium, nickel and their alloys in chloridizing and oxidizing atmospheres at 400-700°C,” *Corros. Sci.*, vol. 42, pp. 1093–1122, 2000.

[46] K. L. Luthra and O. H. LeBlanc, “Low Temperature Hot Corrosion of Co-Cr-Al Alloys*,” *Mater. Sci. Eng.*, vol. 87, pp. 329–335, 1987.

[47] V. Mannava, A. S. Rao, N. Paulose, M. Kamaraj, and R. S. Kottada, “Hot corrosion studies on Ni-base superalloy at 650 °C under marine-like environment conditions using three salt mixture (Na2SO4+ NaCl + NaVO3),” *Corros. Sci.*, vol. 105, pp. 109–119, 2016.

[48] N. Birks, G. H. Meier, and F. S. Pettit, “High-Temperature Corrosion Resistance,” *JOM*, vol. 39, no. 12, pp. 28–31, 1987.

[49] N. Eliaz, G. Shemesh, and R. M. Latanision, “Hot corrosion in gas turbine components,” *Eng. Fail. Anal.*, vol. 9, no. 1, pp. 31–43, 2002.

[50] D. A. Shifler, “Hot corrosion: a modification of reactants causing degradation,” *Mater. High Temp.*, vol. 35, no. 1–3, pp. 225–235, 2018.

[51] P. Lortrakul, R. W. Trice, K. P. Trumble, and M. A. Dayananda, “Investigation of the mechanisms of Type-II hot corrosion of superalloy CMSX-4,” *Corros. Sci.*, vol. 80, pp. 408–415, 2014.

[52] B. A. Pint, S. Dryepondt, and K. A. Unocic, “Oxidation of superalloys in extreme environments,” *7th Int. Symp. Superalloy 718 Deriv.*, pp. 861–875, 2010.

[53] R. A. Rapp, “Chemistry and electrochemistry of hot corrosion of metals,” *Mater. Sci. Eng.*, vol. 87, no. C, pp. 319–327, 1987.

[54] W. Gao and Z. Li, *Developments in high-temperature corrosion and protection of materials*. 2008.

[55] J. W. Morris, “Chapter 4 : Defects in Crystals,” *Mater. Sci.*, pp. 76–107, 2007.

[56] F. Farhad, X. Zhang, and D. Smyth-Boyle, “Fatigue behaviour of corrosion pits in X65 steel pipelines,” *Proc. Inst. Mech. Eng. Part C J. Mech. Eng. Sci.*, vol. 0, no. 0, pp. 1–12, 2018.

[57] E. M. Gutman, G. Solovioff, and D. Eliezer, “The mechanochemical behavior of type 316L stainless steel,” *Corros. Sci.*, vol. 38, no. 7, pp. 1141–1145, Jul. 1996.

[58] British Standards Institutions, “BSI Standards Publication Plastics — Determination of flexural properties,” 2013.

[59] J. Sumner, A. Encinas-Oropesa, N. Simms, and J. R. Nicholls, “Type II hot corrosion: Behaviour of CMSX-4 and IN738LC as a function of corrosion environment,” *Mater.*

Corros., no. 2, pp. 188–196, 2014.

[60] J. M. Sanchez, J. R. Barefoot, R.N. Jarrett and J. K. Tien, "Modelling of γ/γ' phase equilibrium in the nickel-aluminium system," *Acta Metall* vol. 32, No. 9, pp 1519-1525, 1984.

[61] E. A. Brandes and G. B.Brooks (Eds.), *Smithells Metals Reference Book*, 7th Edition, (Butterworth-Heinemann: Oxford), 1992.

[62] C. Booth-Morrison, Z. Mao, R. D. Noebe and D. N. Seidman, "Chromium and tantalum site substitution patterns in Ni_3Al ($L1_2$) γ' precipitates," *Applied Physics Letters,* vol. 93, pp 033103-1 - 033103-3, 2008.

[63] Y. Tu, Z. Mao and D. N. Seidman, "Phase partitioning and site-substitution patterns of molybdenum in a model Ni-Al-Mo superalloy: An atom probe tomographic and first-principles study," *Applied Physics Letters,* vol. 101, pp 121910-1 - 121910-3, 2012.

[64] C. D. Sudbrack, T. D. Ziebell, R. D. Noebe and D. N. Seidman, "Effects of a tungsten addition on the morphological evolution, spatial correlations and temporal evolution of a model Ni-Al-Cr superalloy," *Acta Materialia,* vol. 56, pp 448-463, 2008.

[65] Y. Amouyal, Z. Mao, C. Booth-Morrison and D. N. Seidman, "On the interplay between tungsten and tantalum atoms in Ni-based superalloys: An atom probe tomographic and first-principles study," *Applied Physics Letters,* vol. 94, pp 041917-1 - 041917-3, 2009.

[66] Y. Amouyal, Z. Mao, and D. N. Seidman, "Effects of a tantalum on the partitioning of tungsten between the γ- and γ'- phases in nickel-based superalloys: Linking experimental and computational approaches," *Acta Materialia,* vol. 58, pp. 5898-5911, 2010.

[67] R.A. MacKay, M. V. Nathal and D. D. Pearson, "Influence of molybdenum on the creep properties of nickel-base superalloy single crystals," *Metall. Trans. A,* vol. 21 pp. 381-388, 1990.

[68] R Jayaram, J. I. Hren and M. K. Miller, "APFIM/TEM characterization of solute partitioning in a model Ni-Mo-Al-Ta superalloy," *Surface Science,* vol. 246, pp. 323-328, 1991.

[69] H. Mughrabi and U. Tetzlaff, "Microstructure and high-temperature strength of monocrystalline nickel-base superalloys," *Advanced Engineering Materials,* vol. 2 No. 6 , pp. 319-326, 2000.

[70] J. Svoboda and P Lukas, " Model of creep in <100> - oriented superalloy single crystals," Acta Mater. vol. 46, no. 10, pp. 3421-3431, 1998.

[71] A. K. Jena and M.C. Chaturvedi, "The role of alloying elements in the design of nickel-base superalloys," J. Mat. Sci., vol. 19, pp. 3121-3139, 1984.

6. Paper 5: Corrosion fatigue testing: the combined effect of stress and high temperature corrosion

Neil Chapman[1 and 2], Laurie Brooking[2], Joy Sumner[2], Simon Gray[2] and John Nicholls[2]

[1] Siemens Industrial Turbomachinery Ltd, Ruston House, PO Box 1, Waterside South, Lincoln, LN5 7FD

[2] Cranfield University, College Road, Cranfield, MK43 0AL

Abstract. A corrosive environment can have a detrimental effect on the fatigue life of a material due to a change in failure mechanism. Attempts have been made to replicate this change on nickel-base superalloy CMSX-4 cast in the <001> orientation. Fatigue testing in air, of this material typically produces a fracture on an angle of approximately 55° which is consistent with the fracture having propagated on a {111} slip plane. The aim of the research was to fatigue test in a corrosive environment with the purpose of producing a crack/fracture which deviated from the typical angle and thus confirm that the corrosive environment had affected the fatigue mechanism. It was concluded that the change in mechanism to high temperature corrosion fatigue was associated with a reduced load application rate together with precorroding the test specimens to trigger the initiation of the corrosion fatigue mechanism.

Keywords: corrosion fatigue, waveform, load application rate, precorrosion

6.1. Introduction

Materials which are used in rotating parts of industrial gas turbines (IGTs) are subjected to harsh operating conditions which include high stresses and temperatures. In addition, an IGT may operate in a number of different atmospheres such as: industrial, marine or rural, all of which are likely to contain different impurities in the air that may cause corrosion issues[1].

Nickel-base superalloys are routinely used in IGTs due to their high temperature mechanical properties [1][2] and their development has included improvements in their resistance to corrosion attack. This has been achieved by including chromium and aluminium in the chemistries with the purpose of growing either a protective chromia or alumina scale. The superalloys may therefore be classed as either a chromia or an alumina former [1][2], depending on the alloy composition.

Chromia formers tend to be used at temperatures below 900°C due to chromia forming volatile species above this temperature, whilst alumina formers are used above 900°C since less protective scales are formed below this temperature [1]. IGT components though do not generally experience a uniform temperature and different sections of the same component may experience temperatures above and below 900°C. The nickel-base superalloy CMSX-4 is an alumina former [1] and thermal exposure tests on this material, conducted at 700°C,

revealed the primary scale observed was a thin aluminium rich layer. Due to the instability of the protective alpha alumina phase at this temperature, the scale was attributed as being either a less protective transient Al_2O_3 phase or a mixed oxide of Al/Cr [3].

Nickel-base superalloys, even when they have grown a protective scale, are not immune to corrosion attack though and under certain conditions the attack may result in high rates of material loss. One form of corrosion that can result in pitting and rapid material loss is type II hot corrosion [1][2][3]. This form of corrosion tends to occur between the temperatures of 600 to 800°C[1] and requires the presence of deposits such as sulphates and SO_3 [1][2], within the gas phase.

There are two stages to type II hot corrosion: incubation and propagation. Once the attack has penetrated any protective scale (considered the end of the incubation stage), the attack will enter the propagation stage of corrosion and the superalloy itself will be attacked resulting in high rates of material loss [3]. These rates though, may alter with exposure time as was found from type II hot corrosion tests that were performed on CMSX-4 material [3]. During these tests, the propagation rates fell with exposure time which was thought to be most likely due to thick deposits/corrosion product scale that had formed inhibiting the supply of the corrosive species to the material/scale interface [3].

Any reduction in cross section caused by the corrosion attack will effectively increase the stresses acting on the IGT components and the rate of loading/straining may also have an effect on the fatigue life of the material. Classically, a series of fatigue tests are performed to evaluate an S-N curve which can be used to determine the fatigue life of a material for a specific set of conditions such as: temperature, environment and R-ratio. Figure 6.1 shows an example of an S-N curve which may be made up of up to three different regions. In region I, the tests are performed at stresses at or above the materials' yield strength and hence the material behaves in an elasto-plastic manner. In region II, the material is stressed below the yield strength and so behaves in an elastic manner. Region III defines an unlimited life but materials with a face centred cubic structure, such as nickel, do not seem to experience this region [4].

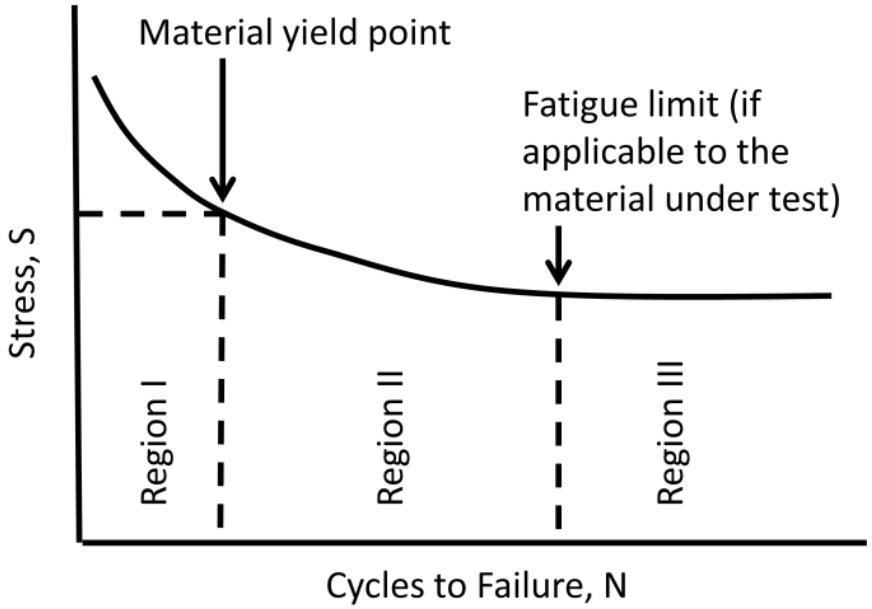

Figure 6.1: Example of S-N curve showing different regions

Fatigue tests may be performed in strain or load control and generally, strain control is used for the elasto-plastic region of fatigue testing where the associated strain is the summation of elastic and plastic strains. Load control tends to be used in the elastic region of fatigue testing where a one-to-one correspondence between stress and strain exists. It is therefore unimportant whether fatigue testing in the elastic region is conducted using strain or load control [4].

For a given total strain, reducing the strain rate may result in shorter fatigue lives when the tests are conducted in the elasto-plastic region of fatigue testing. This effect was observed on tests performed at elevated temperatures on nickel-base alloy 718 in air[5]. The tests were also performed with only elastic loading which gave no noticeable interaction between life and strain rate [5]. The most likely cause is an interaction between creep and fatigue at the elevated temperatures, however, no hypothesis was ventured by the author[5] as to a possible mechanism that may be responsible for this behaviour.

A molecular dynamic simulation of monocrystalline nickel indicated the strain rate effect may be explained by a mechanism involving microstructural changes in the form of dislocations being generated at the crack tip at temperature. The simulations showed that when a set strain level was reached with different strain rates, the faster strain rates produced slower growing cracks that tended to propagate in a ductile manner with dislocations generated at the crack tip. This had the effect of blunting the crack tip and produced relatively low peak stress levels at the tip of the crack. The slower strain rates though produced faster propagating cracks which behaved in a more brittle manner and induced fewer dislocations at the crack tip resulting in greater peak stress values at the tip of the crack [6]. These peak stress values are highly localised and upon repeated cycling, form micro-cracks and a plastic zone ahead of the advancing crack tip [7].

During the growth of a corrosion fatigue crack, it is reported that it is necessary for the corrosive compound to be supplied to the crack tip, interact with newly exposed crack surface by adsorption and diffusion, and finally the reacted products on the crack surfaces need to be

removed in order to prevent a build up at the crack tip which may influence local stresses [8]. An important factor then, is the rate at which the corrosive compound reaches the crack tip and slowing down the frequency of the fatigue testing should allow more time for this to happen. It has also been commented that frequencies below 1 Hz have the greatest environmental effect on the fatigue properties of nickel-based superalloys [9].

Slowing the frequency of the fatigue tests down can be achieved by increasing the duration of the entire selected waveform or selected periods of the waveform which include the stress or strain (depending on whether the fatigue test is performed in load or strain control) application time, the maximum stress/strain hold time, the stress/strain decreasing time and the minimum stress/strain hold. Fatigue tests, performed on a low carbon alloy steel in an aqueous solution of 3% NaCl at a temperature of 25°C, led to the conclusion that of all the periods of a waveform, lengthening the stress application period up to 10 seconds had the greatest environmental effect and was attributed to corrosive dissolution on fresh crack surfaces that were formed during that period of the waveform [10]. One premise to be examined is whether this observation applies to high temperature corrosion fatigue.

The aim of the current work was to perform corrosion fatigue tests in service like-type II hot corrosion conditions on the face centred cubic single crystal nickel-based superalloy CMSX-4 that had been cast in the <001> orientation. The purpose of the corrosion fatigue tests was to establish parameters that would allow sufficient time for the corrosive compounds to affect the fatigue mechanism. The parameters under evaluation were the various periods of a trapezoidal waveform (Figure 6.2) and whether or not to precorrode the test specimens. Typically, fatigue tests conducted in air on this material and orientation produce fracture surfaces on approximate angles of 55° in relation to the axial {001} plane, which is consistent with the fracture having propagated on a {111} slip plane. Deviation from this typical angle would therefore be strongly suggestive that the environment had affected the fatigue mechanism of the material.

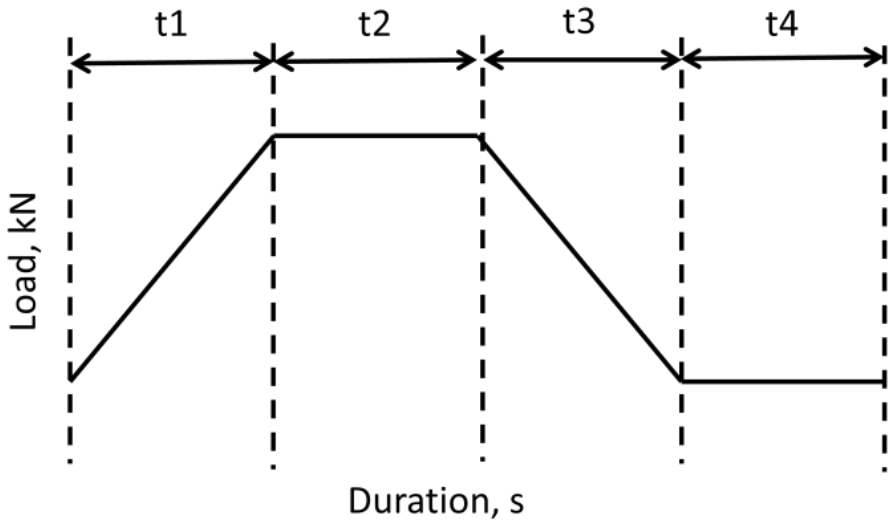

Figure 6.2: Various periods of the trapezoidal waveform, where in t1 the load increases, in t2 the maximum load is held, in t3 the load decreases and in t4 the minimum load is held. The trapezoidal waveform is written in the form: t1-t2-t3-t4

6.2. Experimental methods

The material under investigation was the superalloy CMSX-4 that had been solution treated and precipitation hardened but had not been hot isostatic pressed. The nominal composition of this superalloy is shown in table 6.1. After casting, this material typically contains significant segregation, γ/γ' eutectic regions and pores [11]. The solution heat treatment is therefore carried out in order to achieve a balanced chemical composition and dissolve the eutectic regions but this is at the expense of increased levels of porosity [11]. The precipitation hardening then provides the material with the desirable mechanical properties which makes it suitable for use as IGT components.

Table 6.1: Chemical composition of CMSX-4 in weight percentage (wt-%)

Alloy	Ni	Cr	Co	Mo	W	Al	Ti	Ta	Hf	Re
Wt-%	61.7	6.5	9	0.6	6	5.6	1	6.5	0.1	3

Plain fatigue test specimens with a gauge diameter of 6 mm (Figure 6.3) were machined from bars that were cast in the <001> orientation and tested on an axial fatigue testing machine in load control at a temperature of 550°C. Due to the flexibility in controlling the various periods of applying the load, the trapezoidal waveform was selected. This waveform is expressed in terms of the duration of each respective period. For example, a 1-1-1-1 s waveform describes a 1 second load increasing period with1 second at maximum load hold followed by 1 second with the load decreasing and finally 1 second at the minimum load hold period.

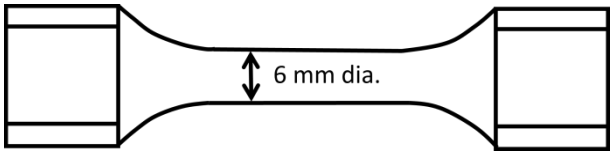

Figure 6.3: Schematic of plain fatigue test specimen

The fatigue testing atmosphere was either laboratory air or 300 ppm SO_2 in air (flow rate between 25 and 50 SCCM, preheated to the test temperature). The test specimens were loaded into the fatigue machine in such a manner so that they sat within a gas sheath within the induction coil that was used for attaining the test temperature. The gas sheath ensured the corrosive gas used in the corrosion fatigue tests, flowed over the surfaces of the test specimen. The tests were only started after the test temperature had been achieved and left for 15 minutes to ensure the temperature had equalised throughout the cross section of the test specimen. Type K thermocouples were used for measuring the test temperature.

The maximum and minimum stress levels used were the same for all of the fatigue and corrosion fatigue tests which were 800 and 0 MPa respectively. This ensured that all the tests were conducted in the elastic region of fatigue testing. Table 6.2 summarises the conditions of the fatigue tests conducted.

Table 6.2: Test conditions for the fatigue tests conducted

Environment	Waveform parameters (s)	Precorroded test specimen	Number of re-salts required
Laboratory air	1-1-1-1	No	…
Corrosive	1-1-1-1	No	0
Corrosive	1-1-1-1	Yes	0
Laboratory air	10-1-1-1	No	…
Corrosive	10-1-1-1	No	1
Corrosive	10-1-1-1	Yes	0
Laboratory air	10-1-1-1	Yes	…
Corrosive	1-10-1-1	No	2

The fatigue testing performed in laboratory air included the waveforms: 1-1-1-1 and 10-1-1-1 s. No salts were applied to either of these test specimens. These can be considered as baseline tests.

Corrosion fatigue testing performed in the SO_x environment on non-precorroded test specimens included the waveforms: 1-1-1-1, 10-1-1-1 and 1-10-1-1 s. For these tests, the test specimens were sprayed evenly around the surfaces between the threads with 0.114 mg cm^{-2} with an 80/20 mol% mix of $(Na/K)_2SO_4$ salt deposits before the testing began. Applying a specific quantity of salt though, implies that the flux may vary for the different corrosion fatigue tests depending on when the test specimen fails. The method for applying the salts, which were dissolved in water, involved heating the specimens up to approximately 200°C after which the salts were sprayed onto the hot surfaces. The heat caused the water to flash evaporate leaving the salts on the sprayed surfaces. If a corrosion fatigue test completed 100 hours without failing, the test was stopped and a further 0.114 mg cm^{-2} of salt was applied before the test was re-started.

The corrosion fatigue testing performed in the SO_x environment on precorroded test specimens included the waveforms: 1-1-1-1 and 10-1-1-1 s. The precorrosion of these test specimens involved evenly spraying the 80/20 mol% mix of $(Na/K)_2SO_4$ salts onto the surfaces between the threads, using the same methodology as described previously, with a flux rate of 5 µg cm^{-2} h^{-1}. That is, the salts were sprayed after 0, 100, 200, 300 and 400 hours of thermal exposure, at the same temperature as the fatigue tests, and the total duration of the thermal exposures were 500 hours. If any corrosion fatigue test using the precorroded test specimens completed 100 hours without failing, the test was stopped and a further 0.114 mg cm^{-2} of salt deposits was applied before the test was re-started.

A fatigue test in laboratory air using a 10-1-1-1 s waveform was also performed on a precorroded test specimen that had all of the salts washed off. The purpose of this test was to determine whether corrosion pitting alone was enough to alter the fatigue mechanism or if the corrosive salts and environment were required throughout the test.

As part of an initial test program to identify parameters which affected the fatigue mechanism, only one test was conducted for each test condition with the exception of the corrosion fatigue test conducted with a 1-10-1-1 s waveform and a non-precorroded specimen. A repeat of this test was performed.

The number of tests conducted is acknowledged as being small and the cycles to failure data would be subject to any potential scatter involved. For this reason, the cycles to failure data was not used for assessing whether the fatigue mechanism had been affected but is included in this article in a normalised form for reference purposes only (Table 6.3). Instead, the assessment was based on visual observations of the crack/fracture paths/angles. These visual observations were conducted with the naked eye, a low powered optical microscope and an SEM. Of particular interest was whether any of the test conditions had produced crack surfaces which deviated away from the typical 55° angle. If cracks had deviated away from this angle, EDX analysis using a series of rectangular region X-ray acquisitions on the crack surface was performed to determine which corrosive element(s) had contributed to the deviation. Microsections were then taken and the resulting cross sections viewed using a high powered optical microscope and SEM.

6.3. Results and discussion

Table 6.3 shows a summary of the fatigue and corrosion fatigue tests which did and did not result in a crack/fracture that deviated from the 55° angle.

Table 6.3: Results of fatigue and corrosion fatigue tests

Environment	Waveform parameters (s)	Pre-corroded test specimen	Normalised cyclic data	Normalised hours data	Deviation of crack/fracture facets from 55° angle?
Laboratory air	1-1-1-1	No	1.0	1.0	No
Corrosive	1-1-1-1	No	1.4	1.4	No
Corrosive	1-1-1-1	Yes	0.9	0.9	Yes
Laboratory air	10-1-1-1	No	1.3	4.1	No
Corrosive	10-1-1-1	No	0.8	2.6	Yes
Corrosive	10-1-1-1	Yes	0.3	1.0	Yes
Laboratory air	10-1-1-1	Yes	1.6*	5.2*	…
Corrosive	1-10-1-1	No	1.6	5.2	No

Where:

* indicates test specimen did not fail and considered a runout

Normalised data is expressed as a factor of the Laboratory air 1-1-1-1 s test

Both of the non-precorroded test specimens that were fatigue tested in laboratory air showed crack/fracture features on angles of approximately 55°. This crack/fracture angle is shown in figure 6.4 which was produced using the 10-1-1-1 s waveform. This is consistent with typical results and indicates that the different stress application rates of 800 MPa s^{-1} and 80 MPa s^{-1}, associated with the respective 1-1-1-1 and 10-1-1-1 s waveforms could not be wholly responsible for any crack/fracture deviation that was subsequently found on the corrosion fatigue test specimens.

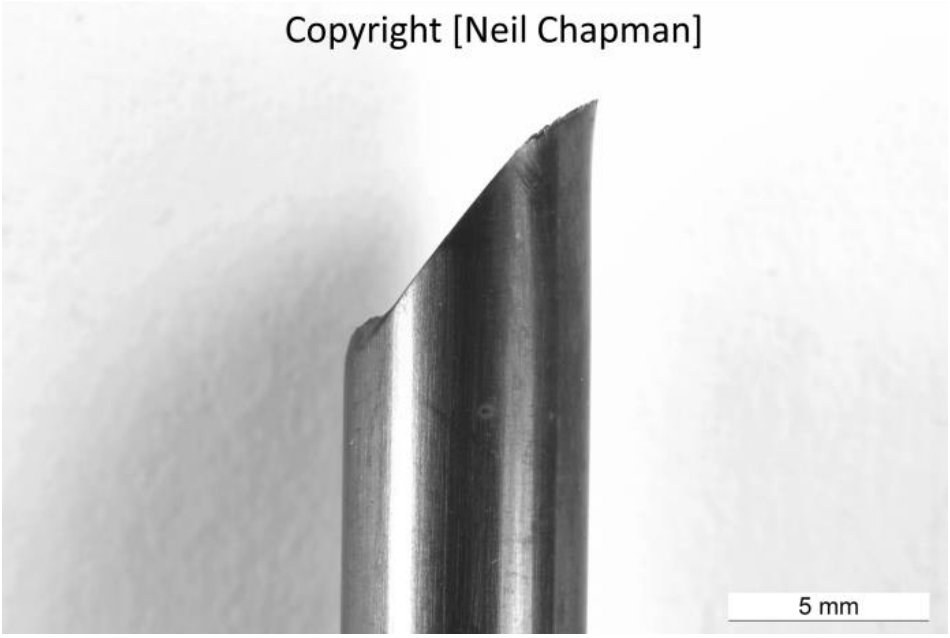

Figure 6.4: Low powered optical microscope image of fractured test specimen showing the typical 55° crack/fracture angle produced from fatigue testing in air using the 10-1-1-1 s waveform and non-precorroded test specimen

The non-precorroded test specimens that were subjected to the corrosion fatigue tests using the 1-1-1-1 and 1-10-1-1 s waveforms, also produced fracture facets that were only on approximate angles of 55°. A repeat of 1-10-1-1 s test was performed and exceeded the duration of the original test by a factor of 1.5 without failing. The repeat test was therefore considered a runout and did not provide any data regarding crack/fracture angles. However, the non-precorroded corrosion fatigue test using the 10-1-1-1 s waveform produced a crack that was initially flat and perpendicular to the surface of the specimen before transitioning to the 55° angle (Figure 6.5). The perpendicular crack, which was in the shape of a thumbnail with approximate maximum width and depth dimensions of 2.0 and 1.5 mm respectively, also exhibited beach marks (Figure 6.6) which were suggestive that the crack was growing as a start-stop-start event. importance and lowering this has the effect of decreasing the frequency providing the other periods of the waveform remain constant.

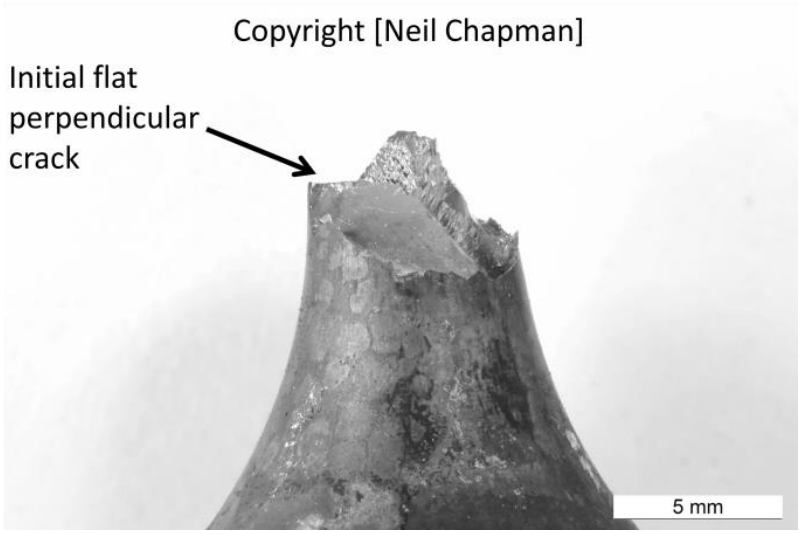

Figure 6.5: Low powered optical microscope image of fractured test specimen showing deviation from the typical 55° crack/fracture angle produced from corrosion fatigue testing using the 10-1-1-1 s waveform and non-precorroded test specimen

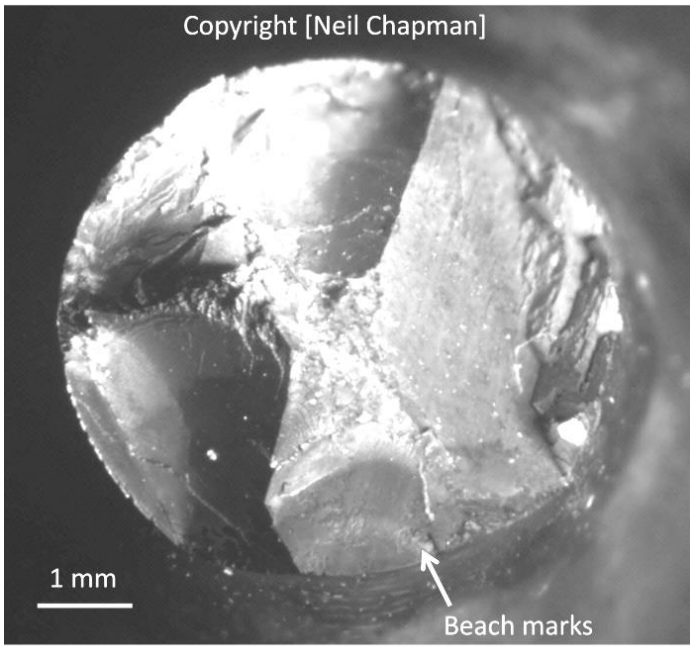

Figure 6.6: Low powered optical microscope image of beach marks observed on the initial flat perpendicular crack from the corrosion fatigue test using the 10-1-1-1 s waveform and non-precorroded test specimen

EDX analysis (Figure 6.7a and 6.7b) of the crack surface indicated sulphur was the main element present, in decreasing amounts, from the surface of the test specimen to the tip of the perpendicular crack. Small quantities of sodium were also present and again displayed a generally decreasing trend from the surface to the perpendicular crack tip. Potassium though was only present in trace amounts. After the EDX analysis, the test specimen was sectioned and this revealed the corrosion product on the perpendicular crack was very thin with an approximate thickness of 0.2 µm at the mid crack position (Figure 6.8). These corrosion fatigue tests have indicated, based on the 10-1-1-1 and 1-10-1-1s waveforms which have the

same frequency, that frequency or the maximum load hold time are not prime factors which allow the environment time to affect the fatigue mechanism. Instead, the load application rate appears to be of greater.

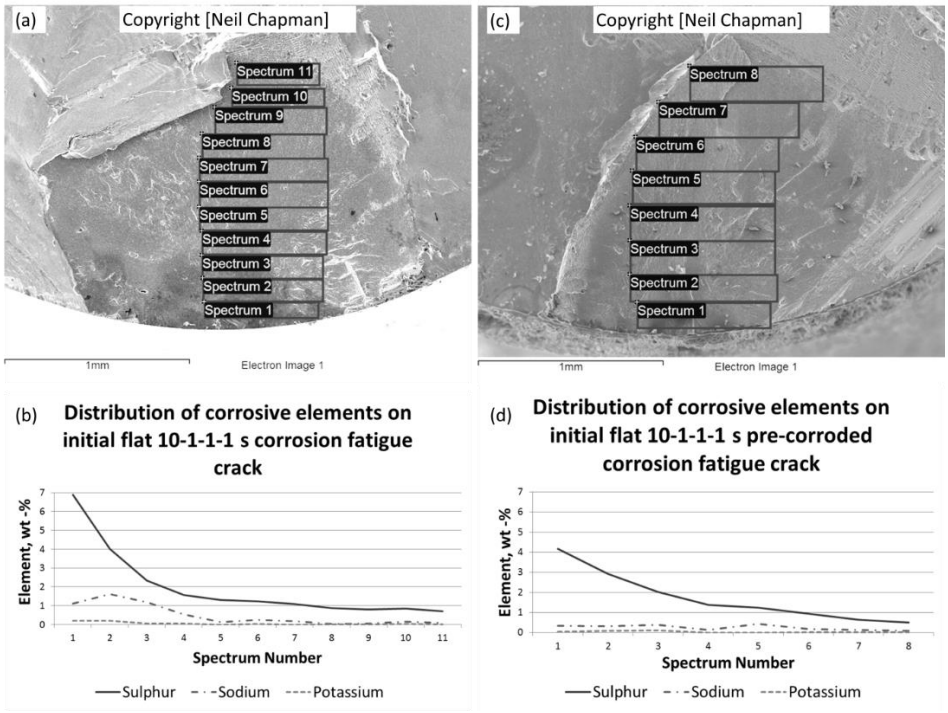

Figure 6.7: (a) SEM image showing locations of X-ray acquisition regions for EDX analysis line plots (b) obtained from the initial flat perpendicular crack from the corrosion fatigue test using the 10-1-1-1 s waveform and non-precorroded test specimen. (c) SEM image showing locations of X-ray acquisition regions for EDX analysis line plots (d) obtained from the initial flat perpendicular crack from the corrosion fatigue test using the 10-1-1-1 s waveform precorroded test specimen

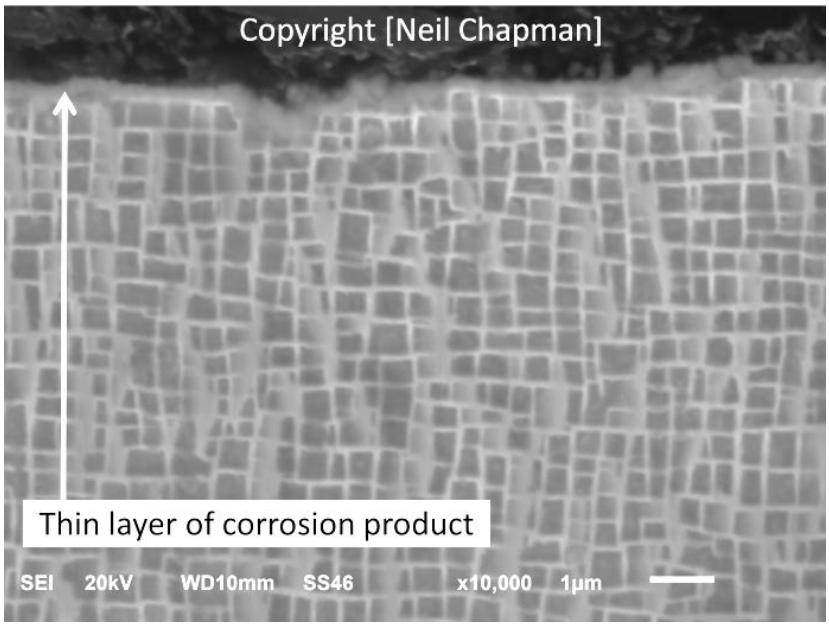

Figure 6.8: SEM image of microsection showing thin layer of corrosion product at mid crack position on the initial flat perpendicular crack from the corrosion fatigue test using the 10-1-1-1 s waveform and non-precorroded test specimen

Precorroding the test specimens before conducting the corrosion fatigue tests with the 1-1-1-1 and 10-1-1-1 s waveforms also produced initial flat thumbnail shaped perpendicular cracks that exhibited beach marks before transitioning to an approximate 55° angle. EDX analysis of the 10-1-1-1 s crack (Figure 6.7c and 6.7d) showed a similar pattern to that observed on the non-precorroded test specimen used on the corrosion fatigue 10-1-1-1 s test in that sulphur and sodium were present in decreasing amounts from the surface of the specimen to the crack tip with the main element being sulphur. The approximate maximum width and depth dimensions of the perpendicular crack for the precorroded 1-1-1-1 s corrosion fatigue test were measured at 1.0 and 0.9 mm respectively. The width and depth dimensions of the initial perpendicular crack on the precorroded 10-1-1-1 s corrosion fatigue test specimen were 3.6 and 2.0 mm respectively. It was also observed that the precorroded 10-1-1-1 s corrosion fatigue initial perpendicular crack differed from the other perpendicular cracks in that it had propagated on two separate crack planes and subsequently joined together (Figure 6.9). All other perpendicular cracks had only propagated on a single crack plane. For both of the corrosion fatigue tests using precorroded test specimens, the size of the flat perpendicular cracks had increased when compared to the non-precorroded corrosion fatigue counterparts. Since the tests were performed at temperatures at which a protective alumina scale does not form, the propagation stage of corrosion would have started relatively early. The importance of precorroding the specimens was therefore to diffuse the corrosive species into the material before the fatigue testing started.

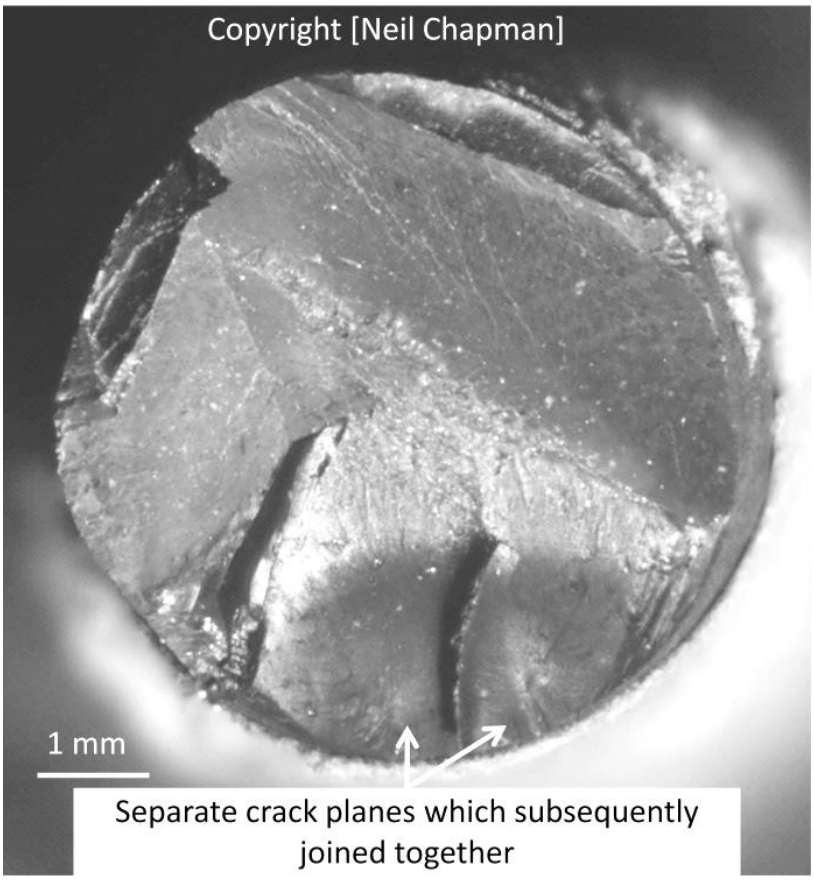

Figure 6.9: Low powered optical microscope image of two initial flat perpendicular cracks from the corrosion fatigue test using the 10-1-1-1 s waveform and precorroded test specimen

The precorroded test specimen that had all of the salt deposits washed off and then tested in air using a 10-1-1-1 s waveform, exceeded the duration of the precorroded corrosion fatigue counterpart by a factor of 5 without failing. This test was considered a runout and indicated that the salt deposits and SO_x environment were of greater significance than any potential corrosion pitting that may have occurred during the initial precorrosion phase.

SEM analysis of the initial flat perpendicular corrosion fatigue cracks found on the precorroded and non-precorroded test specimens, suggested propagation could initiate and occurred from internal pores (Figure 6.10) as well as surface breaking corrosion pits. Un-etched microsections (Figure 6.11) confirmed the initial flat cracks were approximately 90° to the surface of the test specimens and after electrolytically etching in a solution of: 20 mls hydrofluoric acid, 40 mls of glycerol and 340 mls of water, the internal pores appeared to be associated with eutectic regions (Figure 6.12).

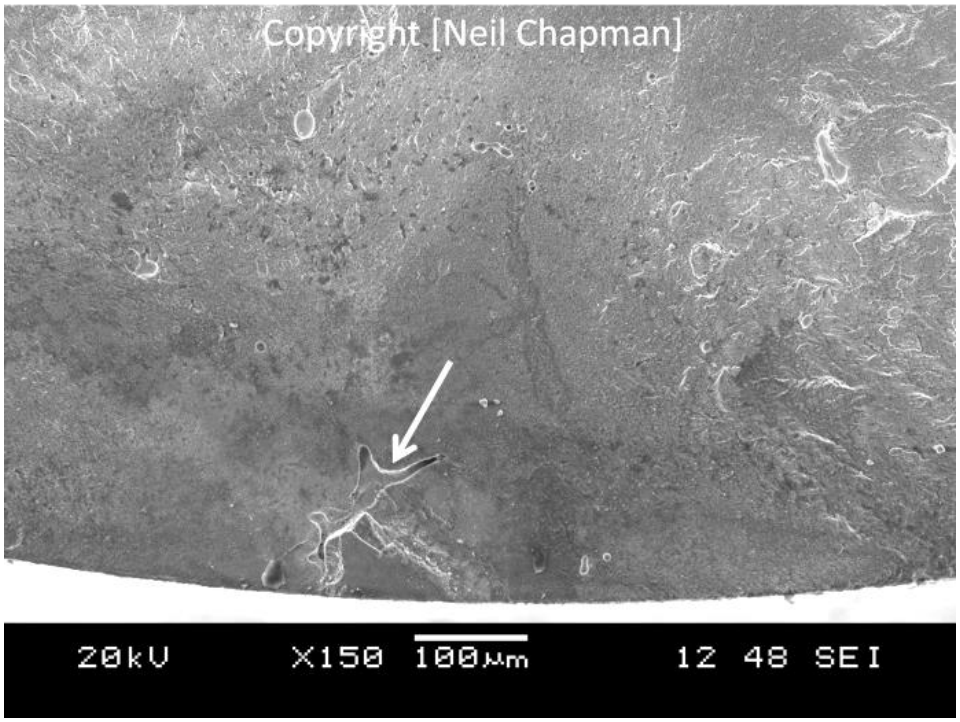

Figure 6.10: SEM image showing an example of an internal origin of the initial flat perpendicular corrosion fatigue crack (produced using the 10-1-1-1 s waveform and non-precorroded test specimen)

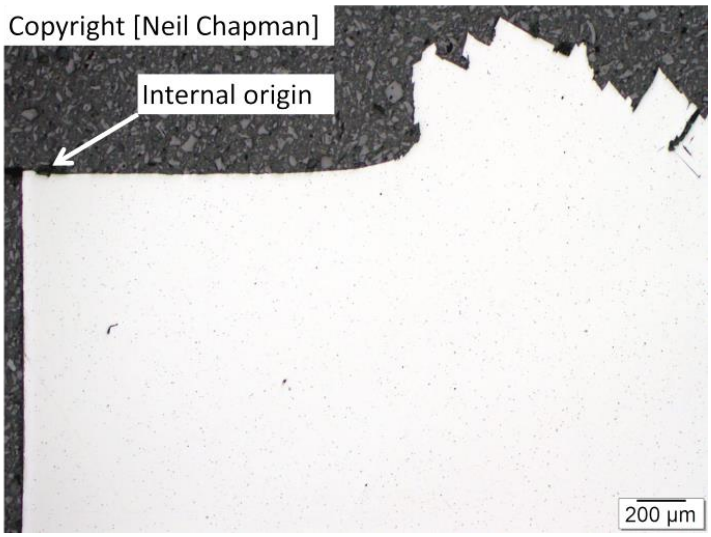

Figure 6.11: High powered optical microscope image of un-etched microsection showing an example of the initial flat perpendicular corrosion fatigue crack (produced using the 10-1-1-1 s waveform and non-precorroded test specimen)

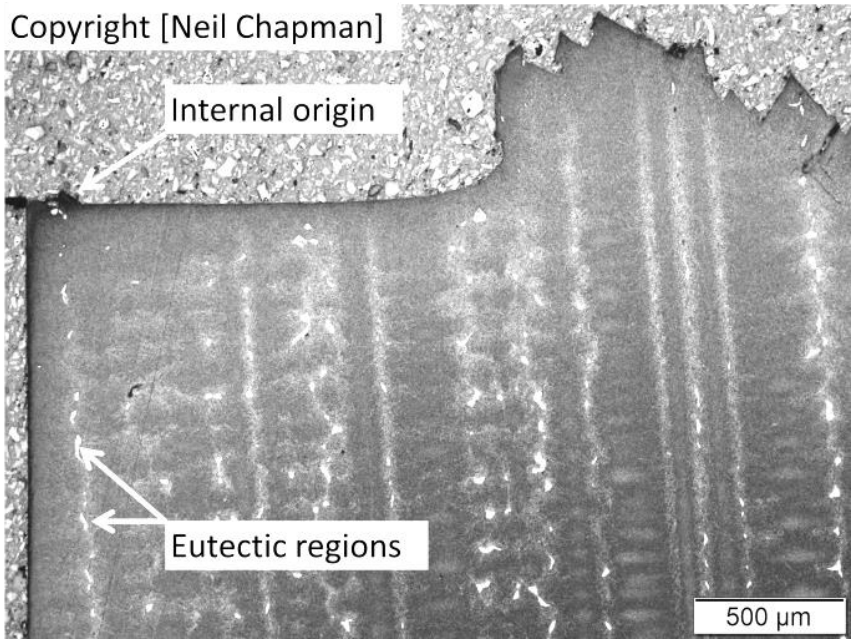

Figure 6.12: High powered optical microscope image of etched microsection showing an example of the initial flat perpendicular corrosion fatigue crack (produced using the 10-1-1-1 s waveform and non-precorroded test specimen)

The results obtained suggest that the internal pores associated with eutectic regions within the material were prime sites for the initiation of corrosion fatigue cracks. These pores may have acted as stress raisers in a material that was likely to have been affected by the diffusion of the corrosive species. Once a crack had initiated, low rates of application of stresses during the fatigue cycling may have resulted in fewer dislocations generated at the crack tip and thus minimised any possible crack tip blunting. In turn, the localised peak stresses associated with the sharper cracks may have caused a relatively large plastic zone ahead of the crack tip containing high vacancy concentrations within the associated slip bands [9], along with a greater concentration of micro-cracks [7]. This would provide short circuit diffusion paths allowing a relatively fast diffusion of the corrosive species (believed to be sulphur). Additionally, the beach marks observed are suggestive that the corrosion fatigue cracking was a start-stop-start process. This would be possible if the rate of crack propagation was greater than the rate of corrosive diffusion. That is, once a crack tip had caught up with the diffusion front, the crack would have stopped propagating if the remaining cross sectional area of the test specimen could support the load. The corrosive diffusion though would continue and when the material ahead of the crack tip had been sufficiently affected, the crack would start to propagate again until it once again caught up with the diffusion front. If the size of the remaining cross section of the test specimen was insufficient to support the load, the crack would begin to propagate every cycle until final fracture occurred. Under this condition, and without the influence of the environment, the crack growth transitioned back to the 55° classic slip band angle for this alloy system.

In summary, the factors which appeared to have affected the typical air fatigue mechanism the most under the corrosive test conditions used were the load application rate and precorrosion of the test specimens. The observation that the load application rate had affected the mechanism was in agreement with the findings, albeit based on different materials, corrosive conditions and temperature of testing, from Ref. 10, which concluded

that this was due to the dissolution of the corrosive species on the freshly exposed crack surfaces formed under the load application period. The molecular dynamic simulations performed in Ref. 6 though, indicate that the change in mechanism may also be associated with the lack of crack tip blunting associated with low strain rates.

6.4. Paper 5 conclusion

The parameters that affected the typical air fatigue mechanism of solution treated and precipitation hardened CMSX-4 material cast in the <001> orientation the most, when tested under the corrosive conditions, were the 10-1-1-1 s waveform and precorrosion of the test specimens. It is postulated that with stress application rates as low as 80 MPa s^{-1}, significant crack tip blunting by the generation of dislocations at the tip of the crack did not occur and cycling of the associated peak stress values at the crack tip caused a relatively large plastic zone to form in front of the advancing crack. This plastic zone with its high vacancy concentrations within the associated slip bands along with the formation of micro-cracks ahead of the crack tip would have allowed a fairly rapid diffusion of the corrosive species, believed to be sulphur in this case, that may ultimately have caused the change in fatigue mechanism. The precorrosion of the test specimens ensured that the corrosive elements had diffused sufficiently into the material and the fatigue testing was performed on corroded material.

Acknowledgements

The authors would like to acknowledge Siemens Industrial Turbomachinery Limited for the funding of the work.

6.5. Paper 5 references

1. B. Bordenet: 'High temperature corrosion in gas turbines: thermodynamic modelling and experimental results', PhD thesis, RWTH Aachen University, Saarbrucken, Germany, 2004, 7-11.
2. H. Lai: 'High temperature oxidation and corrosion of ni-based superalloys for industrial gas turbines', PhD thesis, Chalmers University of Technology, Goteborg, Sweden, 2014, 2-19.
3. J. Sumner, A. Encinas-Oropesa, N. J. Simms and J. R. Nicholls: 'Type II hot corrosion: behaviour of CMSX-4 and IN738LC as a function of corrosion environment', *Materials and Corrosion*, 2014, **65**, (2), 188-196.
4. P. P. Milella: 'Fatigue and corrosion in metals' 1, 8-15, 2013, Milan, Springer (e-book, available at [http://www.springer.com/gp/book/9788847023352]).
5. G. E. Korth: 'Effects of various parameters on the fatigue life of alloy 718, *TMS*, 1991, Superalloys 718, 625 and Various Derivatives, 457-476.
6. W. P. Wu and Z. Z. Yao: 'Influence of a strain rate and temperature on the crack tip stress and microstructure evolution of monocrystalline nickel: a molecular dynamics simulation', *Strength of Materials*, 2014, **46**, (2), 164-171.
7. H. J. Lim, B. Song, B. Park and H. Sohn: 'Noncontact fatigue crack visualization using nonlinear ultrasonic modulation', *NDT&E International*, 2015, **73**, 8-14.
8. C. E. Jaske, J. H. Payer and V. S. Balint: 'Corrosion fatigue of metals in marine environments', Report MCIC-81-42, Metals and Ceramics Information Center, Ohio, USA, 1981, 1-262.
9. A. Stockdale: 'The corrosion and corrosion fatigue behaviour of nickel based alloy weld overlay and coextruded claddings', PhD thesis, Lehigh University, Bethlehem, Pennsylvania, USA, 2014, 19-26.
10. S. Kawai and K. Koibuchi: 'Effect of waveform on corrosion fatigue crack growth', *Fatigue of Engineering Materials and Structures*, 1979, **1**, 395-407.
11. B. Ruttery, M. Ramsperger, L. Mujica Roncery, I. Lopez-Galilea, C. Korner and W. Theisen: 'Impact of hot isostatic pressing on microstructure of CMSX-4 Ni-base superalloy fabricated by selective electron beam melting', *Materials and Design*, 2016, **110**, 720-727.

7. Overall discussion

7.1. Crack initiation and propagation generated by combined static loading and LTHC

GT blades are often subjected to duty cycles with prolonged periods of mean tensile loading. Therefore, consideration of static loading in combination with LTHC condition environments which are representative of the under platform location, is an important factor in relation to the life cycle of the component. As such, experimental testing was conducted on statically loaded specimens which were simultaneously subjected to LTHC environments. This experimentation identified and demonstrated that crack initiation and propagation could occur under these combined conditions, being driven primarily by environment and exposure time, rather than stress or load cycles.

Under conventional unstressed conditions LTHC forms a pitting morphology. These pits then conjoin to form a broad fronted attack. However, when combined with static tensile loading the degradation mechanisms morphology changes to generate the crack initiation and propagation. Due to the absence of fatigue cycles it can be deduced that the crack initiation and propagation observed under static loading, is not the result of conventional fatigue cracking mechanisms such as dislocation emission. Therefore, seeing as the mechanism of crack initiation and propagation is likely different under cyclic and static loading, it is necessary to consider the factors affecting cracking generated by these two load conditions independently.

The parameters which influence crack initiation and propagation under static loading have been studied and are presented in papers 1 and 3. It was found that crack initiation and propagation was influenced by stress state, deposit flux and exposure time. It can be rationalised that increasing the deposit flux and the exposure time generates increased LTHC, and therefore increases the rate of cracking which is driven by LTHC. However, it was observed that the aggressiveness of the static cracking mechanism most closely corresponded to the stress gradient in front of the crack, and not to the maximum principle stress or von Mises stress within the specimen geometries studied. It is well documented that a stress gradient can provide a crack driving force which has the effect of accelerating surface initiated crack nucleation particularly in fretting fatigue [1][2]. Similarly to fretting fatigue cracks generated under LTHC environments were found to be surface initiated; as such it could be argued that the initiation and propagation rates of cracks generated in static load conditions are also similarly affected by stress gradient.

The influence of load/stress on the corrosion mechanism was not independently studied over the course of the project, however an effect of load on the LTHC mechanism's preference to attack specific γ or γ' phases of the alloy was observed in paper 4. This observation demonstrates that the loading condition does have an effect on the LTHC mechanism. It was postulated in paper 4 that this could be related to the electrochemical anodic potential of the phases under loading and deformation as a result of mechanochemical. Given that it has been observed that loading and deformation can have an effect on the preference of the LTHC to

attack microstructural phases, it is therefore plausible that there could also be an impact of loading and deformation on the rate of LTHC. This could firstly be as a result of the γ/γ' volume fraction affecting the corrosion rate given the preferential attack of the phases under certain loading conditions. CMSX-4 has a large γ' volume fraction [3] which could mean that LTHC rates are relatively higher under tensile loading than compressive. Secondly, there could be an impact of mechanochemical effects under loading and deformation, influencing the electrochemical potential of the alloy substrate and resultantly the rate of LTHC. Throughout the experimental work presented it has been demonstrated that the corrosion generated in loaded specimens is consistent with LTHC, even though the temperature of 550 °*C* is below the normal range considered for LTHC. It can therefore be suggested that the mechanism is sub LTHC, and may be assisted by load and deformation in some capacity.

The absence of rafting of the γ/γ' microstructure in specimens post exposure confirms that creep is not a major consideration at temperatures as low as 550 °C. However, interactions between static load LTHC cracking and creep will become an important consideration at higher temperatures. It will therefore be important to consider whether creep is present in future higher temperature work.

7.2. Effect of LTHC on fatigue life and crack propagation

The combined effects of LTHC and fatigue were studied experimentally, these results are presented and discussed in papers 2, 3 and 5. It was demonstrated that in LTHC environments the following parameters reduced the fatigue life: increases in exposure time, deposit flux and load dwell periods. There was also an impact observed between the fatigue life and the load application rate with lower load application rates exhibiting reduced fatigue performance.

The fatigue testing conducted throughout this project was performed under load control, therefore the data has been presented as stress cycles to failure (S-N) curves. S-N curves provide a fatigue life comparison to stress life data already available for CMSX-4 in standard air environments. Therefore, the relative impact of the studied parameters can be assessed from the presented S-N curves. However, it has been demonstrated within the work presented in this thesis, that there are limitations in using conventional fatigue modelling approaches such as stress life, for modelling crack initiation and propagation within combined LTHC and fatigue environments. One of the reasons for this is because the fatigue life within LTHC conditions is dependent on a range of time and environment dependant parameters which are not captured by conventional fatigue modelling approaches. The second is because these methodologies fundamentally correlate calculable engineering parameters to crack stability and propagation. It is often argued that parameters that are representative of what actually is physically occurring locally within the material, such as strain and plasticity can provide better correlation with fatigue crack propagation. Furthermore, it is often argued that fatigue crack propagation occurs as a result of dislocation emissions and plasticity [4]. There is an argument therefore, to say that when considering microscopic cracks initiating and

propagating through crystallographic materials, then crystallographic strain and plasticity provide a better basis for detailed modelling.

However, the engineering challenges of accurately modelling the cracking mechanism generated due to combined LTHC and fatigue is not simple due to the number of factors and variables which have an impact. Therefore, the development of more simplistic engineering adaptations of stress and fracture mechanics based approaches, which further include corrosion and time dependant parameters could be the first step in order to provide a useful tool for the industry requirements and better predict crack initiation and propagation within LTHC environments.

More detailed and accurate modelling of the mechanism would probably be best suited to crystal strain and plasticity based approaches. However, there are considerable challenges and complexities in applying these modelling approaches to alloy systems and engineered components. Such as the computational demands that would be required to solve them, as well as the further development that would be required in order for them to accurately account for environmental effects and crack growth under static load.

It has been generally observed and reported in the literature that LTHC has a detrimental effect on the fatigue life of superalloys [5][6][7][8][9][10]. The mechanism that the literature focuses on to explain this observation is LTHC accelerating fatigue crack initiation as a result of corrosion pitting. Stress concentration as a result of pitting is undoubtedly an important factor, however the research presented in papers 1, 3 and 4 demonstrates that there is a static load crack propagation which, under certain conditions, can interact with and enhance the fatigue crack propagation. The interactions of this static load growth and fatigue provides a notable development in how the fatigue life modelling approaches should be used in respect to superalloys exposed to LTHC conditions. These interactions and considerations were further presented and discussed within papers 2 and 3.

Fractographic analysis of specimens was used to provide information on how LTHC, load and fatigue interact. Several observations were made from the experimental results and subsequent specimen examination. Firstly, crack initiations tended to show a preference to propagate on {100} crystallographic planes with the introduction of LTHC. Secondly, multiple surface crack initiations were observed with increased exposure to LTHC and extended load dwell periods and thirdly, fracture faces show environmental banding particularly near the point of initiation in LTHC environments. These observations suggest that the combined action of LTHC and fatigue has the greatest effect on the fatigue crack nucleation and initiation, probably with some interactions occurring between fatigue cracking and static load cracking. An overview of the proposed crack growth stages observed in SC superalloys such as CMSX-4 exposed to LTHC environments is given in Figure 7.1.

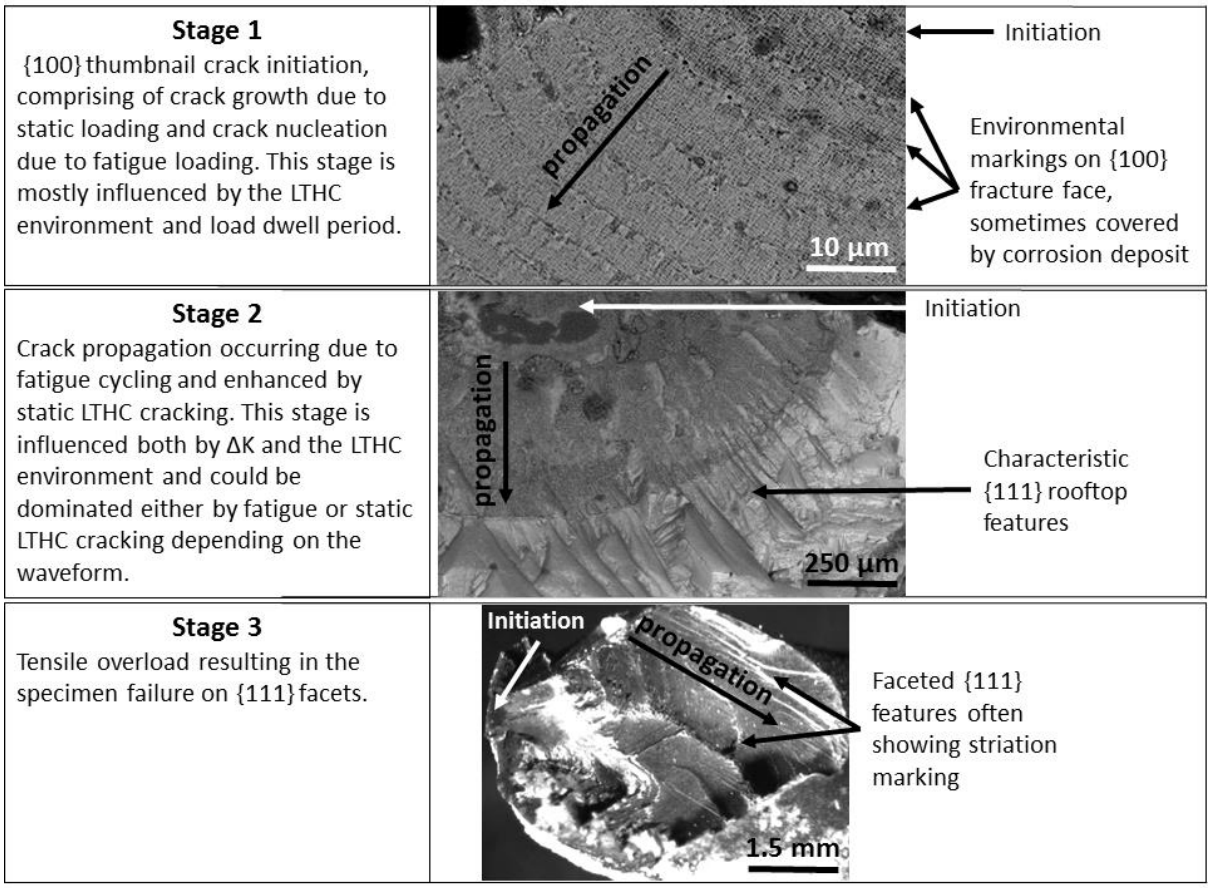

Figure 7.1: Stages of crack growth in combined fatigue and LTHC environments, observed in testing conducted at 550 °C

It should be recognised that the crack propagation plane is influenced by a number of other factors such as temperature, crystallographic orientation, stress field and defects within the material. Therefore, the observations made in relation to the impact of LTHC propagation plane are specific to the material, temperature and plain cylindrical uniaxial specimen geometry used.

7.3. The mechanisms of LTHC crack propagation

The mechanism by which LTHC enables crack initiation and propagation was studied and discussed in papers 3 and 4. A preliminary mechanism explaining preferential {100} crack propagation and γ' attack at the crack tip was proposed in paper 3, which is referred to as mechanism 1. Following paper 3, more in-depth SEM, TEM and EDX analysis combined with in depth review of similar mechanisms in the literature informed a more detailed and developed mechanism which was presented in paper 4 as mechanism 2.

These two mechanisms aim to explain the localised material degradation enabling crack initiation/propagation morphologies, as well as the preferential corrosion attack of the γ' at

the crack tip and γ towards the substrate surface, they do this using the analysis available at the time the paper was written. The analysis presented in paper 3 does not provide high enough magnification and characterisation of the crack tip, in order to accurately establish whether or not there were any corrosive species present at the crack tip, or diffusion ahead of the crack tip. A mechanism was therefore proposed where gas induced acidic fluxing occurs at the crack tip, interacting preferentially with the γ' and generating localised material degradation. A more conventional LTHC alloy induced form of acidic fluxing was proposed as occurring towards the specimen surface which interacts preferentially with the γ. It was further proposed that the {100} crack propagation seen under LTHC conditions is explained by the preferential γ' attack at the crack tip, where geometrically the next closest γ' precipitates are orthogonally located around the crack tip. Therefore, the next closest γ' to be attacked is orthogonally located on {100} crystallographic planes causing preferential crack propagation in these directions.

However, with the addition of more detailed TEM imaging and high magnification EDX mapping, it was determined that there were in fact sodium based corrosive species present at the crack tip. The presence of sodium species at the crack tip, which is reported to be an ionic conductor or electrolyte in electrochemical LTHC mechanisms [11], opens up the possibility that the crack tip corrosion mechanism is electrochemical and not purely gas induced. On the back of these new findings mechanism 2 was proposed. This mechanism is based on localised material degradation at the crack tip being explained by the establishment of a localised anodic region which generates localised acidic dissolution, similar to what is reported in aqueous corrosion mechanisms [12].

Consideration of mechanism 2 and the compressive/tensile loading effect on preferential γ/γ' attack opens up another possible explanation for the preferential corrosion attack of the microstructural phases. Mechanochemical interactions are well documented in electrochemical mechanisms [13][14][15] where stress/deformation can influence the anodic potential of the material. It was proposed that due to the different mechanical properties of the two γ/γ' phases, that these mechanochemical interactions could impact the phases differently thus influencing the corrosion preference under given load conditions.

There is no conclusive evidence presented within this research to definitively confirm whether a change in the fluxing mechanism generates the preferential γ/γ' attack or whether the mechanochemical interactions proposed in mechanism 2 do. However, the mechanochemical mechanism presents a reasonable explanation for the stress effect on the preferential corrosion attack of the γ/γ' microstructure observed in paper 4. The aspects of the mechanism that are well evidenced are firstly, that it is likely a stress assisted electrochemical LTHC mechanism due to the presence of electrolytic species at the crack tip.Secondly that the mechanism generates localised material degradation that facilitates crack propagation even under static tensile loading. Hence, a finalised mechanism based on the observations and ideas presented in papers 3 and 4 is presented in Figure 7.2.

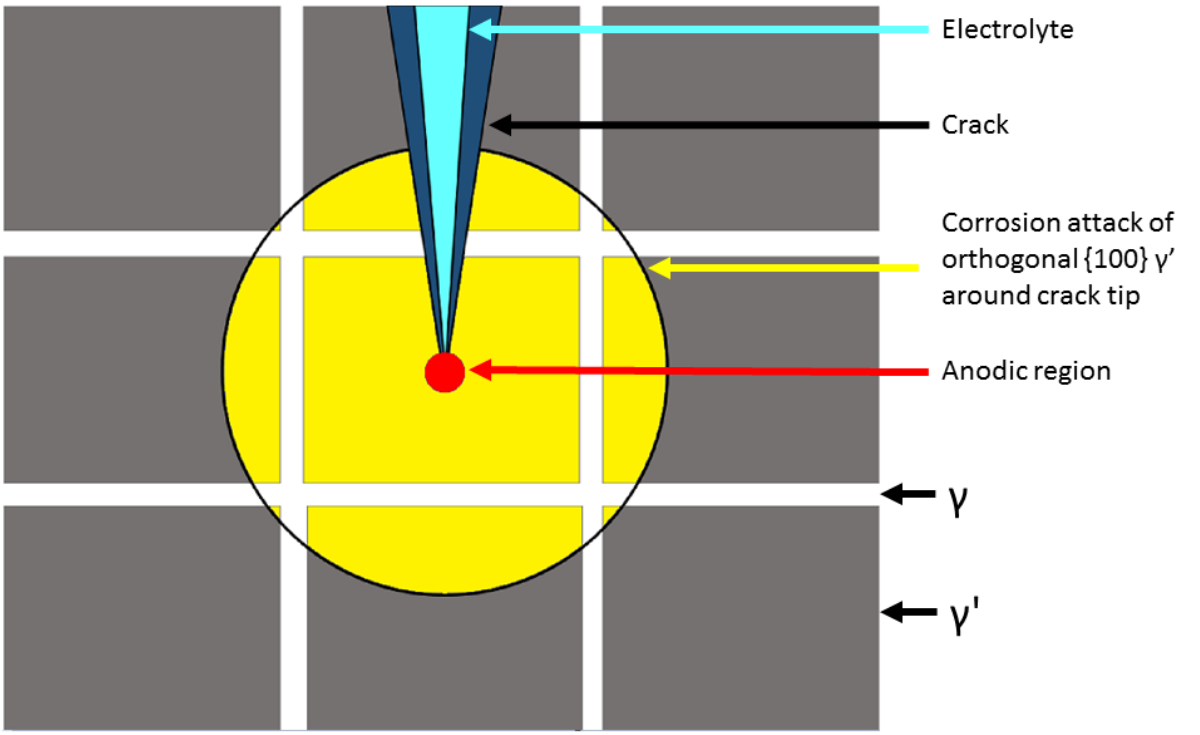

Figure 7.2: Finalised mechanism of electrochemical corrosion attack resulting in orthogonal {100} propagation

This mechanism proposes a high temperature electrochemical material degradation where an anodic region is established at the crack tip. This electrochemistry generates localised acidic fluxing and results in localised material degradation and subsequent crack propagation similar to the mechanism proposed in paper 4. Furthermore, the preferential attack of the corrosion mechanism at the crack tip to the γ' generates crack propagation preferential to {100} planes as postulated in paper 3.

The detailed electron microscopy analysis presented within paper 4, demonstrates that the cracking mechanism occurs due to interactions between deformation within the crystallographic lattice, and complex chemical degradation which is likely to be electrochemical in nature. The specifics of the way in which these interactions generate localised crystallographic de-cohesion, are not fully understood at this point. Basics principles of the mechanism have been proposed and further study of simplified electrochemical corrosion systems and material systems could provide further detail into the specifics of the mechanism and the drivers behind the material degradation which has been observed throughout the course of this research.

7.4. Discussion references

[1] R. Amargier, S. Fouvry, L. Chambon, C. Schwob, and C. Poupon, “Stress gradient effect on crack initiation in fretting using a multiaxial fatigue framework,” *Int. J. Fatigue*, vol. 32, no. 12, pp. 1904–1912, 2010.

[2] R. Ferré, S. Fouvry, B. Berthel, and J. A. Ruiz-Sabariego, “Stress gradient effect on the crack nucleation process of a Ti-6Al-4V titanium alloy under fretting loading: Comparison between non-local fatigue approaches,” *Int. J. Fatigue*, vol. 54, pp. 56–67, 2013.

[3] C. Körner, M. Ramsperger, C. Meid, D. Bürger, P. Wollgramm, M. Bartsch, and G. Eggeler, “Microstructure and Mechanical Properties of CMSX-4 Single Crystals Prepared by Additive Manufacturing,” *Metall. Mater. Trans. A Phys. Metall. Mater. Sci.*, vol. 49, no. 9, pp. 3781–3792, 2018.

[4] P. Chowdhury and H. Sehitoglu, “Mechanisms of fatigue crack growth - A critical digest of theoretical developments,” *Fatigue Fract. Eng. Mater. Struct.*, vol. 39, no. 6, pp. 652–674, 2016.

[5] S. Li, X. Yang, H. Qi, J. Song, and D. Shi, “Low-temperature hot corrosion effects on the low-cycle fatigue lifetime and cracking behaviors of a powder metallurgy Ni-based superalloy,” *Int. J. Fatigue*, vol. 116, no. January, pp. 334–343, 2018.

[6] H. Rosier, K. Perkins, A. Girling, J. Leggett, and G. Gibson, “Factors affecting the corrosion fatigue life in nickel based superalloys for disc applications,” *MATEC Web Conf.*, vol. 14, p. 03001, 2014.

[7] G. Jianting, D. Ranucci, and E. Picco, “Low cycle fatigue behaviour of cast nickel-base superalloy IN-738LC in air and in hot corrosive environments,” *Materials Science and Engineering*, vol. 58, no. 1. pp. 127–133, 1983.

[8] G. S. Mahobia, N. Paulose, S. L. Mannan, R. G. Sudhakar, K. Chattopadhyay, N. C. Santhi Srinivas, and V. Singh, “Effect of hot corrosion on low cycle fatigue behavior of superalloy IN718,” *Int. J. Fatigue*, vol. 59, pp. 272–281, 2014.

[9] M. Y. Nazmy, “The effect of environment on the high temperature low cycle fatigue behaviour of cast nickel-base IN-738 alloy,” *Mater. Sci. Eng.*, vol. 55, no. 2, pp. 231–237, 1982.

[10] (Westinghouse Combustion Turbine Systems) Allen, J, M and (Westinghouse Reaserch and Development Center) Whitlow, G, A, “Observations on the Interaction of High Mean Stress and Type II Hot Corrosion on the Fatigue Behavior of a Nickel Base Superalloy,” *J. Eng. Gas Turbines Power*, vol. 107, pp. 220–224, 1985.

[11] R. A. Rapp, “Hot corrosion of materials: A fluxing mechanism?,” *Corros. Sci.*, vol. 44, no. 2, pp. 209–221, 2002.

[12] L. G. Bland and J. S. Locke, “Chemical and electrochemical conditions within stress corrosion and corrosion fatigue cracks,” *npj Mater. Degrad.*, vol. 1, no. 1, p. 12, 2017.

[13] D. Svedruzic and B. A. Gregg, “Mechano-electrochemistry and fuel-forming mechano-

electrocatalysis on spring electrodes," *J. Phys. Chem. C*, vol. 118, no. 33, pp. 19246–19251, 2014.

[14] F. Farhad, X. Zhang, and D. Smyth-Boyle, "Fatigue behaviour of corrosion pits in X65 steel pipelines," *Proc. Inst. Mech. Eng. Part C J. Mech. Eng. Sci.*, vol. 0, no. 0, pp. 1–12, 2018.

[15] E. M. Gutman, G. Solovioff, and D. Eliezer, "The mechanochemical behavior of type 316L stainless steel," *Corros. Sci.*, vol. 38, no. 7, pp. 1141–1145, Jul. 1996.

8. Overall conclusions and future work

8.1. Overall conclusions

The specific contributions to knowledge delivered by each paper are outlined in the paper overviews which are given in the introduction section 1.7. The overall collective conclusions and key findings from the research is outlined below.

- The work presented demonstrates a cracking mechanism generated under static loading conditions in a LTHC corrosion environment; it further demonstrates the LTHC environments detrimental impact on fatigue life. These findings provide a notable development in the way in which crack initiation and propagation should be considered within LTHC environments. Particularly as previous published work does not highlight static stress corrosion cracking in superalloys under LTHC conditions.

- FEA modelling was used to determine multiaxial stress states and predict stress intensities within specimen geometries. This data was used to study the influence of stress state on crack initiation and propagation within LTHC environments.

- It was experimentally found that the static load crack initiation time was decreased and subsequent propagation rate increased with increases to the following parameters; deposition flux, exposure time and stress gradient. Similarly the fatigue life was found to be detrimentally influenced by increased load dwell periods, reduced load application rate and increased deposition flux. However, stress and stress state were found to be secondary influences on crack initiation and propagation rates under static loading, with the primary factor being deposition flux.

- Fractographic analysis suggests that static load crack propagation and fatigue crack propagation interact with one another and collectively contribute to a combined crack propagation. This was particularly the apparent with increased load dwell periods and increased rates of corrosion where these influences could be observed in both the fracture face morphology and the cycles to failure.

- Detailed analysis of the crack tip was used to inform and propose a mechanism which explains the features and behaviours associated with LTHC cracking and fatigue studied over the course of the research. It is proposed the mechanism is electrochemical in nature and comparable with more widely understood stress corrosion cracking mechanisms such as aqueous corrosion cracking.

8.2. Future work

8.2.1. Need for improved models

Whilst service life and time dependant factors have been included in some fatigue and lifing strategies, these methods do not accurately capture when there is an aggressive mechanistic interaction such has been found in this research between low temperature hot corrosion and stress.

With the ever increasing industrial and political demands on power generation systems such as gas turbines to be more efficient, and cheaper to operate and maintain. There is a need to mechanistically study and understand the drivers behind crack initiation and propagation due to combined corrosion, stress, fatigue and creep in high temperature applications.

For turbine blades this is a requirement from both a safety and service cost perspective to develop new improved models for predicting crack initiation and propagation as a results of hot corrosion, stress, fatigue and often creep. However, this requirement to generate better combined or compound degradation models extends to other alloys in other applications.

In the case of GT blades and crack propagation in hot corrosion environments, there is additionally a requirement for improved modelling of the LTHC mechanism within superalloys. This is needed in order to be able to better predict the rate LTHC and therefore its impact on fatigue life and crack initiation performance of the component.

Currently, most LTHC models are empirically based and are dependent on parameters such as deposit flux and gas flux, as well as the specific chemistries present. Therefore, establishing the flux/deposition rate within a GT is needed in order to effectively predict the corrosion performance.

This deposition rate could theoretically be calculated using kinematic or thermodynamic calculations, however, this is a difficult process to model within the GT system because of the environmental variables which influence the flux/deposition rates of species in service. Examples of these would be the geographical location the GT operates in, the filtration used and the fuel type and quality used. Therefore, in order to do this in reality, a form of condition based monitoring of the turbine conditions would have to feed into the hot corrosion model.

8.2.2. Crack propagation measurement

The development of more accurate modelling of the crack propagation mechanism requires detailed crack propagation data, allowing the crack propagation to be quantified and the parameters impacting crack propagation to be determined. Improved models could then be developed to better life components under combined load and LTHC conditions.

There are not many widely used methodologies capable of achieving the kind of accuracy and precision required to capture the stages of crack initiation and propagation within the corrosive high temperature environment. At present the potential difference (PD) technique has promising capability and is commonly used for high temperature fatigue testing.

The PD technique uses a large current which is conducted through the specimen, PD probe wires are attached across the gauge length of the specimen where cracking is likely/expected to occur. As a crack initiates and propagates, an increase in the potential drop is measured due to the reduction in specimen cross sectional area. Therefore, over the course of a test the PD trace can be correlated to crack area growth and for a known crack aspect ratio the resultant crack length and depth.

However, whilst PD provides a promising methodology aspects of the testing methodology would require further development for use within a LTHC environments. For example, a rig which electrically insulates the specimen load train whilst exposing the specimen to a corrosive environment would have to be developed. Additionally the PD wires would be required to be made from a conductive but corrosion resistant material such as platinum, such wires would be both expensive and delicate to handle.

8.2.3. Improved understanding of the fundamental mechanism

At temperatures higher than the 550 ^{o}C studied in this research, for SC superalloys creep effects may come into play. Creep damage is well known to interact with fatigue nucleation damage and further consideration of creep in combination with the mechanism of LTHC and fatigue studied in this thesis, could provide valuable insight into the degradation of service components.

Additionally specific salt compositions will also have a direct influence on the mechanism and other environments could also sustain electrochemical corrosion. A systematic study of various salt compounds and other relevant environments such as H_2S could help to identify the most aggressive environments and inform operationally based lifing models.

In order to better protect against the degradation mechanism in the future, whether it be through changes in the blade geometry, alloys and materials, or through the development of new coating systems or even a form of electrochemical corrosion protection such as cathodic or magnetic, a more detailed fundamental understanding of the mechanism is required. The work presented within this thesis provides an initial mechanism. However, electrochemical corrosion testing and further static loading testing could be performed. Further analysis using TEM, high energy X-rays and atom probe methods may also help to better understand the chemical reactions occurring and how they enable crack initiation and propagation in combination with tensile loading.

The work presented within this thesis helps to inform the continued future studies into compound high temperature degradation mechanisms, which are crucial to the development of more efficient and robust power generation systems.

Appendices

Appendix 1: Un-normalised fatigue data

All testing was conducted at 550 ^{o}C, where a salt deposit was used it was an 80/20 wt% mix of Na/K sulphate. Specimens that received pre corrosion were not re-salted before the first 100 h of fatigue testing, but were salted as per normal beyond the first 100 h.

Test ID	Specimen #	Stress (MPa)	Wave form (s)	Pre Corrosion	Gas Flow (SCCM)	SO_x (ppm)	Test Flux (µg/cm²/h)	CTF
HCF 8	L3538	800	10-1-1-1	NO PRE	NO COR	NO SO_x	0	55716
HCF9	L3535	800	1-1-1-1	NO PRE	80	300	0	54618
HCF10	L4035	800	1-1-1-1	NO PRE	50	300	1.25	62710
HCF13	L4032	800	1-10-1-1	NO PRE	50	300	1.25	70623
HCF15	L4026	800	10-1-1-1	NO PRE	25	300	1.25	36162
HCF 16	L4036	800	1-1-1-1	PRE 5.0	25	300	5	39714
HCF 18	L4022	800	1-5-1-1	NO PRE	25	300	1.25	73247
HCF 19	L4018	800	10-1-1-1	PRE 5.0	25	300	5	14139
HCF 21	L4024	750	1-1-1-1	PRE 5.0	25	300	5	39618
HCF 27	L4020	700	1-1-1-1	PRE 1.25	25	300	1.25	151193
HCF 29	L4025	725	1-1-1-1	PRE 1.25	25	300	1.25	109039
HCF 30	L4021	775	1-1-1-1	PRE 1.25	25	300	1.25	76265
HCF 31	L4028	800	1-1-1-1	PRE 1.25	25	300	1.25	61991
HCF 33	L4037	750	1-1-1-1	PRE 1.25	25	300	1.25	103977
HCF 34	L4031	775	1-1-1-1	PRE 1.25	25	300	1.25	78516
HCF 35	L4023	775	1-1-1-1	PRE 1.25	25	300	1.25	48703
HCF 36	L4191	800	1-1-1-1	NO PRE	25	300	0	67184
HCF 38	L4191	775	10-1-1-1	PRE 5.0	25	300	5	33830
HCF42	L4206	700	1-1-1-1	PRE 5.0	25	300	5	84121
HCF 43	L4204	775	1-1-1-1	PRE 5.0	25	300	5	60933
HCF 47	L4201	725	1-1-1-1	PRE 5.0	25	300	5	50996
HCF 49	L4203	775	1-1-1-1	PRE 5.0	25	300	5	46293
HCF 50	L4199	750	1-1-1-1	PRE 5.0	25	300	5	38703
HCF 53	L4194	800	1-60-1-1	PRE 5.0	25	300	5	9022
HCF 54	L4202	850	1-60-1-1	PRE 5.0	25	300	5	3300
HCF 59	10310	750	1-60-1-1	PRE 5.0	25	300	5	9057
HCF 60	10313	825	1-60-1-1	PRE 5.0	25	300	5	8085

Appendix 2: Three point bend jig drawings

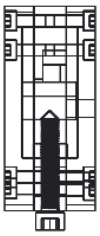

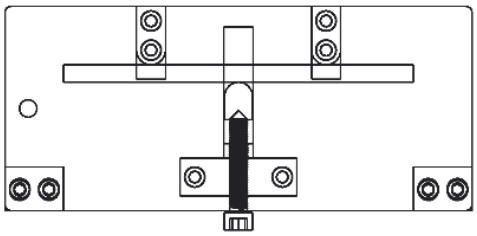

NOTE: ALL TOLERANCES SHOULD BE +/- 0.05mm

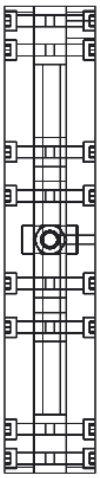

SCALE 1:500

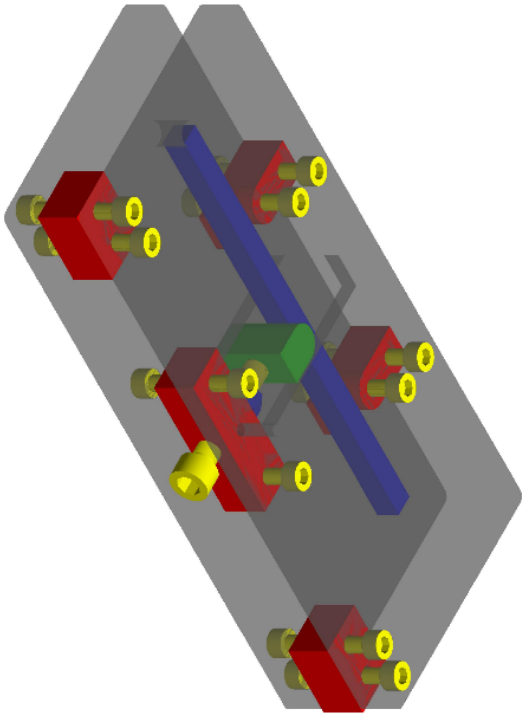

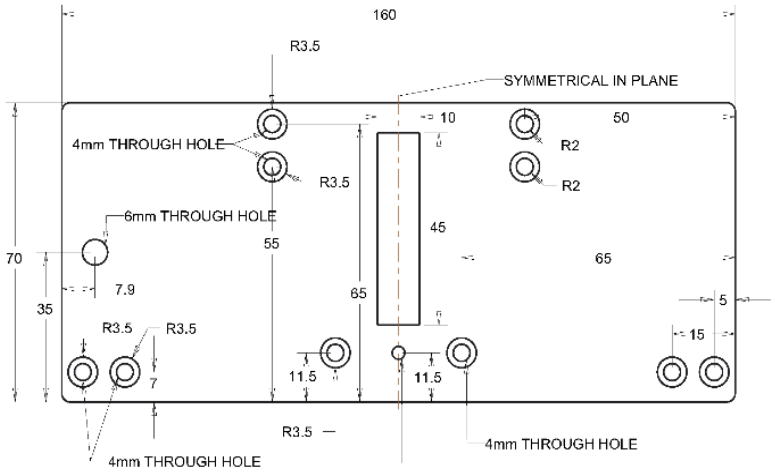

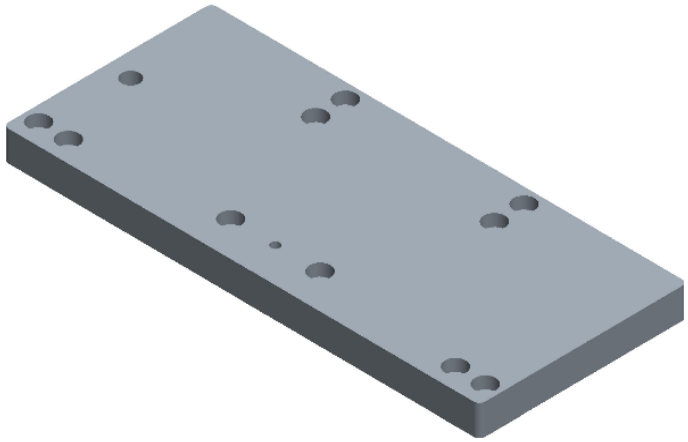

SCALE 1.500

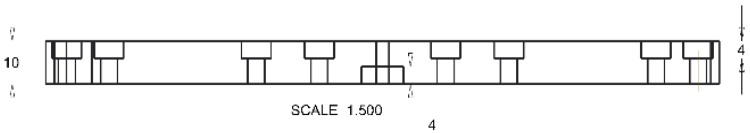

SCALE 1.500

4

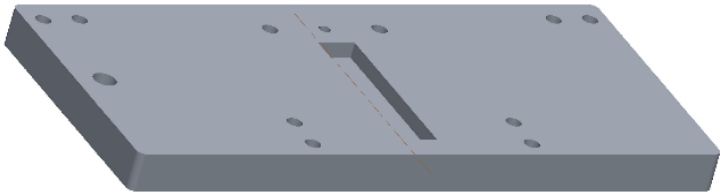

SCALE 1.500

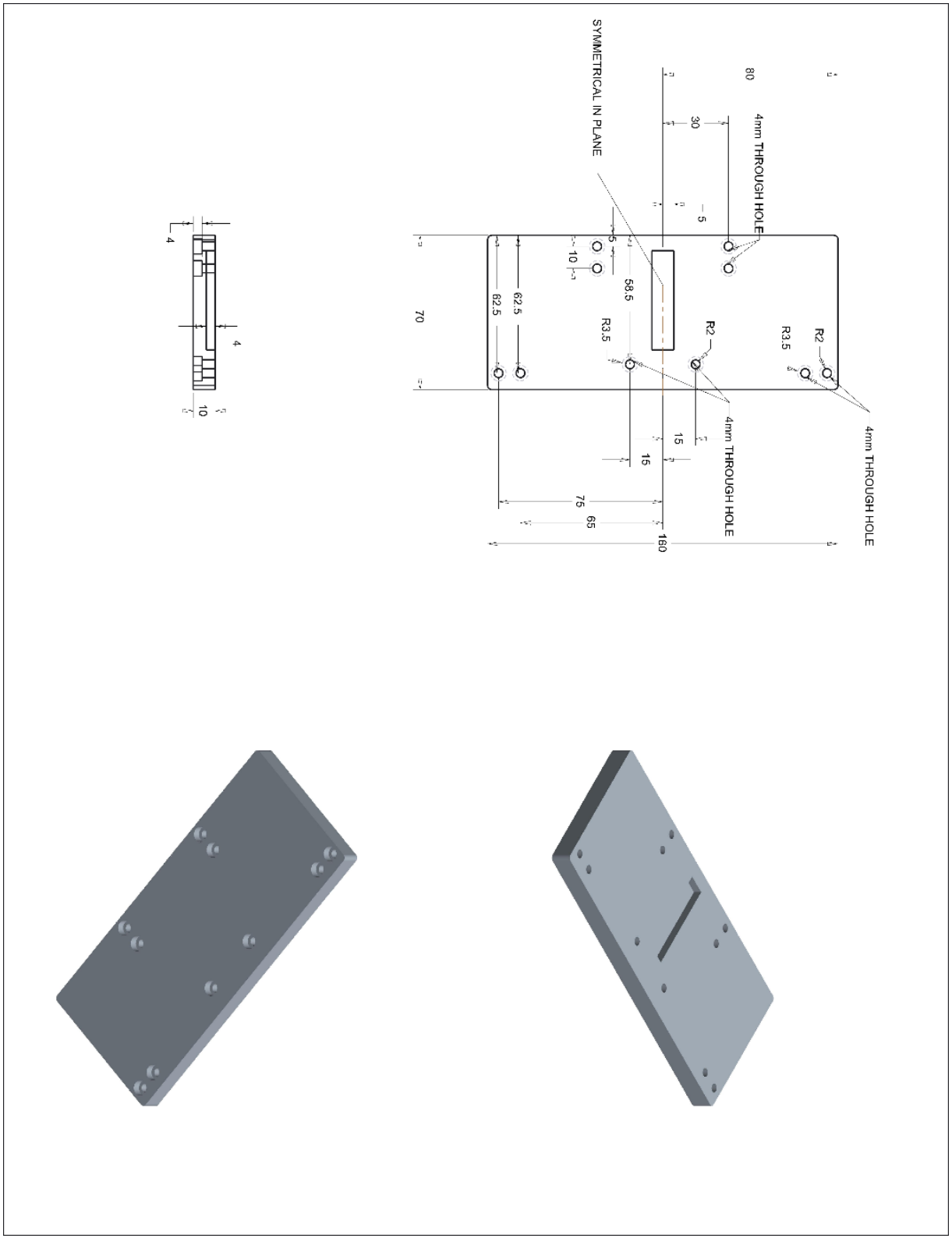
4mm THROUGH HOLE
80
30
5
SYMMETRICAL IN PLANE
10
5
58.5
62.5
62.5
70
R3.5
R2
R2
R3.5
4mm THROUGH HOLE
4mm THROUGH HOLE
15
15
75
65
160
4
4
10

NOTE: 2x PART REQUIERED FOR ASSEMBLY

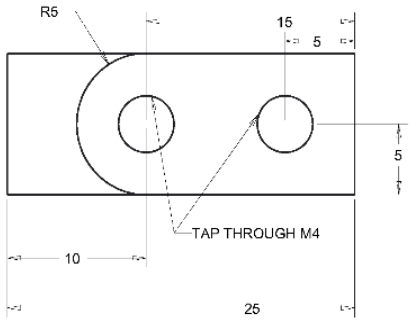

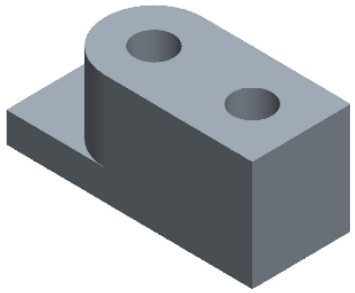

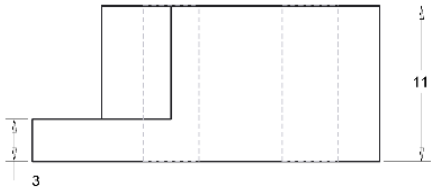

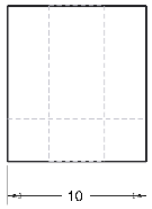

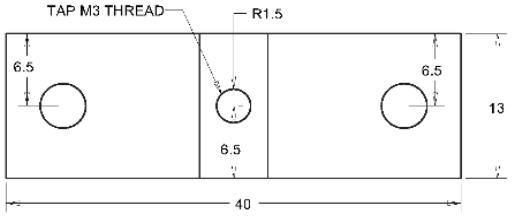
TAP M3 THREAD
R1.5
6.5
6.5
13
6.5
40

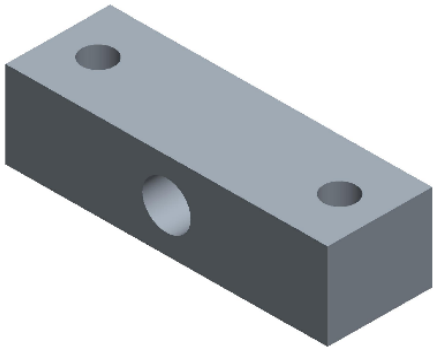

SCALE 4.000

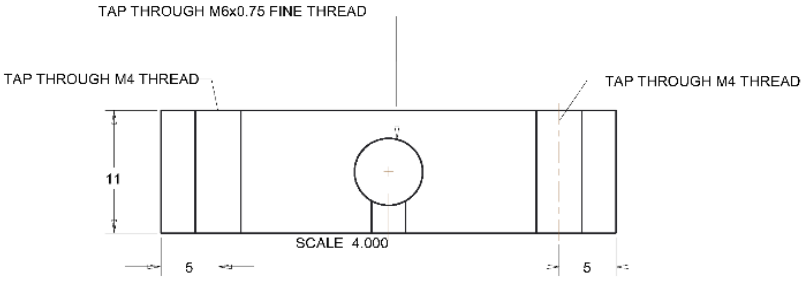
TAP THROUGH M6x0.75 FINE THREAD
TAP THROUGH M4 THREAD
TAP THROUGH M4 THREAD
11
SCALE 4.000
5
5

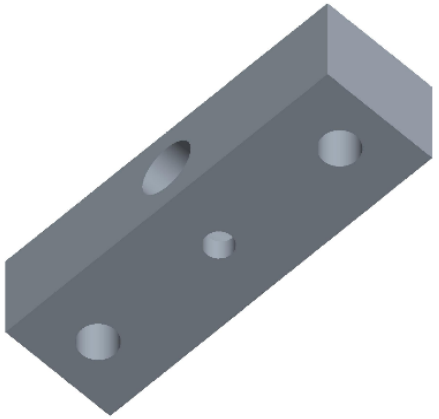

NOTE: 2xPART REQUIERED FOR ASSEMBLY

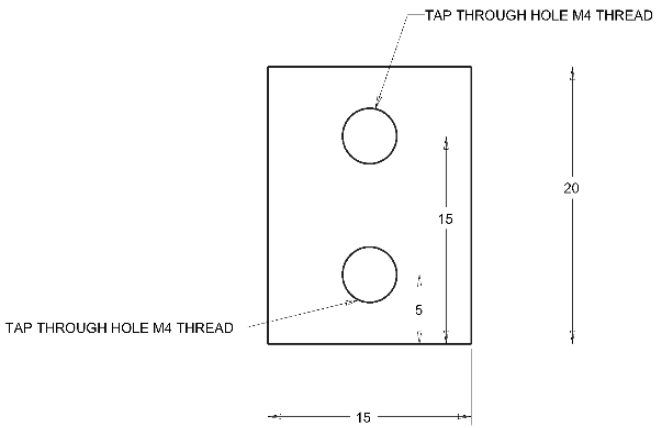

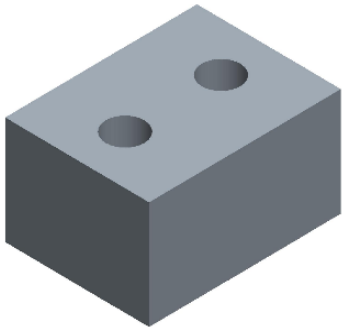

SCALE 5.000

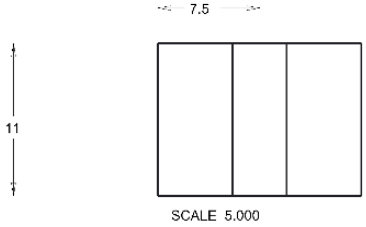

SCALE 5.000

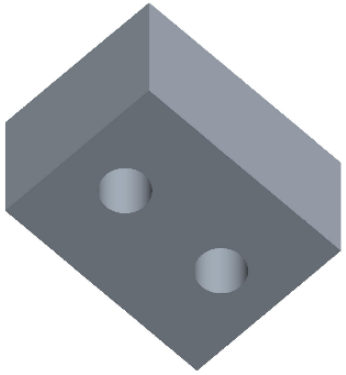

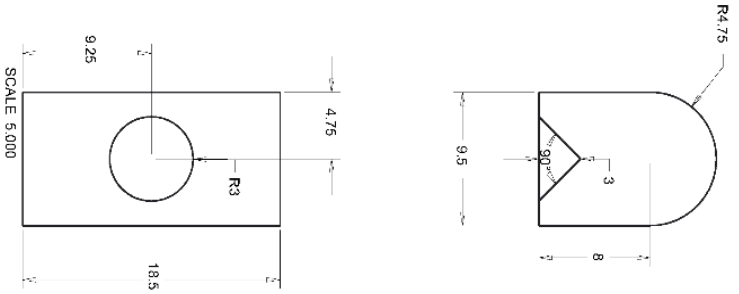
SCALE 5.000
9.25
4.76
R3
18.5
R4.75
9.5
90°
3
8


SCALE 5.000

NOTE: M6x0.75 FINE THREAD, 90 DEG CONICAL TIP

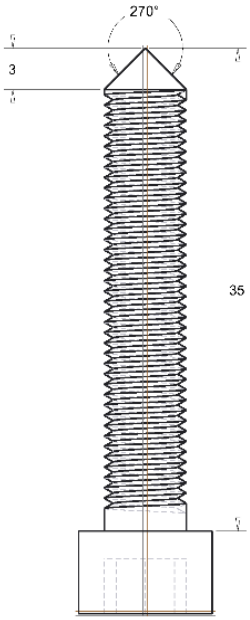

SCALE 5.000

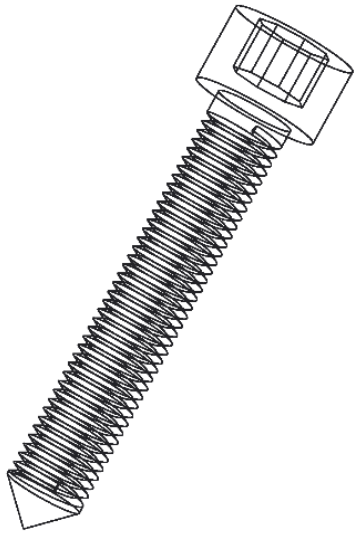

SCALE 5.000

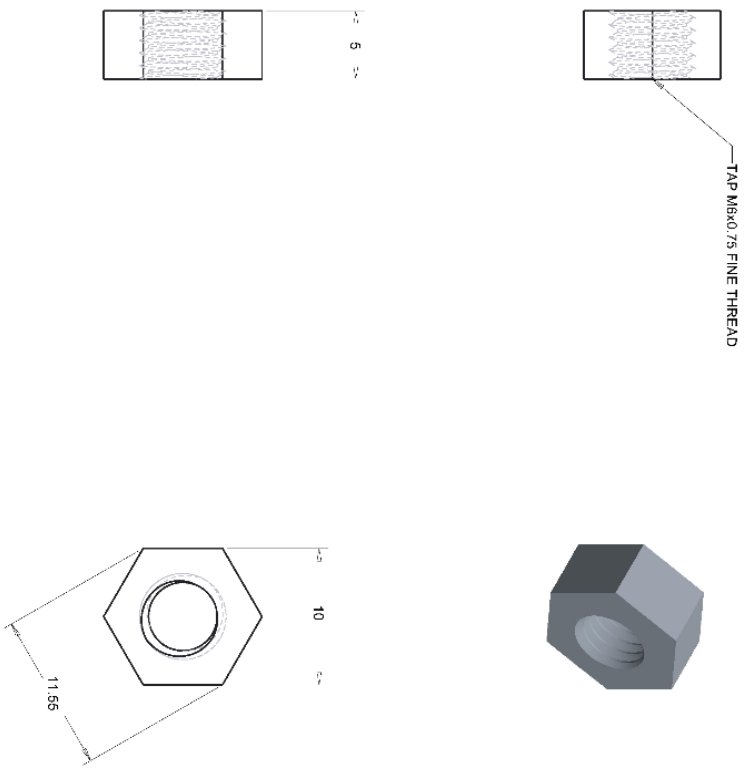
5
TAP M8x0.75 FINE THREAD
10
11.55

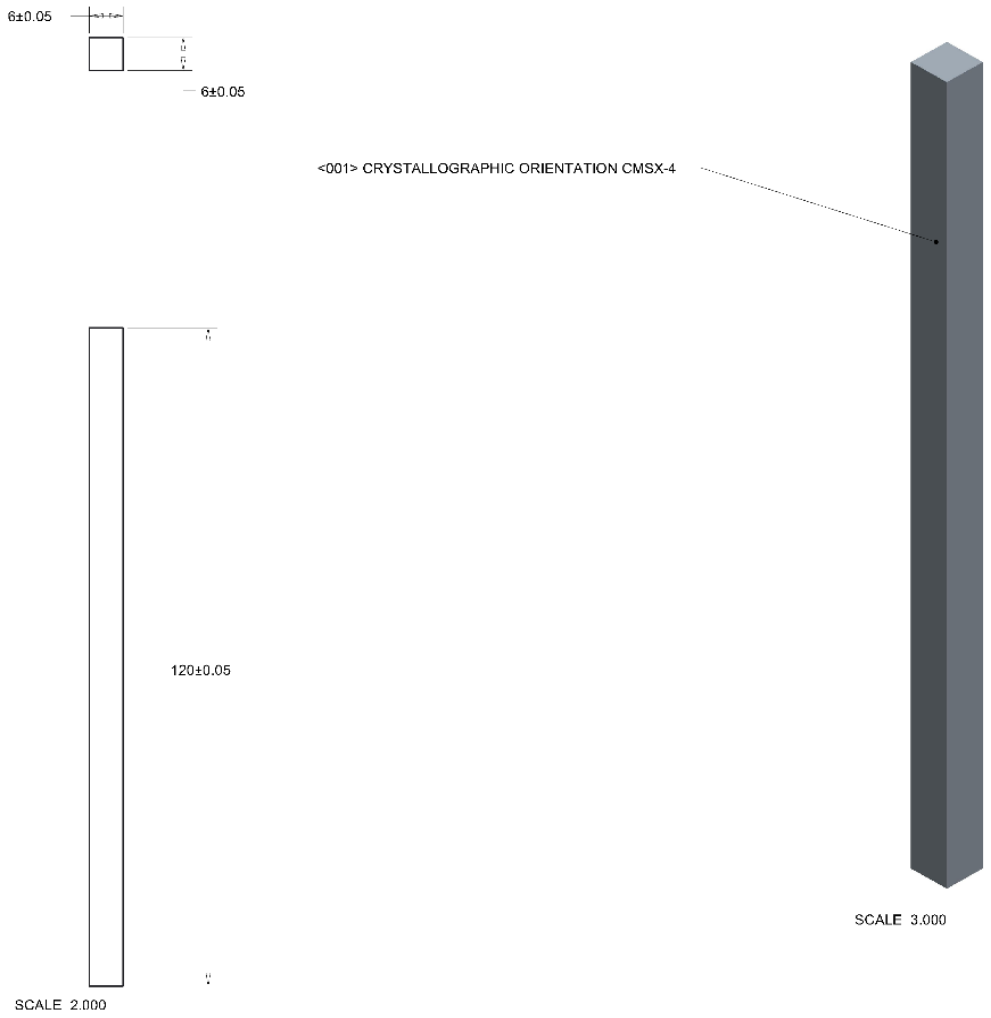
6±0.05
6±0.05
<001> CRYSTALLOGRAPHIC ORIENTATION CMSX-4
120±0.05
SCALE 2.000
SCALE 3.000